Citation for published version:
Chen, H, Zhou, X, Tang, L, Chen, Y, Luo, H, Yuan, X, Bowen, CR & Zhang, D 2022, 'HfO_2-based ferroelectrics: From enhancing performance, material design, to applications', *Applied Physics Reviews*, vol. 9, no. 1, 011307. https://doi.org/10.1063/5.0066607

DOI:
10.1063/5.0066607

Publication date:
2022

Document Version
Peer reviewed version

Link to publication

This article may be downloaded for personal use only. Any other use requires prior permission of the author and AIP Publishing. The following article appeared in Haiyan Chen, Xuefan Zhou, Lin Tang, Yonghong Chen, Hang Luo, Xi Yuan, Chris R. Bowen, and Dou Zhang , "HfO2-based ferroelectrics: From enhancing performance, material design, to applications", Applied Physics Reviews 9, 011307 (2022) and may be found at https://doi.org/10.1063/5.0066607

University of Bath

Alternative formats

If you require this document in an alternative format, please contact:
openaccess@bath.ac.uk

General rights
Copyright and moral rights for the publications made accessible in the public portal are retained by the authors and/or other copyright owners and it is a condition of accessing publications that users recognise and abide by the legal requirements associated with these rights.

Take down policy
If you believe that this document breaches copyright please contact us providing details, and we will remove access to the work immediately and investigate your claim.

Download date: 08. Jun. 2022

HfO_2-based ferroelectrics: from enhancing performance, material design, to applications

Haiyan Chen,[1] Xuefan Zhou,[1]* Lin Tang,[1] Yonghong Chen,[1] Hang Luo,[1] Xi Yuan,[2]*

Chris R Bowen,[3] Dou Zhang [1]*

AFFILIATIONS

[1] Powder Metallurgy Research Institute, State Key Laboratory of Powder Metallurgy, Central South University, Changsha, Hunan 410083, China.

[2] College of Chemistry and Chemical Engineering, Central South University, Hunan 410083, China

[3] Department of Mechanical Engineering, University of Bath, Bath BA27AY, UK

Email: dzhang@csu.edu.cn, ZXF143312115@csu.edu.cn

E-mail: xiyuan@csu.edu.cn

ABSTRACT

Nonvolatile memories are in strong demand due to the desire for miniaturization, high speed storage, and low energy consumption to fulfill the rapid developments of big data, the Internet of Things, and artificial intelligence. Hafnia (HfO_2)-based materials have attracted significant interest due to the advantages of complementary-metal-oxide-semiconductor (CMOS) compatibility, large coercive voltage, and superior ferroelectricity at an ultra-thin thickness. The comparable ferroelectricity to that of traditional perovskite materials and size advantage of HfO_2 result in fascinating storage performance, which can be readily applicable to the fields of integrated non-volatile memories. This review provides a comprehensive overview of recent developments in HfO_2-based ferroelectrics, with attention to the origin of ferroelectricity, performance modulation, and recent achievements in the material. Moreover, potential solutions to existing challenges associated with the materials are discussed in detail, including the *wake-up* effect, long-term *fatigue* behavior, and *imprint* challenges, which pave the way for obtaining HfO_2-based ferroelectric materials and devices with long service life and high stability. Finally, the range of potential applications for these fascinating new materials are presented and summarized, which include non-volatile memories and neuromorphic systems. This review intends to present the state-of-the-art HfO_2-based ferroelectrics and to highlight the current challenges, possible applications and future opportunities, and can act as an update for recent developments in these intriguing materials and provide guidance for future researchers in the design and optimization of HfO_2-based ferroelectric materials and devices.

TABLE OF CONTENTS

I. INTRODUCTION 5

II. FUNDAMENTALS OF PHASE STRUCTURES IN HFO_2-BASED FILMS 11

III. INDUCING FERROELECTRICITY AND PERFORMANCE ENHANCEMENT 19

A. Elemental doping 19

1. Metal doping 19

2. Non-metallic impurities 24

B. Mechanical stress 30

1. Mechanical stress from electrodes 30

2. Strain from substrates 34

C. Surface and interface energy 40

IV. CHANLLENGES OF THE WAKE-UP EFFECT AND FATIGUE PROCESS IN HFO_2-BASED FILMS 47

A. Wake-up effect 49

B. Fatigue process 55

C. Other technical issues 60

V. APPLICATIONS BASED ON FERROELECTRIC HFO_2-BASED FILMS 65

A. Non-volatile memories 65

1. Ferroelectric random-access memories (FRAMs) 66

2. Ferroelectric field effect transistors (FeFETs) 70

3. Ferroelectric tunneling junctions (FTJs) 76

B. Bioelectronic synapses for neuromorphic applications 79

VI. SUMMARY AND PERSPECTIVE 84

ACKNOWLEDGEMENTS 85

DATA AVAILABILITY 86

REFERENCES 86

I. INTRODUCTION

As the world continues to develop towards information digitization, the storage capacity, reliability, and safety of our data is of vital importance. As the carrier of data, the selection of storage materials is crucial for future information dissemination. Ferroelectric materials, as a form of storage material, can exist in two or more polarization states and can therefore maintain a non-zero residual polarization after removal of an externally applied voltage.[1] Figure 1 presents the development of ferroelectric materials, where *ferroelectricity* was first discovered in Rochelle salt by Valasek in the early 1920s. [2,3] Subsequently, conventional perovskite ferroelectrics such as $BaTiO_3$ (BT) and $Pb(Zr,Ti)O_3$ (PZT) were investigated in the 1950s.[4,5] With the development of micro-electro-mechanical systems (MEMS), ferroelectric films were successfully combined with silicon fabrication techniques and ferroelectric devices began to appear.[6,7] To fulfill the demand of portable devices such as laptop computers and mobile phones, ferroelectric films have been extensively used and integrated in ferroelectric random-access memories (FeRAM), ferroelectric field effect transistors (FeFET), radio frequency identification (RFID), and piezoelectric transducers.[8,9]

The initial discovery of ferroelectricity in 10 nm-thick Si: HfO_2 films can effectively solve the existing challenges of the thickness limitation and CMOS incompatibility of ferroelectrics with perovskite structures.[10] The superior properties of HfO_2-based thin films has triggered significant research interest in ferroelectric materials and devices. Today, the von Neumann bottleneck has become a serious concern due to the much lower data storage speed compared to the operation speed for

when dealing with large amounts of data. Neural networks can perfectly solve these problems, based on distributed parallel information processing, and ferroelectric films can act as biological synapses to effectively imitate the behavior of the human brain and achieve artificial intelligence with high speed and low loss.[11] Despite the great achievements made in perovskite-based ferroelectrics to date, there exists a number of challenges when applying them to non-volatile memories. Firstly, the ferroelectricity of perovskite ferroelectrics can decrease, or even vanish, when the thickness of the materials decreases to dimensions below 100 nm due to poor interface qualities, which can severely deteriorate the reliability of a potential ferroelectric device.[12-14] Moreover, the multi-component nature of perovskite ferroelectrics makes it complex to control the elemental ratio precisely during large scale manufacture of thin films, especially with the volatilization of Pb and Bi elements at high temperatures.[15,16] Finally, the relatively narrow bandgap (E_g ~ 3–4 eV) can lead to a large leakage current and increase the risk of film device damage.[1,15,16] Thus, there is an urgent desire to develop new ferroelectric materials to solve these challenges, and HfO_2-based ferroelectric films have become an attractive potential solution with promising properties that are comparable, or even better, than ferroelectrics based on perovskite structures.

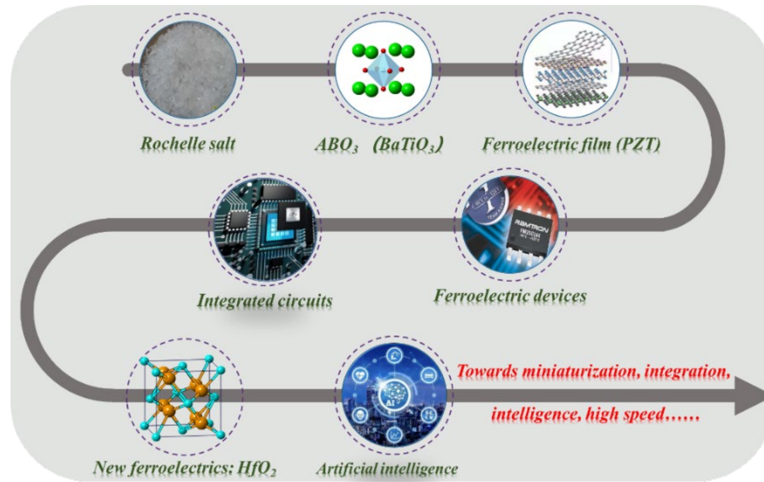

FIG. 1. Development of ferroelectric materials from bulk materials, to thin films, and to devices.

Initially, HfO_2 was often used as a high-*k* (where *k* is relative permittivity) gate insulator in an effort to replace SiO_2 in metal-ferroelectric-insulator-semiconductor (MFIS) transistors due to its high permittivity ($\varepsilon_r \sim 25$) and wide bandgap (E_g: 5~6 eV).[17-19] Since the discovery of ferroelectricity in 10 nm-thick Si: HfO_2 films by Böscke *et al*. in 2011, HfO_2-based ferroelectrics have been in the spotlight as a potential material to replace perovskite based ferroelectrics.[10] A variety of strategies have been used to modulate and control the ferroelectric properties of HfO_2-based films, including elemental doping, interfacial engineering, surface energy effects, and deposition methods.[10,20-25] Based on the multi-functional characteristics of the materials, which include dielectric, ferroelectric, anti-ferroelectric, and piezoelectric performance, HfO_2-based materials have attracted interest in a wide range of applications, as shown in Fig. 2. The non-volatile features of HfO_2-based materials with an ultra-thin thickness allow them to be employed in 3D integration of FeRAM, FeFET, and bioelectronic

synapses.[15,26] Muller *et al*. reported the anti-ferroelectric properties of ZrO_2/HfO_2 films in Zr-rich conditions,[27] and similar phenomena were also discovered in Al: HfO_2 [28] and Si: HfO_2[10]. The remnant polarization could become very small, or even zero, and no hysteresis loops appear, which is appropriate for energy storage applications to improve efficiency. The presence of an electric field-induced anti-ferroelectric to ferroelectric phase transition makes them attractive for applications in supercapacitors, energy harvesting, and solid-state cooling.[29,30] Moreover, Takanori *et al*. improved the thickness limitation from the nano-scale to micro-scale, and 1 μm-thick Y: HfO_2 films exhibited good ferroelectric and piezoelectric properties with a remnant polarization of 14 $\mu C/cm^2$.[31] Piezoelectricity was also identified by Kirbach *et al.* in 20 nm-thick Si:HfO_2 films which can promote the development of highly integrated nano-electro-mechanical-systems (NEMS) and sensor devices.[32] Ferroelectric films can also display large strain under an external electric field, which can actuate micro- or nano-scale devices. Recently, ferroelectricity was even observed in bulk Y:HfO_2, which has overcome the current thickness limitation and provides the possibility for next-generation ferroelectric devices.[33]

A number of review papers have been published in this area, concerning the structures and applications of HfO_2-based films in ferroelectric and anti-ferroelectric devices. For example, Park *et al.* summarized ferroelectricity and anti-ferroelectricity in HfO_2-based films from the origin of ferroelectric properties to an overview of experimental work, and finally to their possible applications.[15] Subsequently, Park *et al.* introduced the advantages and critical issues of the fluorite-structure HfO_2 for memory

devices, and proposed that appropriate doping, decreasing the oxygen vacancy concentration, and anti-ferroelectric properties could also be useful for improved device endurance.[34] Mikolajick et al. explained how HfO_2, compared to traditional perovskite materials, can solve the major issues that exist in 1-transistor-1-capacitor (1T-1C) ferroelectric random-access memories (FeRAMs) and ferroelectric field-effect-transistors (FeFETs), due to its low permittivity and high coercive field. [35] Park et al. comprehensively described the existing issues and the possible influencing factors in HfO_2 from the fundamental physics for semiconductor devices, and proposed the corresponding feasible solutions.[36] Peši´c *et al.* introduced in-depth studies of ferroelectric hafnium and related devices based on models of the physical mechanisms.[37] Park *et al.* systematically reviewed anti-ferroelectric hafnium from the underlying science to energy-related applications based on both pyroelectricity (change of polarization with temperature) and anti-ferroelectricity.[38] In addition to the above simulation and experimental reviews, new insights are also overviewed from the perspective of defects and domains. Park *et al.* summarized the effects of defects on the ferroelectric properties of fluorite-structure oxides, including point defects (*e.g.* oxygen vacancies, carbon and hydrogen) and two dimensional defects (*e.g.* interfacial layer and grain boundaries).[39] Lee *et al.* delivered a comprehensive review of ferroelectricity in fluorite-structured ferroelectrics, covering the domain dynamics and related applications, especially in neuromorphic computing applications.[40] However, there still exists no systematic review on the current status and developments of HfO_2-based thin films. There is a continued debate on the origination of ferroelectricity and the kinetic

phase transitions of HfO_2. Additional challenges also need to be resolved, including wake-up effects, long-term fatigue response, and imprint effect.

In this review, the atomic structure of HfO_2-based ferroelectrics and the kinetic origin of ferroelectricity are initially introduced (Section 2). A range of strategies for inducing ferroelectricity and enhancing the performance in HfO_2-based thin films are then comprehensively overviewed (Section 3). Then, current technical and research challenges are put forward and methods to modulate and control the materials are proposed that can lead to improved properties for practical applications (Section 4). Finally, the possible applications of HfO_2-based thin film devices that aim to exploit ferroelectricity in these materials are summarized, and future perspectives are provided to highlight new and emerging research directions in this new and emerging research area (Section 5). The fundamentals of the phase structure of HfO_2-based materials are now described.

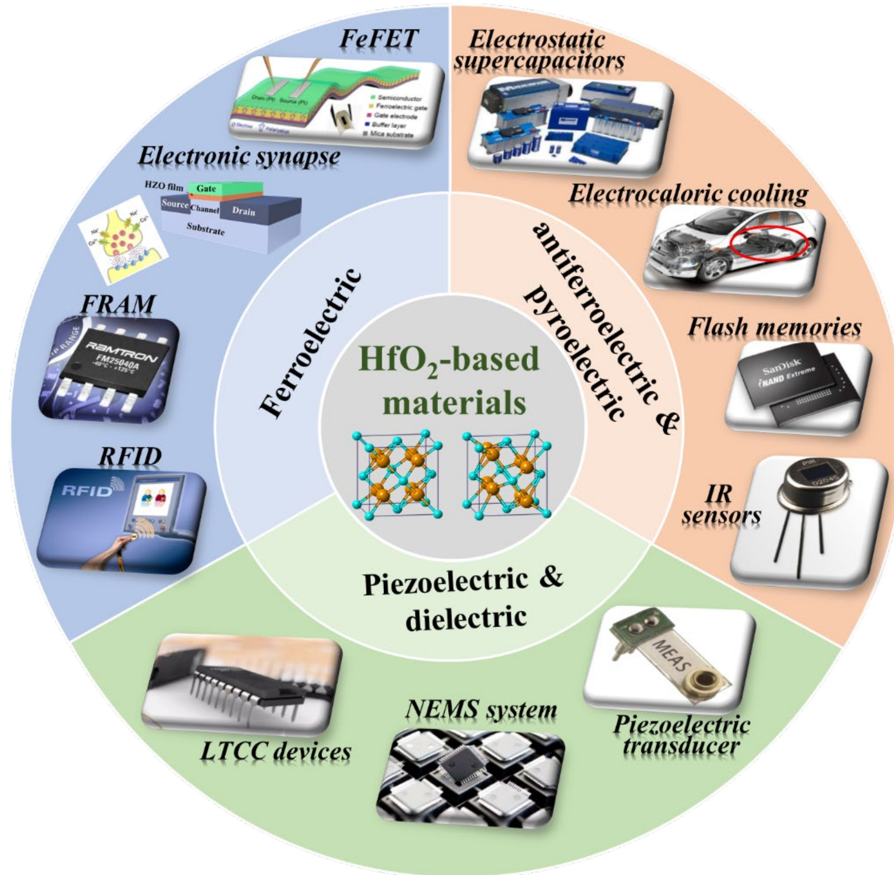

FIG. 2. Applications and properties of HfO_2-based materials.

II. FUNDAMENTALS OF PHASE STRUCTURES IN HFO$_2$-BASED FILMS

The ground state of bulk HfO_2 is monoclinic phase (*m*-phase), with a space group of $P2_1/c$ at room temperature under standard pressures. In a similar way to zirconium oxide (ZrO_2), the *m*-phase is able to transform to the tetragonal phase (*t*-phase) with space group $P4_2/nmc$ at temperatures of ~1770°C, [41] and then to a cubic phase (*c*-phase, $Fm\overline{3}m$) at higher temperatures, above 2550°C. [42] In addition, the centrosymmetric orthorhombic phase (*o*-phase) has been confirmed to be stable under high pressures. As shown in Fig. 3(a), the temperature-pressure phase diagram for bulk hafnium indicates

that with an increase of hydrostatic pressure, the orthorhombic I phase (o_I phase, *Pbca*) and orthorhombic II phase (o_{II} phase, *Pnma*) can be induced at 4 GPa and 14.5 GPa, respectively. [43] It seems that no ferroelectricity can be induced in bulk HfO_2.

Approximately two decades ago, Kisi *et al.* firstly discovered that the *t*-phase of ZrO_2 could be transformed into a polar *o*-phase ($Pca2_1$) in Mg-doped ZrO_2 subjected to an asymmetric stress during the cooling process. [44] A smaller volume difference between the *t*-phase and *o*-phase (1.3%), compared to the volume difference between the *t*-phase and *m*-phase (5%), made the phase transformation more favorable.[44,45] Then, ferroelectricity was also firstly observed in 10 nm-thick Si: HfO_2 capped with TiN electrodes in 2011. [10] Figure 3(b) shows the corresponding glancing incident X-ray diffraction (GIXRD) patterns of Si: HfO_2 films without, and with, titanium nitride (TiN) capping. Non-ferroelectric *m*(-111) and *m*(111) peaks were located at 28.5° and 31.5°, respectively. The peak near 30.5° is thought to be the mixture of *t*(001) and *o*(111) peaks, because their structures are quite similar and cannot be distinguished by regular XRD measurements. Ferroelectricity can be induced by the clamping stress of TiN, which will be described in detail in Section III. In contrast to the widely reported ferroelectric *o*-phase, Wei *et al.* also reported a rhombohedral (*r*-phase, *R3m*) ferroelectric phase in epitaxially strained $Hf_{0.5}Zr_{0.5}O_2$ (HZO) thin films, as evidenced by the appearance of a diffraction peak at 2θ = 27.13°.[46] The strong ferroelectricity in the material was attributed to the large in-plane tensile stress from the epitaxial substrate, which was also verified through density-functional-theory calculations.[47] Nukala *et al.* also proved the coexistence of the *r*-phase with *o*-phase in HZO films. [48]

In fact, the *m*-phase is energetically favorable due to its low free energy. However, among all the potential fluorite crystalline structures, the polar *o*-phase is the most common reported phase to exhibit non-centrosymmetry. The crystal structures of all phases are displayed in Fig. 3(c), and the lattice parameters of each structure are also shown in Table I. Each structure consists of Hf^{4+} cations at the corners and O^{2-} anions at the tetrahedral interstitial sites, and the polarity of HfO_2 is achieved through the up and down movement of oxygen anions. The difference in the distance between the four oxygen atoms and Hf atoms leads to a polarity. Compared to the *t*-phase, the *a*- and *b*-directions of the *o*-phase are constrained and the *c*-direction is elongated because of their varied thermal expansion coefficients. [49] The *m*-phase is comparatively stable, therefore it is necessary to apply an external stress or exploit other strategies to obtain the metastable *o*-phase, which has been demonstrated both experimentally and theoretically.[49,50] In addition, the orthorhombic Ш phase ($o_{Ш}$ phase, $Pca2_1$) was confirmed to be non-centrosymmetric and polar, which could be induced by a variety of strategies, including the application of a clamping stress [51] and a surface energy effect. [52,53]

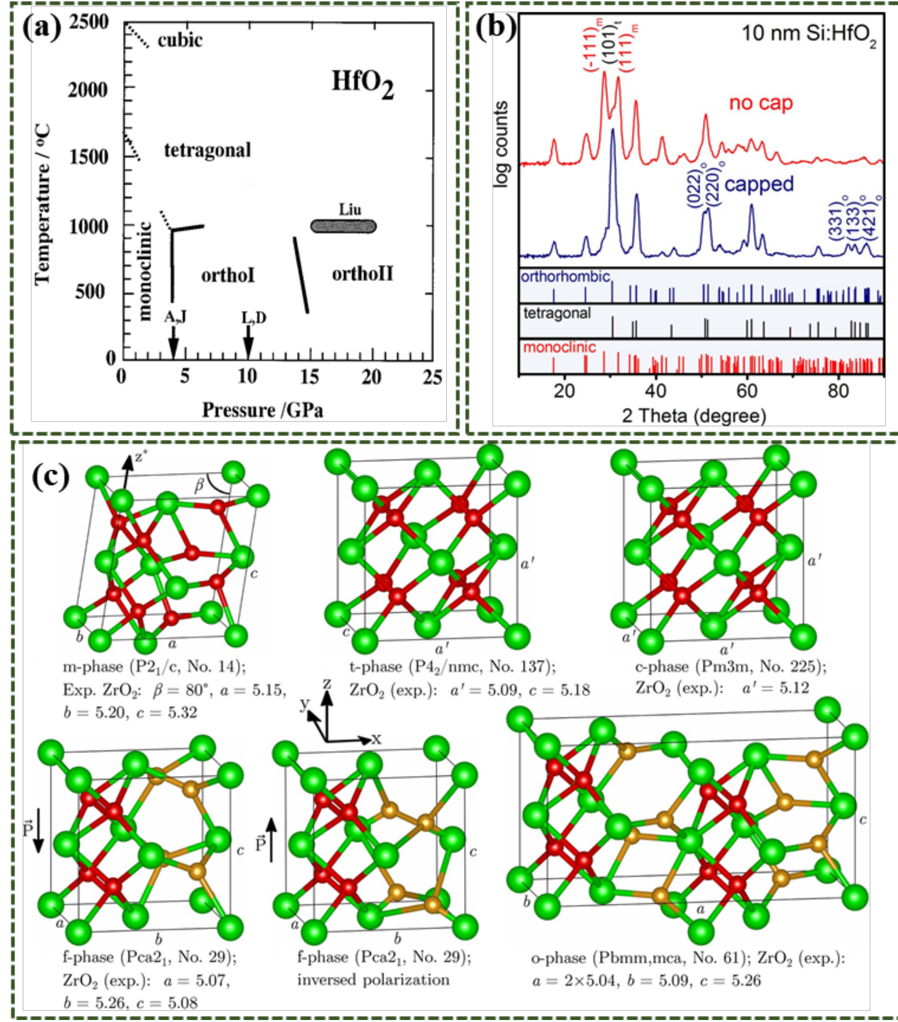

FIG. 3. (a) Pressure - temperature phase diagram of HfO_2. [43] (b) GIXRD measurements of Si: HfO_2 samples of the same composition with TiN capping and no capping.[10] (c) Crystal structures of polymorphs in HfO_2, including *m*-phase, *t*-phase and *o*-phase. [54] Reproduced with permission from (a) O. Ohtaka et al., J. Am. Ceram. Soc. 84 (6), 1369 (2001).[43] Copyright 2004, John Wiley and Sons. Reproduced from (b) Böscke et al., Appl. Phys. Lett. 99 (10) (2011),[10] (c) Materlik et al., J. Appl. Phys. 117 (13) (2015),[54] with the permission from AIP publishing.

Table I. Lattice parameters of HfO_2 with different crystal structures.

Crystal structure	*a*(Å)	*b*(Å)	*c*(Å)	α	β	γ	Reference
m-phase	5.12	5.17	5.29	90°	99.11°	90°	[55]

t-phase	5.08	-	5.17	90°	90°	90°	[27]
o-phase	5.24	5.06	5.07	90°	90°	90°	[56]

Based on the bulk energy, the *o*-phase is accepted to be unstable under processing conditions. Thus, the origin of ferroelectricity in fluorite HfO_2 thin films has been examined widely, combining theoretical simulations and experiments according to the thermodynamic and kinetic models. Materlik *et al.* firstly reported the thermodynamic stabilization of the o-phase due to a surface energy effect according to density functional computations.[54] Ferroelectricity was expected to exist in a small size range near 10 nm, in the absence of strain, and decreased when the film thickness was increased to over 14 nm. Park *et al.* systematically compared the discrepancies of experiments with theoretical predictions, with respect to dopant concentration, film stress and film thickness.[57] The modified interface/grain boundary energy model was suggested to simulate the probable o-phase fraction. The measured $2P_r$ value (where P_r is the remnant polarization) of the $Hf_{0.57}Zr_{0.43}O_2$ composition was large and decreased rapidly with a film thickness over 24.2 nm according to the experimental results, which was quite different from the simulated predictions. Batra *et al.* previously calculated that a compressive stress could stabilize the o-phase,[58] however, experimental observations indicated that the polar o-phase was usually induced under an in-plane tensile stress.[21] Thus, the proposed thermodynamic model is contradictory to the experiments and cannot account for the emergence of a metastable o-phase based on a surface energy effect.

Subsequently, the kinetic model was suggested to describe the phase evolution and

energy barrier between crystallographic phases. A detailed description has been provided by Park *et al.* on the phase transition of a 9.2 nm-thick $Hf_{0.5}Zr_{0.5}O_2$ film with different kinetic energy barriers during the crystallization and cooling processes based on the kinetic origination,[59] as shown in Fig. 4(a)-(k). The phase diagram in Fig. 4(a) was obtained based on thermodynamic model and the as-deposited film was thought to be amorphous in the thermodynamic model, while small nuclei of 2~3 nm were formed in situ during practical deposition in an atomic layer deposition (ALD) chamber, as shown in Fig. 4(b). The stable phase of these nanocrystals is considered to be o-phase, according to Fig. 4(c), which is consistent with the investigation by Materlik *et al.*.[54] The free energy of the t-phase decreases when the temperature increases to 600 °C, as shown in Fig. 4(e), because of its lower entropy compared to the m- and o- phase. Figure 4(f) shows that columnar growth of grains can be observed with an annealing holding time of 1 min at 600 °C, and the m-phase becomes the thermodynamically stable phase at this condition. The presence of columnar grains and emergence of the m-phase at higher temperatures were confirmed in experimental data by Kim *et al.*.[60] From Fig. 4(g), the m-phase becomes the thermodynamically stable phase due to its much reduced total free energy. Park *et al.* estimated the kinetic energy barrier of the phase transition from the t-phase to the m-phase, and the t-phase to the o-phase to be 223–262 meV $f.u.^{-1}$ and 22-31 meV $f.u.^{-1}$ according to general phase transition theory, respectively.[61] The phase transition from the t-phase to the m-phase is suppressed due to its much larger energy barrier and the t-phase is proven to be stable at this step. Thus, the m-phase can be formed if the annealing temperature and holding time are high and long

enough to provide sufficient thermal energy to over-compensate the large driving force of the phase transition. After a rapid thermal process (RTP), the phase transition from the t-phase to the o-phase readily occurs at low temperatures because of its low energy barrier, as shown in Fig. 4(h)-(k). Thus, RTP is thought to be a key process for the formation of the ferroelectric o-phase.

Lee *et al.* calculated the activation energy barrier of the phase transition from the t-phase to the m-phase, which was 2.14 eV $f.u.^{-1}$ and 1.67 eV $f.u.^{-1}$ with and without a TiN capping layer, respectively.[62] The presence of a TiN capping layer can inhibit the nucleation and growth rate and induce a large tensile stress in the films. In addition, Ti and N diffusion can lower the free energy of the t-phase. Dopant concentrations were also investigated and identified to largely affect the energy barrier of phase transition. Wu *et al.* calculated the free energy of all phases for pure HfO_2 and Si: HfO_2 with different dopant concentrations by ab initio molecular-dynamics simulations.[63] A diffusion-less phase transition can take place from the t-phase to the o-phase with appropriate Si doping during the cooling process because of its lower energy barrier. Tashiro et al. comprehensively studied the kinetic formation of the o-phase in epitaxial xY: HfO_2 (x=0.05-0.09) thin films.[64] For Y: HfO_2 with a high Y concentration, the t-phase is frozen due to the stabilization of the t-phase at a high transition temperature. The same group also reported on the temperature-dependent structures of Y: HfO_2 using in-situ XRD and TEM measurements, which verified the formation of the o-phase during the cooling process. [24,25,65] Shimizu *et al.* revealed the typical electric field-induced phase transition after application of an electric field using TEM

characterization. [66] Based on these investigations, a variety of factors such as dopants, RTP process, stress, electric field and oxygen vacancies, can influence the energy barrier of phase transitions, which should be considered in detail to obtain the o-phase.

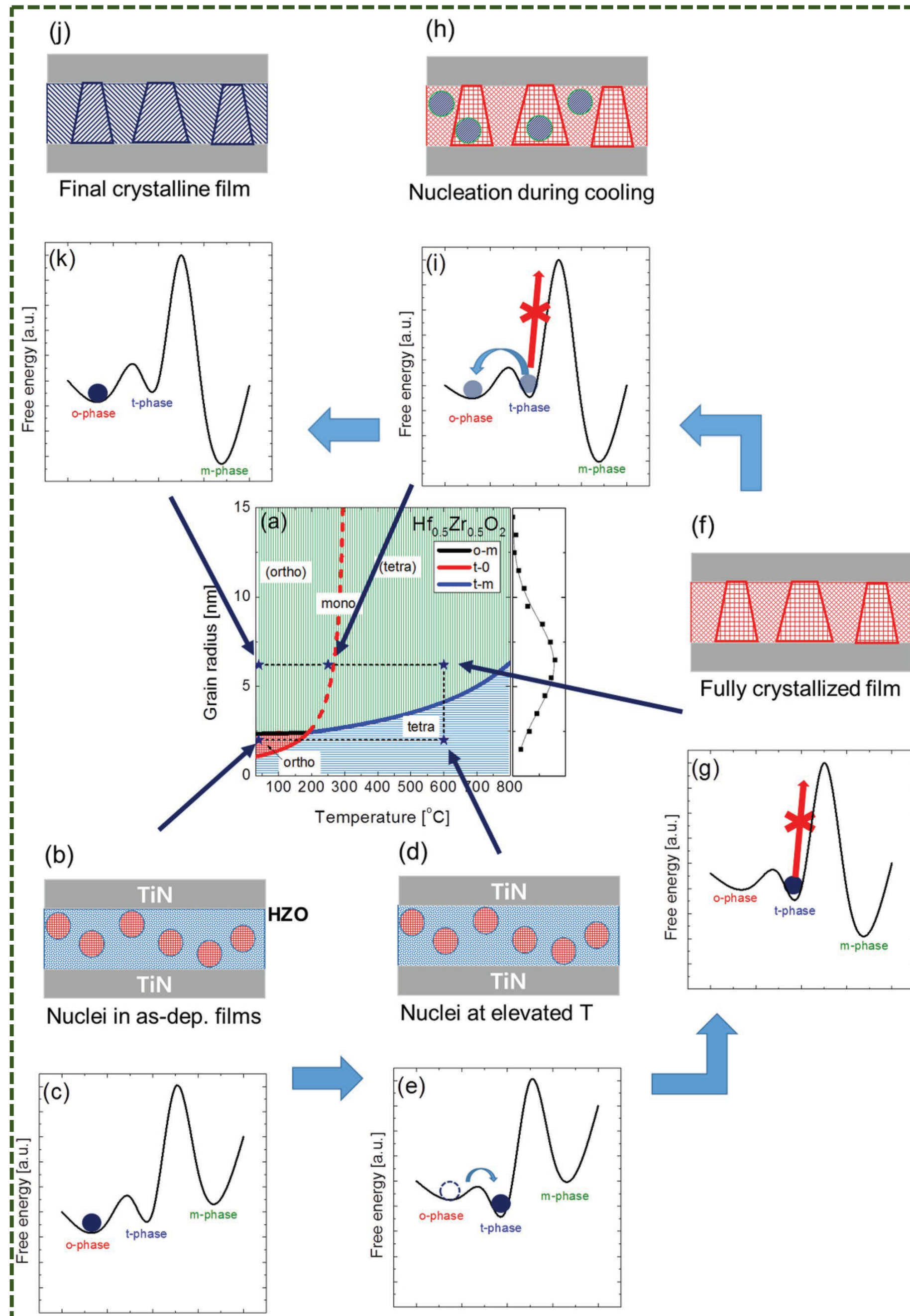

FIG. 4. (a) Phase diagram for $Hf_{0.5}Zr_{0.5}O_2$ thin film with different grain sizes under various temperatures, (b, d, f, h, j) schematic diagram of the phase transition and (c, e, g, i, k) free energy curves during the whole rapid thermal process for film

crystallization.[59] Reproduced with permission from (a-k) Park *et al.*, Adv. Electron. Mater. 5 (3) (2019).[59] Copyright 2018, John Wiley and Sons.

III. INDUCING FERROELECTRICITY AND PERFORMANCE ENHANCEMENT

Data storage can be realized through the reversal of ferroelectric domains, and a high ferroelectric activity should therefore be stabilized for the improvement of data retention and persistence. Theoretical analysis and experiments have been conducted by a variety of researchers to achieve a high level of ferroelectricity in HfO_2-based materials. [54,67] In their reports, the ferroelectric phase can be induced by an applied stress, a large surface energy, and the application of an external electric field. The theoretical remnant polarization (P_r) could reach 53 μC/cm^2 according to the displacement of oxygen anions from Hf cations.[54] However, the P_r values obtained in experiments are usually lower, in the range of 12~30 μC/cm^2, and ferroelectricity is difficult to achieve in pure HfO_2. To induce a high level of ferroelectricity in HfO_2-based films, a variety of strategies have been carried out, such as element doping, the introduction of a mechanical stress, and a surface energy effect, which are now described in detail.

A. Elemental doping

1. *Metal doping*

The doping strategy for HfO_2 can be classified into *metal* doping and *non-metallic* impurities. Metal doping includes those elements with smaller or larger atomic radius

compared to the Hf atom. When doping with smaller atomic radius elements, the dopant can decrease the bond length of the metal-oxygen, increase the asymmetry of the structure, and induce a ferroelectric and anti-ferroelectric response to HfO_2-based films. Dopants with a larger atomic radius can increase the bond length of the metal-oxygen and lead to asymmetry, which can induce a ferroelectric response in HfO_2-based films; but no anti-ferroelectric response. As shown in Fig. 5(a)-(c), Mueller *et al.* [28] fabricated Al:HfO_2 via an atomic layer deposition (ALD) technique, and the effect of doping concentration on the structural and electrical properties were studied. It was found that a phase transition from the *m*-phase to *o*-phase, and finally to the *t*-phase, occurred with increasing Al content, which was indicated by XRD measurements and a continuous increase in relative permittivity of the Al: HfO_2. In addition, Figure 5(c) shows that P_r values over zero could be obtained in the Al concentration ranges from 3.1 mol% to 11.4 mol%. A maximum P_r value of ~6 μC/cm^2 was achieved in 7.1 mol% Al doped HfO_2.

Similar to Al: HfO_2, Zr: HfO_2 was also reported to have the same structural and performance changes.[27,68-71] Zr is recognized to be an attractive doping element because of its infinite solid solubility with Hf and low crystallization temperature. The infinite solid solubility is attributed to the similar atomic radius and crystal structures of Zr and Hf atoms.[72] Muller *et al.*[27] carefully discussed the existence of ferroelectricity and anti-ferroelectricity in Zr-doped HfO_2 films by measurement of the polarization-electric field (*P*-*E*) hysteresis loops. As shown in Fig. 5(e), undoped HfO_2 showed a dielectric behavior with an almost nearly-zero remnant polarization (P_r).[27] With an increase of Zr

content, the samples exhibited a ferroelectric response and a P_r value of 17 μC/cm^2 was achieved in the $Hf_{0.5}Zr_{0.5}O_2$ film. Furthermore, anti-ferroelectric behavior was revealed in a $Hf_{0.3}Zr_{0.7}O_2$ film, similar to ZrO_2.[27] Correspondingly, the dielectric constant (ε_r) exhibited an increase with an increasing amount of Zr, which indicated a phase transition from the *m*-phase to the *o*-phase, and finally to the *t*-phase based on their different ε_r values (*m*-phase: ~25, *o*-phase: ~30, *t*-phase: ~35).[27,28] Park *et al.*[68] carried out detailed experiments on the Morphotropic Phase Boundary (MPB) of $Hf_{1-x}Zr_xO_2$ solid solutions and a schematic phase diagram is shown in Fig. 5(d). The stable ferroelectric *o*-phase can be regulated through controlling the Hf/Zr ratio and the film thickness. Such a similar phase transition process also existed in other doped systems based on Si: HfO_2 [73-76] and La: HfO_2 [77,78]. The antiferroelectric-like HfO_2-based films are ideally suited to energy storage in supercapacitors because of their near zero P_r values and large saturation polarization (P_s).[30,79] It was reported that La-doped HfO_2 films showed a high energy storage density of 50 J/cm^3 with 70% efficiency.[78,80] The ultrathin thickness, ultrahigh breakdown strength, and CMOS compatibility of HfO_2-based films makes then attractive for future 3D integrated capacitors.[81]

However, not all dopants can lead to a ferroelectric-antiferroelectric phase transition. Muller *et al.* investigated the influence of Y doping on the properties of Y: HfO_2 films with a TiN capping electrode, and the polarization - voltage (*P-V*) loops are shown in Fig. 5(f).[51] The Y content was varied from 2.3 to 12.3 mol%. and under post-metal annealing (PMA) conditions, it was found that the P_r of the films increased to 24 μC/cm^2 with a dopant level of 5.2 mol% of Y and then decreased to nearly zero with a

dopant level of 12.3 mol% of Y. Under the post-deposition annealing (PDA) conditions, the films showed a similar variational trend with regard to ferroelectric properties, but had relatively lower P_r values, which were ascribed to the different mechanical stress applied by the TiN capping electrode during heat treatment. This aspect will be carefully discussed in next section.

In order to clarify the relationship between the crystal radius of the dopants, the dopant content, and the resulting ferroelectricity of HfO_2-based films, Schroeder *et al.* [26] summarized a contour plot of P_r values as a function of crystal radius and dopant content, as shown in Fig. 5(g). In most cases, a P_r value of 15 ~ 25 μC/cm^2 can be achieved and the appropriate dopant content was determined to be 3 ~ 6 mol%. Dopants with a smaller radius than Hf exhibited a wide range of doping contents (e.g., Al: 0-10 mol%, Si: 2-5 mol%). At high doping contents, the films were able to exhibit a stabilized *t*-phase or even anti-ferroelectricity. Meanwhile, for dopants with a larger radius than Hf (*e.g.*, Y, La, Sr, Gd), the doping content range was rather narrow and a phase transition of *m*-phase→*o*-phase→*c*-phase can be observed on increasing the concentration of dopants, which was also verified by the first principle method[82] and clearly shown in doped ZrO_2-based films.[83] Dopants were thought to change the symmetry of the crystal structure because of their different ionic radius from Hf and different bond length between the metal atom and oxygen atom.[84] In addition, when the valence of dopants is different from Hf, the introduction of oxygen vacancies can also lead to the asymmetry of the crystal structure and lead to the appearance of ferroelectricity.

Al:HfO_2

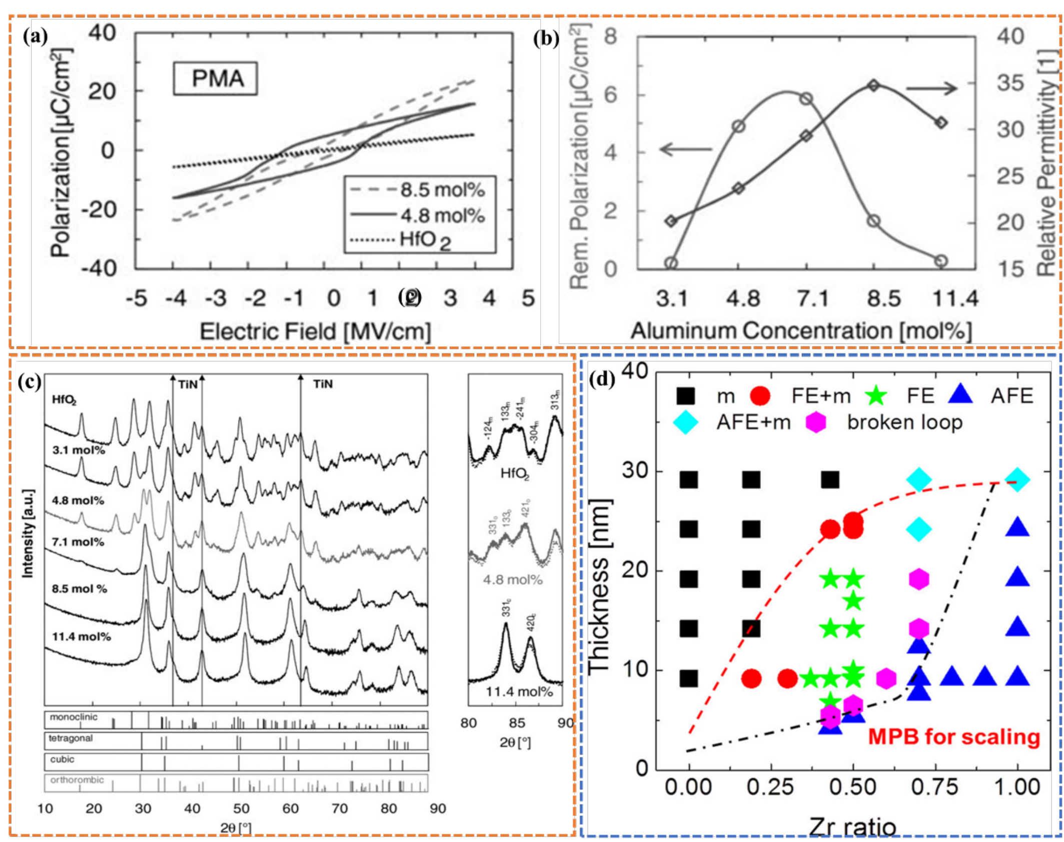

Zr:HfO_2

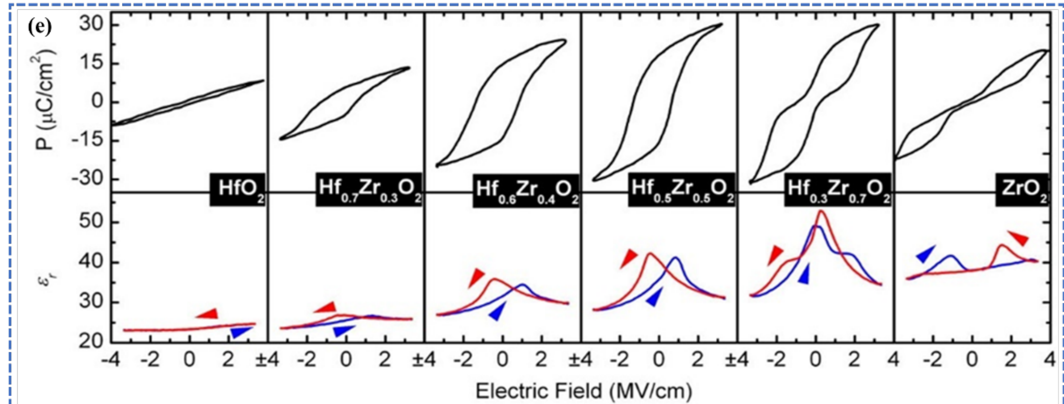

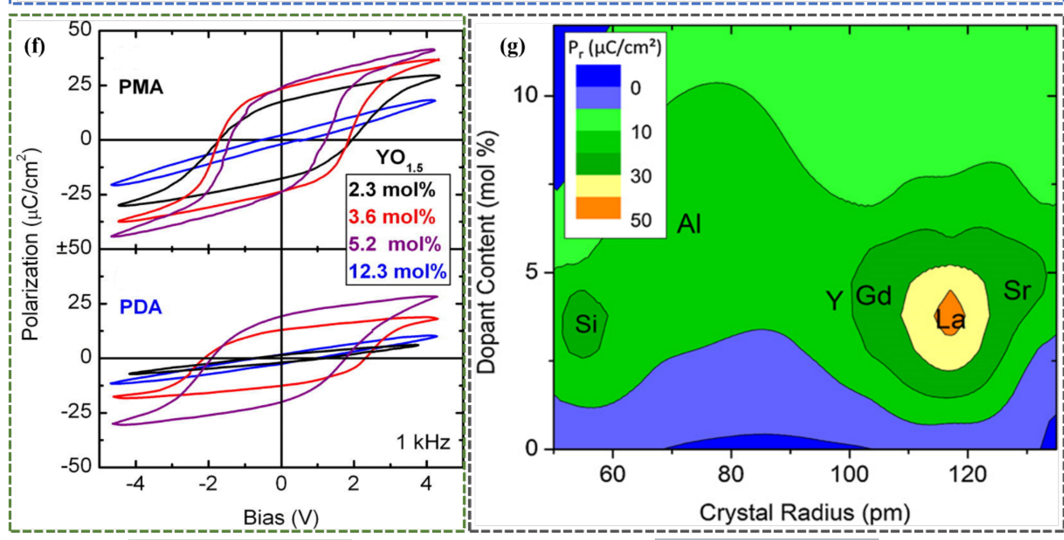

Y:HfO_2

Contour plot

FIG. 5. (a) Polarization hysteresis, (b) GI-XRD diffractograms and (c) relation schematic between polarization and Al concentration for PMA Al: HfO_2 capacitors.[28] (d) MPB diagram of $Hf_{1-x}Zr_xO_2$ solid solution.[68] (e) *P*-*E* loops and ε_r-*E* curves of Zr-doped HfO_2 films.[27] (f) *P*-*V* loops of 10 nm-thick ALD-deposited Y: HfO_2 films with various doping contents under PMA and PDA conditions, respectively.[51] (g) Contour plot of P_r values as a function of crystal radius and dopant content.[26] Reproduced with permission from (a-c) Mueller et al., Adv. Funct. Mater. 22 (11), 2412 (2012).[28] Copyright 2012, John Wiley and Sons; (d) Park et al., ACS Appl. Mater. Inter. 10 (49), 42666 (2018).[68] Copyright 2018, American Chemical Society; (e) Muller et al., Nano Lett. 12 (8), 4318 (2012). [27] Copyright 2012, American Chemical Society; Reproduced from (f) Mülleret al., J. Appl. Phys. 110 (11) (2011),[51] with permission of AIP publishing; Reproduced with permission from (g) Schroeder et al., Jpn. J. Appl. Phys. 53 (8S1), 08LE02.1 (2014).[26] Copyright 2014, The Japan Society of Applied Physics.

2. *Non-metallic impurities*

In addition to above metal dopants, non-metallic impurities were also reported to induce ferroelectricity in HfO_2-based films, such as N, C and H.[60,85,86] A carbon impurity is quite common in ALD-deposited films due to the incomplete decomposition of metal-organic precursors, especially at lower temperatures. Kim *et al.* [60] investigated the dependence of deposition temperature on the ferroelectric behavior of undoped HfO_2 films, as shown in Fig. 6(a) and Fig. 6(b). The samples can achieve strong ferroelectricity at a deposition temperature of 220 °C, but they behave more like a dielectric at a higher deposition temperature of 280 °C. The ferroelectric properties

were attributed to the existence of carbon in the film, which originated from incomplete decomposition of precursor. Residual carbon could suppress the lateral growth of grains, which could promote the formation of the ferroelectric *o*-phase. However, when the deposition temperature was raised to 240 °C or higher, there was insufficient residual carbon impurities in the film and HfO_2 was no longer ferroelectric. The *t*-phase can also be stabilized in C: HfO_2 films during low temperature decomposition and using low active oxygen source environment.[87] The same triggering mechanism was also demonstrated in other HfO_2 films deposited using chemical solution deposition (CSD) and sputtering methods. However, Künneth *et al.*[88] found that ferroelectricity could not be induced in C: HfO_2 with a carbon concentration from 3.125 f.u.% to 6.25 f.u.% according to calculation of the formation energies. Although carbon substitution is not useful to reduce the free energy of the t-phase, other types of defects should be further investigated to affect the free energy of the t-phase, such as interstitial carbon and carbon with oxygen vacancies.

The properties of perovskite structures can be destroyed by the introduction of hydrogen due to its strong reducibility.[89] Hydrogen impurities are always induced when annealing samples under an H_2 atmosphere. Park *et al.*[86] compared the ferroelectricity of HZO films with and without Pt electrodes after annealing with a forming gas with H-incorporation. The P_r values were only degraded slightly for HZO films both using Pt electrodes and TiN electrodes, which indicated the good resistance of HZO to hydrogen incorporation. As shown in Fig. 6(c-e), Park *et al.*[90] studied the ferroelectric properties and conduction mechanisms of HZO films after annealing under different

atmospheres. Despite the large difference in the built-in electric field in the initial state, the final polarization becomes the same after a *wake-up* process. Nitrogen has a limited negative effect on the performance of HfO_2-based films, especially when using TiN electrodes. Furthermore, Oh *et al.*[91] discovered that the endurance of W/Al:HfO_2/Si stacks could be improved after high-pressure hydrogen annealing, which originated from the passivation of interfacial layer by H-related positive charges.

Oxygen vacancies are commonly reported to induce ferroelectricity in HfO_2-based films. Zhou *et al.*[92] studied the free energy difference of the *o*-phase in HfO_2 by substituting different oxygen sites in computational simulations, as shown in Fig. 6(f-h). With an increase of oxygen vacancies from 0 to 12 f.u.%, the total energies of the *o*-phase compared to the *m*-phase reduced from 2.64 eV to 1.21 eV, respectively. In addition, the energy barrier for polarization switching could be decreased with appropriate use of oxygen vacancies, which was consistent with other reports.[93] The *t*-phase could be transformed to the *o*-phase when the symmetry was broken by oxygen vacancies and the introduction could significantly decrease the energy difference between the *o*-phase and *m*-phase. The ferroelectric phase transition from the *m*-phase to *o*-phase could be easier to complete under the combined effect of oxygen vacancies and other impurities. Nitrogen can be easily introduced into films from the diffusion of TiN electrodes and as an impurity from metal-organic ligands. Xu *et al.*[94] also reported that a small level of N doping (0.34 mol%) can enhance ferroelectric properties significantly, but over-doping ($>$ 1 mol%) can weaken the polarization. The ferroelectric *o*-phase could be stabilized through the use of oxygen vacancies by

constructing Hf-N and N-O covalent bonds.

In addition, Schenk *et al*. firstly prepared Sr: HfO_2 films by ALD, which exhibited a large P_r of 23 μC/cm^2 at a doping content of 4.4 mol%.[95] However, the coercive field was much larger than other HfO_2-based systems due to the large radius of Sr (200 pm).[72] Tang *et al*. also realized ferroelectricity in Sr: HfO_2 by the CSD method.[96] Other dopants such as Ca[97], Pr[60], Gd[98,99], and Lu[100]. were also shown to be effective to induce ferroelectricity in HfO_2. Table II summarizes the properties of doping HfO_2 in recent years and further studies are desired to explore the concentration limit of dopants in HfO_2 and develop new doping elements.

Table II. Summary of ferroelectric doped-HfO_2 films, and their properties.

Dopants	Preparation method	P_r (μC/cm^2)	E_c (MV/cm)	References
3.8 mol% Si	ALD	10	1.0	10
5.2 mol% Y	ALD	24	1.2	51
4.8 mol% Al	ALD	5	1.0	28
50 mol% Zr	ALD	17	1.0	27
2 mol% Gd	ALD	12	1.75	98
Mixed 1.08 mol% Al & 0.75 mol% Si	ALD	20	2	101
undoped	ALD	10.6	-	22
9.9 mol% Sr	ALD	23	~2	95
2.1 mol% La	ALD	17	1	102
5.2 mol% Y	CSD	＞13	2	23
5 mol% Pr	CSD	6.9	1.2	103
10 mol% Sr	CSD	13.3	~0.75	96

10 mol% Ce	CSD	5	~2	[104]
4.8 mol% Ca	CSD	10.5	~2	[97]
7.5 mol% Mg	CSD	3	1	[105]
7.5 mol% Ba	CSD	12	1.7	[105]
undoped	CSD	22.56	-	[106]
5 mol% La	CSD	7	~1.5	[107]
1.9 mol% Y	sputtering	~5	-	[108]
15.64 mol% Zr	sputtering	10	0.75	[109]
undoped	sputtering	9~10	-	[110]
6 mol% Fe	sputtering	8.8	-	[111]
50 mol% Zr	PLD	20	3	[112]
5 mol% Lu	PLD	11	1.6	[100]
7 mol% Y	PLD	14~17	1.3~1.6	[31]
Bulk 12mol% Y	LDFZ	3	4	[33]
4.4 mol% Si	PLD	42	4	[113]

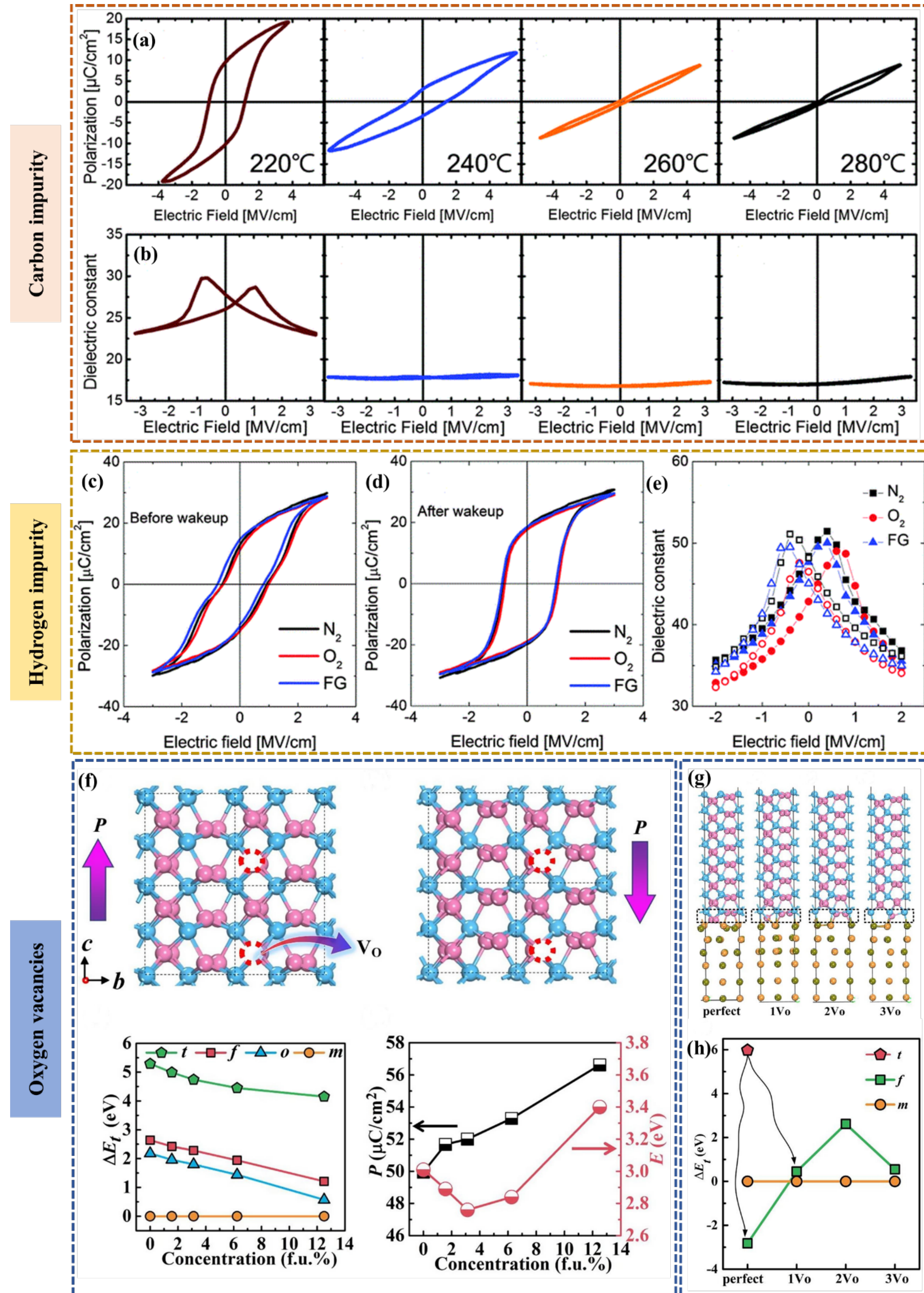

FIG. 6. (a) P - E loops and (b) ε_r - E curves of undoped HfO_2 films.[60] P - E loops (c) before and (d) after wakeup process, (e) ε_r - E curves of HfO_2 annealed at O_2, N_2 and (N_2+H_2) forming gas atmosphere.[90] (f) Dependence of oxygen vacancy on free energy

and polarization reversal of HfO_2, (g) effect of oxygen vacancies at interfaces on the atomic structures, and (h) energies of HfO_2 films of different phase structures with different interfacial oxygen vacancies.[92] Reproduced with permission from (a-b) Kim et al., J. Mater. Chem. C 4 (28), 6864 (2016).[60] Copyright 2016, Royal Society of Chemistry; (c-e) Park et al., J. Mater. Chem. C 3 (24), 6291 (2015).[90] Copyright 2015, Royal Society of Chemistry; (f-h) Zhou et al., Comp. Mater. Sci. 167, 143 (2019).[92] Copyright 2019, Elsevier Ltd.

B. Mechanical stress

The influence of mechanical stress on the properties of HfO_2-based films have attracted interest due to its significant inhibition on the growth of grain volume. Phase transitions from the *t*-phase/*c*-phase to the *m*-phase follows a martensitic transformation, along with a volume expansion.[114] The introduction of a mechanical stress is therefore able to suppress the formation of the *m*-phase, which possesses a larger unit volume than the *o*-phase. Böscke *et al.* and Muller *et al.* discovered that the capacitance and P_r of HfO_2-based films were much lower when there was no TiN capping electrode during crystallization.[10,51] It is concluded that the ferroelectric *o*-phase can be stabilized under the influence of a capping electrode due to a mechanical confinement, which originates from either the upper and bottom electrodes or lower substrate.

1. Mechanical stress from electrodes

TiN electrodes are common in the field of semiconductors, especially during the preparation of HfO_2-based metal-insulator-metal (MIM) capacitors. Lomenzo *et al.* prepared Si: HfO_2 films capped with TiN and Ir upper electrodes, which led to a high

P_r of 22 μC/cm^2 in TiN/Si: HfO_2/SiO_2/Si capacitors.[115] As shown in Fig. 7(a)-(c), Kim *et al*.[116] investigated the ferroelectric behavior of TiN/HZO/TiN capacitors by varying the thickness of the TiN upper electrodes from 45 nm to 180 nm. The presence of upper TiN electrodes with a larger thickness led to the promotion and improvement of ferroelectricity. The HZO film annealed at 400 °C after deposition of a TiN electrode exhibited a P_r of 24 μC/cm^2, which was much larger than that (nearly zero) annealed without a capping electrode.[116] The HZO film was considered to be confined by the TiN capping electrode, which operated as a generator of tensile stress during heat treatment. As a result, the non-symmetric *o*-phase could be formed due to the compression of the *a*-axis and elongation of the *c*-axis. Schroeder *et al*. calculated the tensile stress to be ~2 GPa according to $\sin^2\psi$ from the XRD results of TiN/La: HfO_2/TiN capacitors.[117] The use of TaN electrodes is another appropriate approach, which can provide a large in-plane tensile stress. Lomenzo *et al.* found that Ta-O bonds could accumulate at the interface region and lead to an asymmetric ferroelectric behavior.[118]

Metal electrodes are often used as the top electrodes in HfO_2-based films. Karbasian *et al*. studied the properties of $Hf_{0.8}Zr_{0.2}O_2$ films with W capping electrodes, which showed stronger ferroelectricity than TiN-capped films.[119] Nitrogen was recognized as a catalyst for the formation of oxygen vacancies, but W was minimally diffused into the films. The large mechanical stress induced by W contributed to the improvement of ferroelectricity in HfO_2, as shown in Fig. 7(d)-(f).[120] It was previously reported that W could induce a higher tensile stress due to its lower coefficient of

thermal expansion (CTE: ~4.5×10^{-6}/K) compared to TiN (CTE: $9.35 \times 10-6$/K).[120,121] Other metal electrodes including Pt, Ir, Al, and Ru have also been studied, [21,122-124] however they have almost no clamping effect on HZO films because of their large CTEs. The Ir electrodes can be easily oxidized into IrO_2, which can pull oxygen out from the HZO and promote the formation of non-ferroelectric *m*-phase.

To avoid the oxidation of TiN into TiO_xN_y and TiO_2, oxide electrodes were proposed to provide a clamping stress on the HZO films. Zhang *et al*. reported that in VO_x-capped HZO films, large $2P_r$ value of 36.9 μC/cm^2 and high endurance were observed.[125] As indicated in Fig. 7(g)-(i), a significant shift to the right side of the *P*-*V* hysteresis was found in the HZO films without a VO_x capping layer. The introduction of VO_x can supply additional oxygen for HZO and the oxygen vacancies were largely decreased. Therefore, the built-in electric field was successfully modulated in the films with VO_x electrodes according to the shift of polarization hysteresis. In addition, the decrease of oxygen vacancies could reduce the active charge carriers and improve the endurance and retention properties, as shown in Fig. 7(i). RuO_2 top electrodes were also indicated to decrease the concentration of vacancy defects at the electrode/film interface by Goh *et al*. and the stability of HZO films were increased significantly. [126] Recently, Zhang *et al*. reported on epitaxial ferroelectric HZO films with a thickness over 30 nm deposited on pyrochlore bottom electrodes because of its close lattice size to HZO. [127] The epitaxial strain can effectively stabilize the polar *o*-phase. In general, TiN is recognized to be the most potential electrode material in industrial production due to its strong resistance to hydrogen, convenience and low cost.

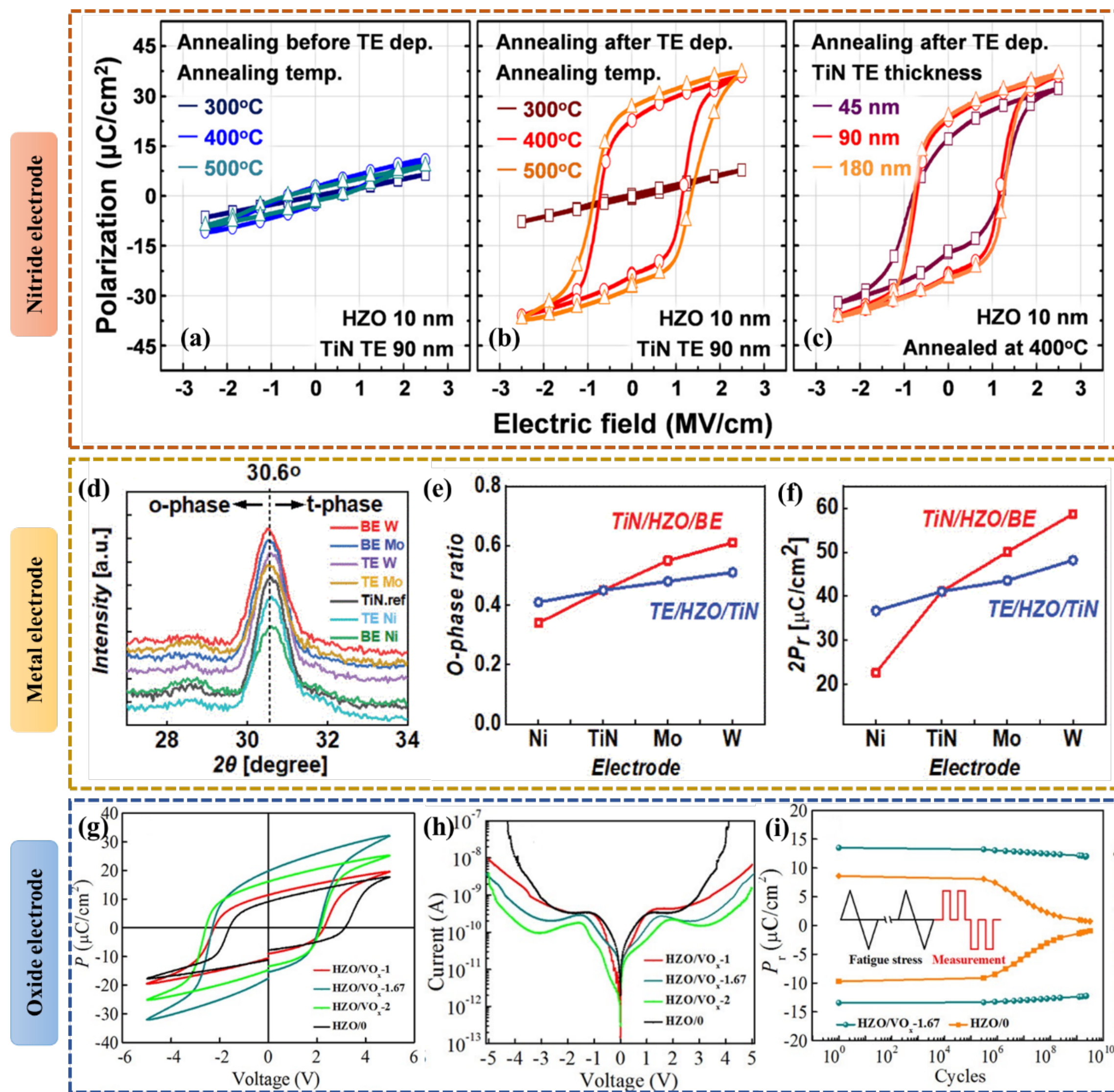

FIG. 7. P - E curves of HZO films annealed (a) before deposition of top electrode, (b) after deposition of TiN top electrode and (c) with various thickness of TiN top electrode.[116] (d-f) GIXRD patterns of HZO films using different electrodes, and the summary of o-phase ratio and $2P_r$ for all structures.[120] (g-i) P - V loops, leakage current, endurance, and retention properties of VO_x - capped HZO films. [125] Reproduced from (a-c) Kim et al., Appl. Phys. Lett. 111 (24) (2017).[116] with permission of AIP Publishing; Reproduced with permission from (d-f) Lee et al., IEEE T. Electron. Dev. 68 (2), 523 (2021).[120] Copyright 2021, IEEE. (g-i) Zhang et al., ACS Appl. Mater. Inter. 12 (36), 40510 (2020).[125] Copyright 2020, American Chemical Society.

2. *Strain from substrates*

Substrates are crucial to determine the growth direction of films and can significantly influence the properties of the film, due to their different crystallographic orientation, lattice parameter and CTE. As shown in Fig. 8(a)-(c), Shiraishi *et al.* [128] investigated the effect of mechanical stress on the ferroelectricity of HZO films on Si, SiO_2 and CaF_2 substrates, respectively. All films were highly crystallized, and the diffraction peak near 30° in the XRD patterns moved towards higher angles with an increase in the CTE of the substrate. The HZO behaved simply as a dielectric on CaF_2 substrates due to the in-plane compressive stress. Combining formula (2) with Figure 8(b), it was concluded that ferroelectricity could be obtained under an in-plane tensile stress when using a substrate with a lower CTE. For example, the radius of the curvature could decrease after rapid thermal annealing and the final residual stress could be tensile in nature. Clearly, by combining TiN electrodes with SiO_2 substrates, HZO films could achieve strong ferroelectricity due to the contribution to a tensile stress and the formation of a ferroelectric phase.

According to Stoney's equation, the residual stress can be calculated by the following formula:

$$\sigma_c = \frac{E_s}{6(1-\nu_s)} \frac{t_s^2}{t_c} \left(\frac{1}{R} - \frac{1}{R_0}\right) \quad (1)$$

Where t_s is the substrate wafer thickness (silicon in this case), t_c is the film thickness, E_s is the substrate elastic modulus (130 GPa), ν_s is the Poission's ratio (0.28) and R_0 and R and are the radius of curvature before and after coating, respectively. Due to the different CTEs of the films from the top electrode and bottom electrode, the final curvature can be quite different.

Yttria-stabilized zirconia (YSZ) is recognized as the most popular epitaxial substrate due to its similar cubic fluorite structure and a lattice constant close to HfO_2 (YSZ: a=5.12 Å, *o*-HfO_2: a=5.24 Å).[129] As shown in Fig. 8(d) and Fig. 8(e), Li *et al.*[129] fabricated epitaxial HZO films on TiN buffered YSZ substrates with different orientations. It is observed that the $o_{(111)}$-phase is more easily formed with HZO films epitaxially growing on a $TiN_{(111)}/YSZ_{(100)}$ substrate. A larger 2θ value of 43.7° for $HZO/TiN_{(111)}/YSZ_{(100)}$ compared to other epitaxial films was attributed to the applied compressive stress in the out-of-plane direction. The anisotropic stress can lead to a significant difference in the ferroelectricity of HfO_2-based films. Katayama *et al.* fabricated epitaxial and textured $Y_{0.07}Hf_{0.93}O_2$ films on indium tin oxide buffered YSZ substrates (ITO/YSZ) and Pt substrates using a pulse laser deposition (PLD) technique. [130] Stronger ferroelectricity was found for $Y_{0.07}Hf_{0.93}O_2$ grown on ITO/YSZ substrate due to much smaller lattice mismatch between YHO (3.653 Å) and ITO (3.594 Å) compared to that between Pt (2.774 Å) Y: HfO_2 films. The epitaxial growth of YHO along the YSZ substrate was also verified by XRD 2θ-ψ mappings,[131] as shown in Fig. 8(f) and Fig. 8(g). YHO-5, YHO-6 and YHO-7 showed a super-lattice diffraction as a result of a relaxation of strain through the formation of ferroelectric domain. Mimura *et al.*[132] investigated the temperature-dependent crystalline phase and ferroelectricity of epitaxial $Y_{0.07}Hf_{0.93}O_2$ on a YSZ substrate. It was reported that high temperature annealing (1000°C) could benefit for the formation of *o*-phase. In addition to Y: HfO_2, other HfO_2 doped films could be epitaxially grown on YSZ substrates.

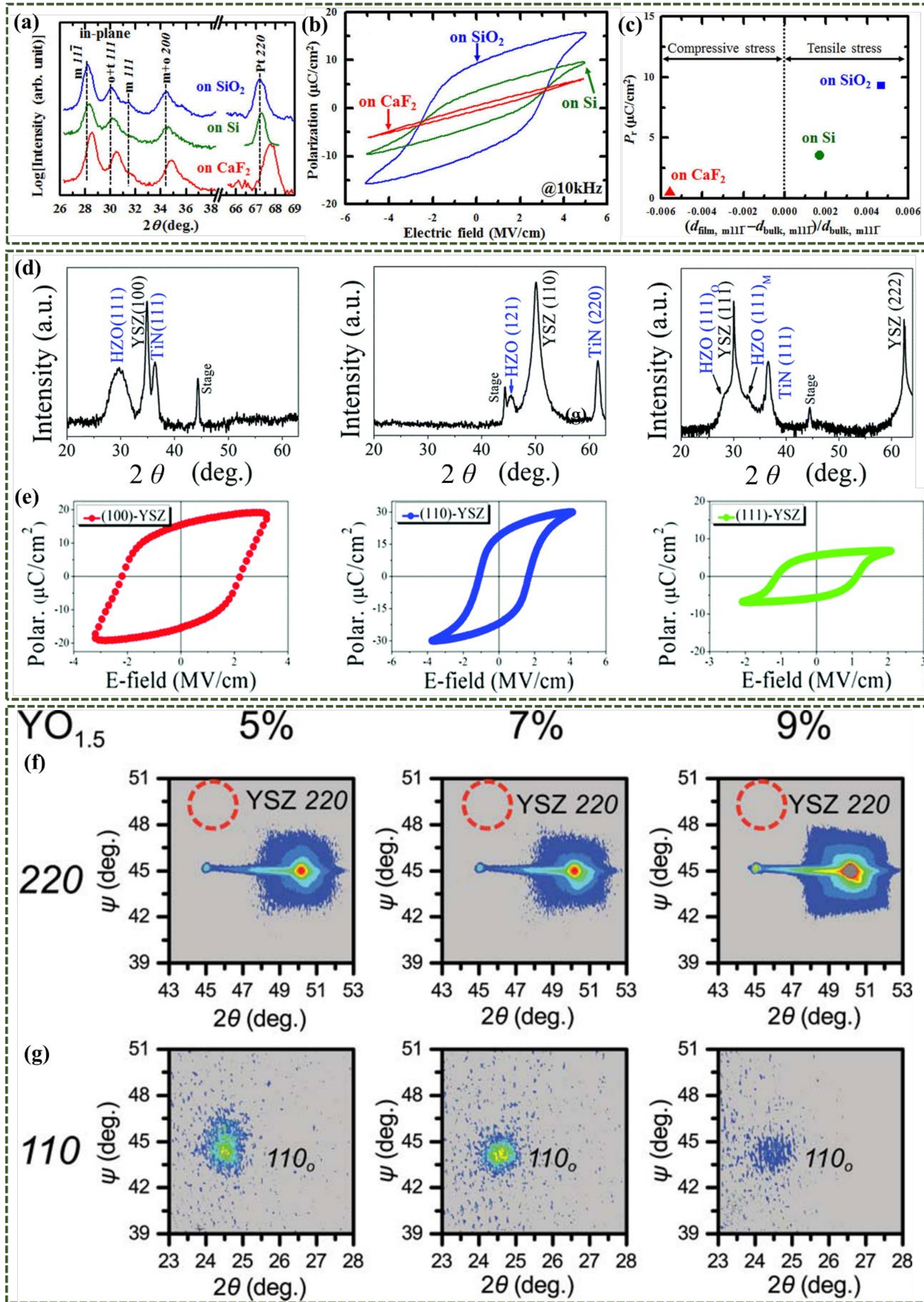

FIG. 8. (a) GIXRD characterization, (b) *P* - *V* loops and (c) influence of stress conditions on P_r values for HZO films grown on SiO_2, Si and CaF_2 substrates.[128] (d) XRD patterns and (e) P - E loops of HZO grown on YSZ substrates with different

orientations.[129] 2θ-ψ scans of epitaxial Y:HfO_2 films with different Y concentrations around (f) 220 and (g) 110 diffractions spots.[131] Reproduced from (a-c) Shiraishi et al., Appl. Phys. Lett. 108 (26) (2016),[128] with permission of AIP publishing. Reproduced with permission from (d-e) Li et al., J. Mater. Chem. C 6 (34), 9224 (2018).[129] Copyright 2018, Royal of Society Chemistry; (f-g) Shimizu et al., Ferroelectrics 512 (1), 105 (2017). [131] Copyright 2017, Taylor & Francis;

In order to further increase the level of ferroelectricity, endurance and reliability of HfO_2-based films, single crystal substrates with low defect concentrations have been employed including $SrTiO_3$ (STO), monocrystalline Si, and $La_{2/3}Sr_{1/3}MnO_3$ (LSMO) substrates. [112,129,133,134] As shown in Fig. 9(a) and Fig. 9(b), Li *et al.*[135] studied the electrical properties of Si: HfO_2 films through fine tuning the strain states of Nb-doped STO (NSTO) with different orientations. The XRD results indicated that the Si: HfO_2 films grew along the direction of the (001) NSTO substrate, but with a rotation of 45° along the (110) NSTO substrate due to their large lattice mismatch. The large lattice mismatch could kinetically control the structure alternatives upon phase transition and lead to enhanced Hf adsorption and O diffusion.[136] P_r values firstly increased and then decreased with increasing film thickness for Si: HfO_2 films grown on all substrates. The interface strain can also be relaxed by increasing the film thickness, which is ascribed to the splitting of diffraction peaks. Lyu *et al.* reported on the robust ferroelectricity of HZO films that were epitaxially grown on $La_{2/3}Sr_{1/3}MnO_3/SrTiO_3$ (LSMO/STO) substrate, with a P_r of 20 μC/cm^2 that did not exhibit a wake-up process, and exhibited a long retention beyond 10 years.[137] The peak position of epitaxial films shows a small

shift due to a volume expansion of 1.1% associated with the epitaxial orientation of substrates compared to that of polycrystalline films. Song *et al.* comprehensively investigated the ferroelectric properties of La: HZO films with a large endurance over 10^{10} years that was epitaxially grown on STO and STO/Si substrates.[133] Recently, a large P_r of 34 μC/cm^2 was also achieved in HZO films grown on STO/Si(001) templates. [138] A high level of ferroelectricity was successfully achieved in a 1 nm-thick $Hf_{0.8}Zr_{0.2}O_2$ film formed by an ALD technique on a Si substrate.[139] The pre-formed SiO_2 layer by thermal oxidation can provide a compressive stress for the formation of the ferroelectric *o*-phase. [128] An enhanced distortion originated from the mechanical confinement on the ultrathin film and the inversion asymmetry. The ferroelectric properties were stabilized in single crystal Y: HfO_2 bulk materials fabricated by a laser-diode-heated floating zone (LDFZ) technique due to its ultrafast heating and cooling capability.[33]

As shown in Fig. 9(c)-(f), Estandia *et al.* studied the dependence of epitaxial stress on ferroelectricity of HZO thin films by growing HZO films on a series of single crystalline substrates.[140] XRD results showed that HZO films were constrained under different stress conditions due to the different lattice parameters of substrates. The intensity of the *o*-phase was much stronger for HZO grown on substrates with larger lattice parameters. A P_r of ~ 25 μC/cm^2 was obtained for HZO films on $TbScO_3$ and $GdScO_3$ substrates. The LSMO was under tensile strain due to a large lattice constant of substrates, which could promote the epitaxial stabilization of the *o*-phase and provide ferroelectric properties. The mechanical strain could also be influenced by the

deposition temperature, oxygen pressure, and film thickness, which finally could modulate the ferroelectricity. [141,142]

While significant improvements have been achieved in HfO_2-based films, all films continue to exhibit polycrystalline structures and a single crystal structure has rarely been fabricated. It is believed that a higher level of ferroelectricity can be achieved in HfO_2-based films by increasing the tensile stress through selection of the appropriate electrodes and preparing textured films through adopting oriented substrates or single-crystal substrates. Therefore, highly oriented HfO_2-based films are desired and commonly fabricated on an epitaxial substrate or by limiting the film thickness to very small values, in the range of 1-10 nm.

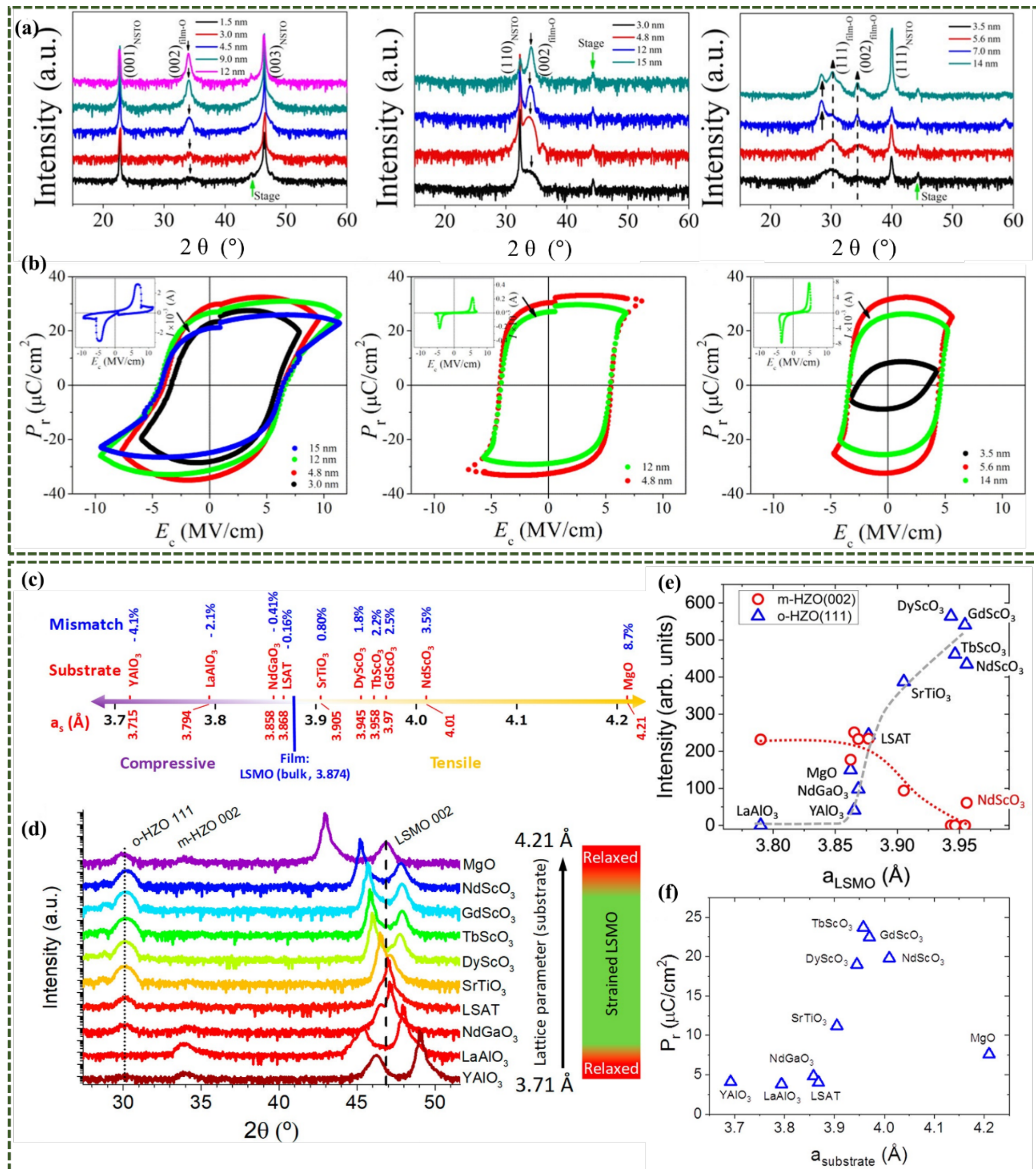

FIG. 9. (a) XRD θ – 2θ scans and (b) *P* - *E* loops of Si:HfO_2 grown on NSTO substrates with different orientations.[135] (c) lattice mismatch schematic between LSMO and substrates, (d) XRD θ – 2θ scans, (e) intensity of o-phase and (f) P_r values as a function of lattice parameter of the substrate.[140] Reproduced with permission from (a-b) Li et al., ACS Appl. Mater. Inter. 11 (4), 4139 (2019).[135] Copyright 2019, American Chemistry Society; (c-f) Estandia et al., ACS Appl. Electron. Mater. 1 (8), 1449 (2019).[140] Copyright 2019, American Chemistry Society.Surface and interface energy

The bulk energy and surface energy of the *o*-phase are both larger than those of the *m*-phase and *t*-phase in HfO_2-based materials. The free energy of a single grain can be calculated by Formula (2),[57] where the free surfaces and interfaces can both contribute to the whole Gibbs free energy. The size driven phase transformation from the *m*-phase to the *t*-phase/*o*-phase on the nano-scale is utilized to decrease the formation energy of the *o*-phase. The grain size can be reduced through the limitation of grain growth by decreasing the film thickness, constructing nano-laminate structures, and using a reducing annealing temperature. The surface energy effect has proven to be important in stabilizing the polar *o*-phase of HfO_2-based films, and ferroelectricity could be weakened or even disappear with an increase of film thickness and larger grain sizes.[76,123,143,144]

$$G_{grain} = G_{bulk} + \frac{2\pi r^2 \gamma_{if} + 2\pi r t \gamma_{gb}}{\pi r^2 t} \qquad (2)$$

Where G_{grain}, G_{bulk}, γ_{if} and γ_{gb} are the free energy of the grain and bulk, and the interface energy per unit volume, and grain boundary energy, respectively.

The *t*-phase of HfO_2 and ZrO_2 films will be stabilized when the film thickness decreases to 4 nm and 32 nm, respectively.[145,146] The same thickness-dependent ferroelectric behavior was observed in ALD-deposited Si-, Al-,Y- and La- doped HfO_2, and even undoped HfO_2 films.[22] HfO_2-based films with a smaller thickness always exhibited a higher level of ferroelectricity. As shown in Fig. 10(a) and Fig. 10(b), Mittmann *et al.* compared the ferroelectric behaviors of undoped HfO_2 fabricated by a sputtering method.[110] The rate of decrease in $2P_r$ with increasing the thickness was more rapid in ALD-derived HfO_2, compared to PVD-deposited HfO_2. Defects formed in

PVD-deposited HfO_2 such as oxygen vacancies and carbon can impact the phase transition and decrease the free energy of the *o*-phase. In addition, undoped HfO_2 with a smaller thickness displayed stronger endurance because of the contribution of additional *o*-phase. Polakowski *et al*. reported that a decrease in the grain size in HfO_2-based films of small thickness could stabilize the *o*-phase due to the large surface energy.[22] In this case, the surface energy, rather than bulk energy, contributes to the improvement of ferroelectricity.[57] In previous studies, the size-induced monoclinic to tetragonal phase transition was also reported in HfO_2-based powders and thin films.[145,146] Liao *et al.* reduced the grain radius of HZO by controlling the ALD cycle ratio.[147] A maximum $2P_r$ of 41 μC/cm^2 was achieved for a 5/5 HZO film with an average grain size of ∼13 nm. The excellent level of ferroelectricity was attributed to a small grain size, which was lower than the critical size of 14.5 nm, calculated according to Vagard's law, as shown in Formula (4). An accelerated phase transition was accomplished in a HfO_2/ZrO_2 nano-laminate through optimizing the single layer thickness.[148,149] Recently, Shin *et al.* realized ferroelectricity in HfO_2 nano-dots with a diameter of only 10 nm, and the level of ferroelectricity obtained was even larger than epitaxial HfO_2 thin films.[150] Chen *et al.* characterized the dependence of grain size on the ferroelectric switching behavior by PFM,[151] as shown in Fig. 10(c)-(d). The effective d_{33} could represent the spontaneous polarization in films, and showed a decreasing trend with the increase of grain sizes, indicating a stronger ferroelectricity at smaller grain size. In summary, the enhancement of ferroelectric properties of HfO_2-based films can be achieved through size and grain size effects.

$$d_{Hf_{1-x}Zr_xO_2} = (1-x)d_{HfO_2} + xd_{ZrO_2} \quad () \tag{4}$$

Where $d_{Hf_{1-x}Zr_xO_2}$, d_{HfO_2}, d_{ZrO_2} represent the grain size of $Hf_{1-x}Zr_xO_2$ solid solution, HfO_2 and ZrO_2 respectively, and x donates the atom ratio of ZrO_2.

In addition to decreasing film thickness, it is feasible to prevent the grains from growing by inserting an amorphous layer, or adopting CSD methods. As shown in Fig. 10(e), Kim *et al.*'s work demonstrated that the P_r can be degraded from 17 μC/cm^2 to 5 μC/cm^2 when the film thickness increased from 10 nm to 25 nm.[152] However, the ferroelectric properties can maintain at a high level with the addition of an Al_2O_3 interlayer, as seen from Figure 10(f). The existence of an interlayer effectively blocks the growth of grains in the HZO films, thus promoting the formation of the polar *o*-phase of small grain size. Moreover, the stabilization of the *o*-phase through a surface energy effect is common in the CSD-derived HfO_2-based films.[103,153] In our previous work, undoped HfO_2 films prepared by the CSD method exhibited a clear ferroelectric response in a wide range of thickness from 34 nm to 136 nm.[106] Excellent ferroelectricity can be obtained with small grain sizes even though the film thickness is relatively large, which is attributed to grain growth disruption through the layer-by-layer thermal treatment. The CSD method is also employed in fabricating other HfO_2-based ferroelectric films with a relatively large thickness, but is able to produce a ferroelectric response based on the surface energy effect, including Ca: HfO_2,[97] Sr: HfO_2,[96] Pr : HfO_2,[103] and Y: HfO_2[23,154].

For fluorite ferroelectric films, interfaces and grain boundaries are numerous, whose impact can also be indispensable. It is favorable to form HfO_2/ZrO_2 nano-

laminates due to potential for structural design and preparation convenience. As shown in Fig. 10(g), Weeks *et al.*[155] investigated the dependence of the individual thickness of the HfO_2/ZrO_2 layer on the ferroelectric behavior and structural variation. The maximum $2P_r$ was 50 μC/cm^2 in a (1 nm HfO_2/1 nm ZrO_2) × 4 nanolaminate after subjecting the material to a wake-up process at a deposition temperature of 285 ℃, which is even higher than a $HfZrO_2$ solid solution. The lattice distortion could lead to the ferroelectricity enhancement due to the different interface energy of neighboring HfO_2 and ZrO_2 regions. [156] The large ferroelectric response of the nanolaminates and superlattice was verified by quantitative analysis by simulation and experimental reports.[148,157-159] The construction of ferroelectric/dielectric bilayers is a popular approach for the improvement of ferroelectricity. As shown in Fig. 10(h)-(i), Si *et al.* reported that the Al_2O_3 (AO) thickness could play a decisive role on the polarization switching of AO/HZO stacks.[160] The ferroelectric response was firstly improved and then decreased with increasing AO thickness in the AO/HZO bilayers. In addition, the physical models behind the thickness relation before and after polarization switching have been proposed. If the externally applied voltage is zero, the ferroelectric layer is not polarized. If the dielectric layer is very thick, no polarization switching can occur since most of the applied voltage is consumed by the low-*k* AO layer which has a lower overall capacitance. When using an ultra-thin dielectric layer of higher capacitance, the ferroelectric layer can be fully polarized and the process can be assisted by the leakage charges from dielectric/ferroelectric (DE/FE) interfaces. Wang *et al.* enhanced the ferroelectric properties of AO/HZO bilayers due to the existence of capping stress

induced by interfacial mismatch.[161] Our group has also reported a large P_r of 24 μC/cm^2 and a decreased leakage current in AO/HZO bilayers due to the existence of an interfacial polarization.[162] Electronic charges can accumulate at the interface between DE and FE under the external electric field due to their permittivity mismatch and different interface energy. The seed layer of ZrO_2 was also shown to have a positive effect on the HZO films.[163] The existence of DE/FE interfaces can therefore make a significant contribution to ferroelectric polarization by an interfacial energy effect and boundary energy effect.

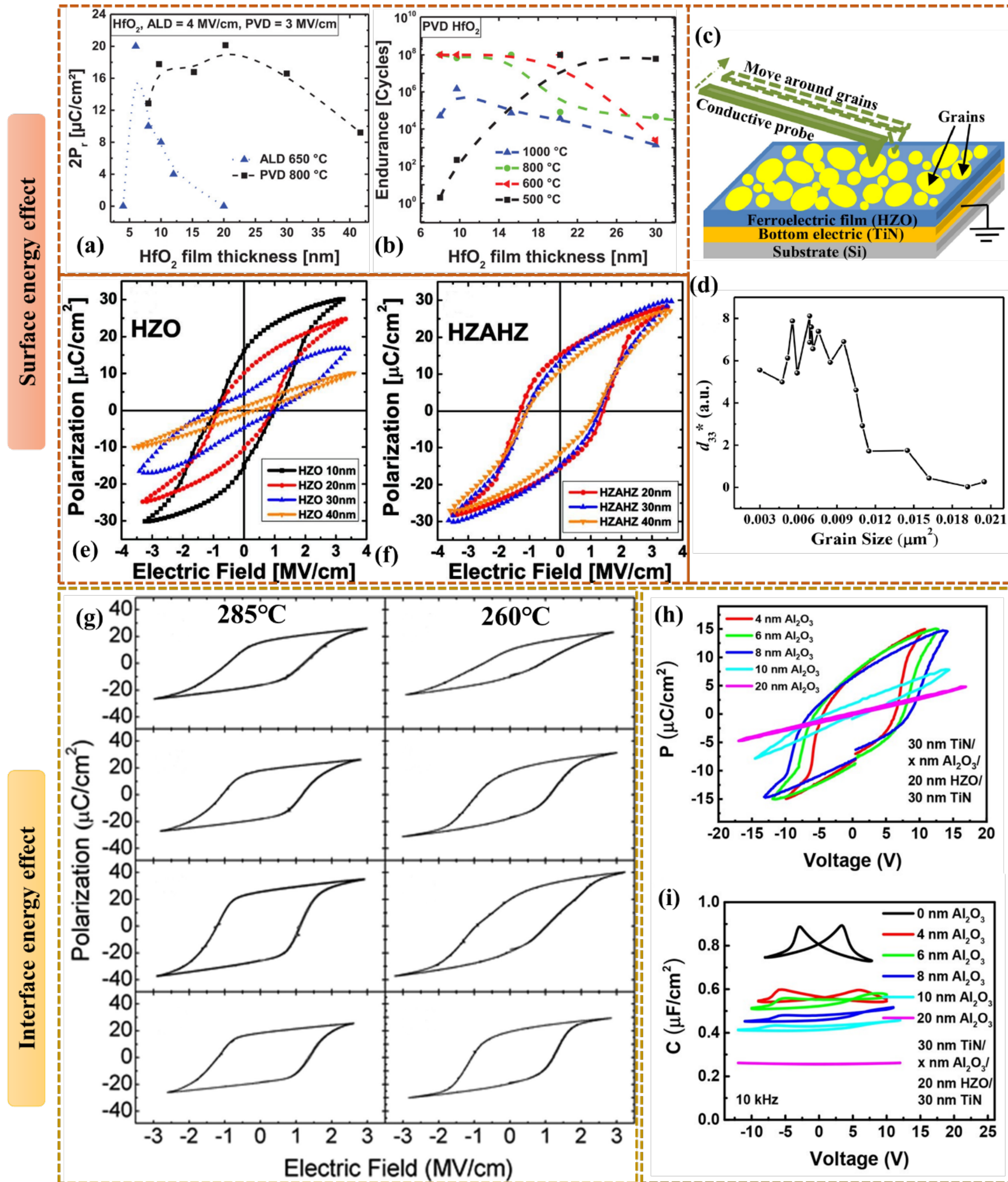

FIG. 10. (a) $2P_r$ values of sputtered undoped HfO_2, (b) endurance for undoped HfO_2 with different thickness using ALD and sputtering method.[110] (c) the testing schematic of grain sizes and (d) grain size dependent d_{33} values.[151] *P* - *E* loops of (e) HZO and (f) HZAHZ films. [152] (g) Comparison of *P-E* loops between HfO_2/ZrO_2 nanolaminates and $HfZrO_2$ solid solution deposited at 285 °C and 260 °C.[155] (h) *P* - *V* loops and (i) *C* - *V* curves of AO/HZO bilayers with different Al_2O_3 thickness.[160] Reproduced with

permission from (a-b) Mittmann et al., Adv. Mater. Interfaces 6 (11), 9 (2019).[110] Copyright 2019, John Wiley and Sons; (c-d) Chen et al., Int. J. Mech. Sci. 212 (212), 106828 (2021).[151] Copyright 2021, Elsevier Ltd.. Reproduced from (e-f) Kim et al., Appl. Phys. Lett. 105 (19) (2014),[152] with permission of AIP publishing. Reproduced with permission from (g) Weeks et al., ACS Appl. Mater. Inter. 9 (15), 13440 (2017).[155] Copyright 2017, American Chemistry Society; (h-i) Si et al., ACS Appl. Electron. Mater. 1 (5), 745 (2019)[160] Copyright 2019, American Chemistry Society.

IV. CHALLENGES OF THE WAKE-UP EFFECT AND FATIGUE PROCESS IN HFO_2-BASED FILMS

In previous sections, the structures and strategies for improving ferroelectricity in HfO_2-based ferroelectric films have been systematically overviewed. However, there continues to remain challenges associated with the practical application of HfO_2-based films in ferroelectric memories, including the *wake-up* effect, *fatigue* and *imprint* problem. As shown in Fig. 11, Schenk *et al.* analyzed three phenomena including the wake-up effect, split-up/merging and the fatigue processes by the first-order-reversal-curve (FORC) measurements, and concluded that the non-uniform distribution of built-in electric field led to the presence of divided current peaks.[164] In a pristine condition, two current peaks appear in the first quadrant and the *P-V* loops are rather constrained and slim. The current peaks are merged into a single current peak, along with improved P_r values after the wake-up process. With a further increase in cycles, fatigue phenomena appear to be accompanied with a decrease in P_r and a reduced intensity of

current peaks, see the lower image in Fig. 11. The recent *split-up effect* discovery led to the *P-E* loops exhibiting a pinned shape, see right image in Fig 11. Two or more current peaks appear when the applied electric field is smaller than the coercive field, and when cycling of the film is undertaken at higher voltage, the split-up effect disappears.

Both the wake-up effect and fatigue can lead to a decrease in endurance and a shortening of the service life of devices. Previous reports have shown that charge trapping at oxygen vacancies sites can cause these reliability problems.[165-167] This section will therefore discuss the wake-up effect and fatigue behavior in more detail.

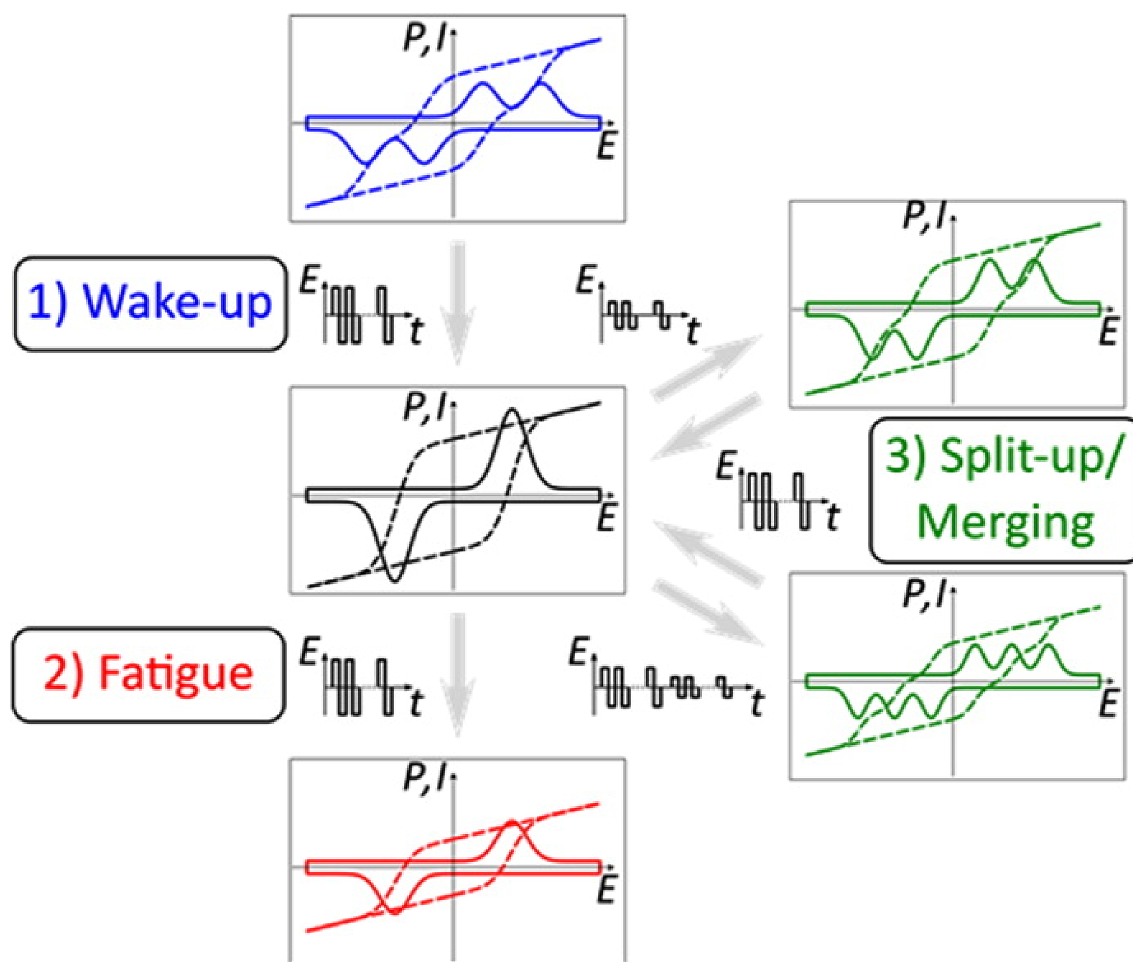

FIG. 11. Three phenomena including wake-up, fatigue and split-up/merging process during electric field cycling. [164] Reproduced with permission from Schenk et al., ACS

Appl. Mater. Inter. 7 (36), 20224 (2015).[164] Copyright 2015, American Chemistry Society.

A. Wake-up effect

The *wake-up* effect is a special phenomenon in HfO_2-based films during cycling measurement, which can be attributed to the redistribution of oxygen vacancies or electric field induced phase transitions. The cycling-dependent ferroelectric behavior regarding the wake-up effect was initially investigated by Zhou *et al.* [168] As shown in Fig. 12(a) and Fig. 12(b), the initial *P-V* loops behaved as pinched hysteresis loops and then became more open, with a gradually weakened built-in electric field after 1000 cycles. It is thought that the local dipoles are under a constraint condition and pinned by oxygen vacancies. The application of a cyclic electric field can activate the oxygen vacancies, and finally relax the dipoles and promote the improvement of the remnant polarization, P_r. Lower frequencies and higher voltages are able to accelerate the wake-up process since the migration/diffusion of charge carriers need time (frequency) and a driving force (voltage). The redistribution of oxygen vacancies has also been verified by researchers and suggested to explain the wake-up effect. [117,169] Another mechanism related to an electric field-induced phase transition has also been proposed. As shown in Fig. 12(c) and Fig. 12(d), Kim *et al.*[170] found that the phase transition from the *t*-phase to *o*-phase was achieved through cyclic measurements. The dielectric constant was significantly decreased due to the phase transition from a higher-*k* *t*-phase to a lower-*k* *o*-phase. Lomenzo *et al.* also confirmed the similar phenomenon of a phase transition from a distorted anti-ferroelectric to a ferroelectric after only 100 cycles. [118]

The estimated interface capacitance obtained from the pulse switching measurement increased with increasing the number of cycles, implying a decrease of the interface volume. The electric field-induced phase transition in the interface region was observed clearly through STEM measurements by Grimley *et al*.[171] The transformation from the *m*-phase to the polar *o*-phase in bulk grains, and the diminishment of non-uniform and defect-rich *t*-phase in interface grains can also explain the wake-up effect which leads to a higher P_r and an increase of interface capacitance.

In order to separate charge movements from phase change effects on the wake-up effect, Mehmood *et al.* investigated the influence of temperature on the ferroelectricity of La: HZO films, [172] as shown in Fig. 12(e)-(h). Higher ambient temperatures led to an increase in P_r values and a decrease in saturation polarization (P_{sat}), which was accompanied with a great influence on back-switching current peaks. For a woken-up sample, the dynamic hysteresis only began to exhibit tilting with a slightly higher P_{sat} and narrower current peaks. The initial improvement of P_r was attributed to the depinning of ferroelectric domains. However, the existence of interfacial regions can lead to a phase change and a variation of the coercive field. As shown in Fig. 12(i)-(k), Lee *et al.* reported on the nucleation-limited polarization switching with respect to defect concentrations through Monte Carlo simulation.[173] The switched polarization is highly related to the external voltage for both the initial and woken-up samples, which can be ascribed to the interactions of dipolar defects. The Lorentzian distribution was calculated to be largely broader using Kolmogorov−Avrami−Ishibashi (KAI) model as the defect concentration increases.[174] The simulated domains nucleated and grew

through domain-wall motion, which were easily formed in the more defective samples. The disorder caused by oxygen vacancies and charged defects could effectively promote the improvement of the remnant polarization, and result in a wake-up effect.

To further understand the intrinsic mechanisms, Pešić *et al*. simulated the diffusion of oxygen vacancies and distribution of electric field in Gd:HfO_2 films using a kinetic Monte Carlo simulation.[175] As shown in Fig. 12(l) and Fig. 12(m), charged defects were accumulated at the interface in the pristine state, which caused a high built-in electric field, especially near the lower electrode. Charged defects, such as oxygen vacancies, have been reported to induce an inhomogeneous electric field by a variety of researchers.[90,117,169,176] With an increase of field cycles, oxygen vacancies and interstitial ions can drift or diffuse into the films and the distribution of electric field becomes more uniform. The depinning of domains due to the relaxation of oxygen vacancies can promote the improvement of P_r, as shown in Fig. 12(n). Gb: HfO_2 can therefore show stronger ferroelectricity due to the existence of appropriate oxygen vacancies. [177] However, excessive oxygen vacancies can cause a decrease of reliability because of the higher leakage and reduced resistance to breakdown.

The redistribution of oxygen vacancies has been recognized to be the key impact factor for the *wake-up* effect and surface energy of different phases. In addition, an electric field-induced phase transition can also be induced through the movement of oxygen vacancies. [178,179] However, there are also other proposed mechanisms for the wake-up effect. Shimizu *et al*. reported that oxygen vacancies had no contribution to the wake-up effect.[180] The obtained ferroelectricity for HZO films was at similar levels

whether annealed under N_2 or O_2 atmospheres, and the final P_r values were dependent weakly on the applied frequency and measuring temperature, which indicated that the ferroelectricity was not related to the oxygen vacancies, but to the lattice ion displacement. The forming gas for annealing was also observed to have little impact on the ferroelectric properties of HfO_2-based films, suggesting its strong resistance to hydrogenation compared to traditional perovskite-structured materials.[86] Other factors such as annealing temperature [117,144] and electrode materials [181] can also affect the wake-up effect.

A similar *wake-up* effect was also discovered in perovskite-structured ferroelectrics, [182,183] but the problem could be readily solved using oxide electrodes such as IrO_x. For HfO_2-based devices, the control of oxygen vacancies is also used as an important strategy to reduce the wake-up effect and improve stability. Goh *et al.* used RuO_2 as oxide electrodes which successfully resulted in excellent switching properties.[126] The fastest switching speed and reduced *wake-up* process were achieved for HZO capped with both RuO_2 upper and lower electrodes, which was due to the good quality of the interface and fewer defects. TiN as oxyphilic electrodes can pull oxygen out of HZO, which leads to the generation of defects at the interface. However, RuO_2 as an oxygen donor electrode can supply oxygen for HZO, which can decrease the defect concentration.

In addition to using oxide electrodes, controlling the process condition is also considered to be a good strategy to obtain wake-up free HfO_2-based films with a lower concentration of oxygen vacancies. Kashir *et al.* obtained wake-up free devices through

increasing the ozone pulse duration during the ALD process.[184] It was reported by Mittmann *et al.* that the *t*-phase could be stabilized under a low oxygen content, while oxygen exposure could promote the formation of the *m*-phase.[185] Then, Kashir *et al.* investigated the influence of the ozone pulse duration, the annealing process, and the metal/insulator interface in detail on the wake-up process.[186] The suppression of the *t*- and *m*-phase is due to the high temperature annealing (700°C), longer ozone pulse length (30s) and large in-plane tensile stress induced by the W electrodes. A wake-up free condition was attributed to no phase transition from the *t*-phase to the *o*-phase. Recently, Kim *et al.* found excellent ferroelectric properties (2Pr: ~47.6 μC/cm^2) in HZO thin films without any annealing using cyclopentadienyl based precursors.[187] A carbon residue can be avoided and the films can crystallize into the *o*-phase without post-annealing at such a high deposition temperature (320 °C). Based on these investigations, the thermal budget is important to obtain wake-up free HfO_2-based films, and further studies are needed.

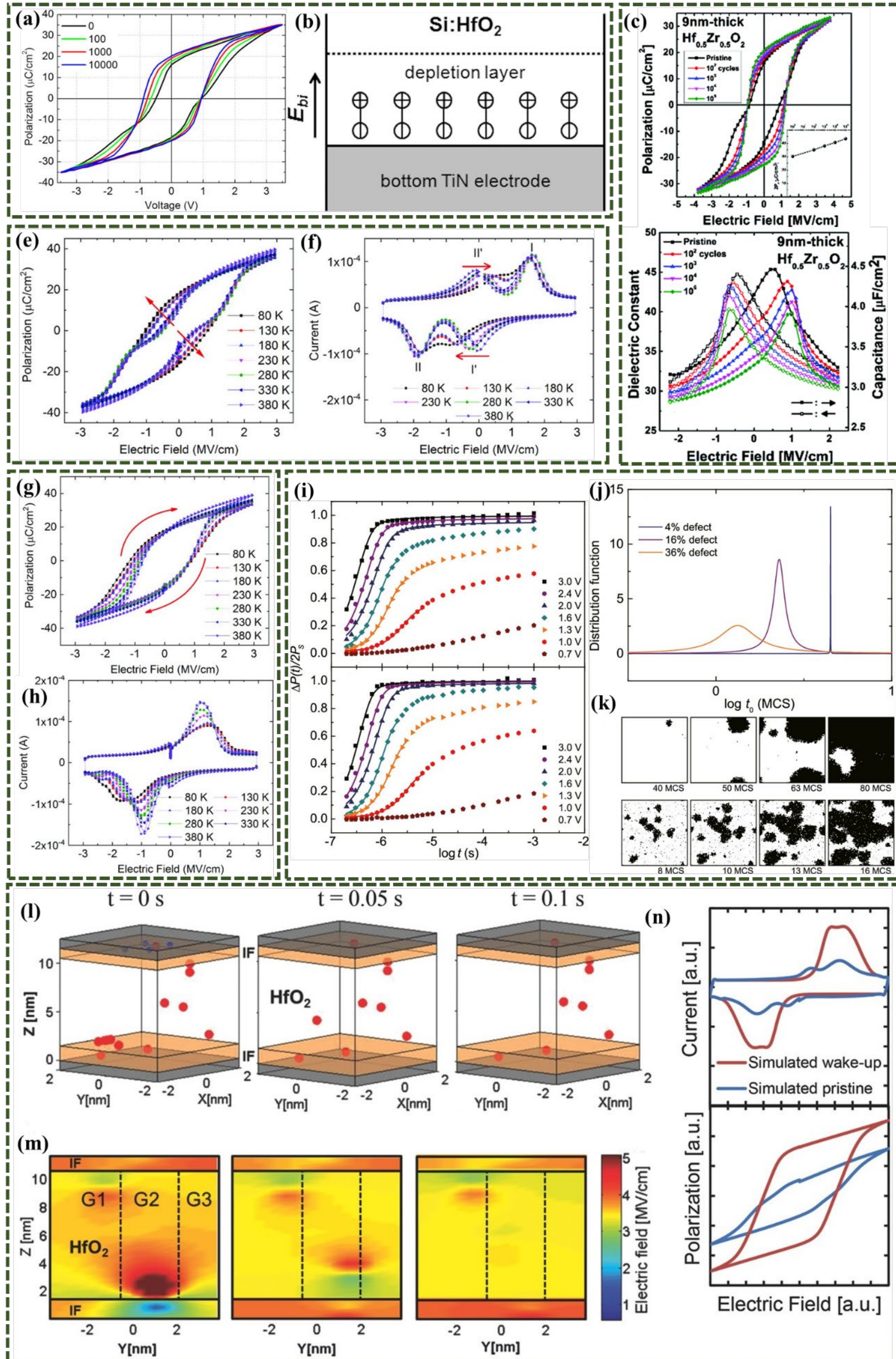

FIG. 12. (a) *P*-*V* loops under different cycles and (b) schematic of wake-up effect for

Si: HfO_2 film. [168] (c) P - E loops and (d) ε_r - E curves under different cycles of HZO film.[170] (e)(g) P - E loops and (f)(h) I - E loops for La: HfO_2 films under different temperatures before and after wake-up process.[172] (i) Polarization switching behavior as a function of voltage for the initial and wake-up samples, (j) Lorentzian distributions and (k) Snapshots of polarization switching with different defects concentrations calculated by Monte Carlo simulations.[173] (l) Oxygen vacancies diffusion and (m) electric field distribution with increasing cycling time, (n) simulated I - E and P - E loops.[175] Reproduced from (a-b) Zhou et al., Appl. Phys. Lett. 103 (19), 4 (2013), [168] with permission of AIP Publishing. Reproduced with permission from (c-d) Kim et al., Nanoscale 8 (3), 1383 (2016).[170] Copyright 2015, Royal of Society Chemistry; (e-h) Mehmood et al., Phys. Status Solidi A 217 (22) (2020).[172] Copyright 2020, John Wiley and Sons; (i-k) Lee et al., ACS Appl. Mater. Inter. 11 (3), 3142 (2019).[173] Copyright 2019, American Chemistry Society; (l-n) Pešić et al., Adv. Funct. Mater. 26 (25), 4601 (2016).[175] Copyright 2016, John Wiley and Sons.

B. Fatigue process

Fatigue is another critical problem which decreases the endurance of ferroelectric HfO_2-based thin films. A significant decrease of P_r and an increase of leakage current shows that the failure of the film can be caused by polarization fatigue and even hard breakdown. [117,170,181] The almost one order of magnitude lower activation energy of wake-up and fatigue effect for HfO_2-based films, compared to perovskite based PZT ferroelectric films, is mainly attributed to its high coercive field and larger surface to volume ratio. [188] In essence, HfO_2 is more likely to fatigue than perovskite-structured

films.

Regarding the fatigue behavior, oxygen vacancies generated at the grain boundaries and interfaces were considered to be the main reason for a higher leakage current after continuous electric field cycling. Pešić *et al*. found that a faster generation of oxygen vacancies occurred at the interface region by analysis using a thermochemical bond breakage model in MDLab software. [175] A stronger recovery can be observed with an increase in waiting time since more domains were de-trapped from the occupied oxygen vacancies. As shown in Fig. 13(a) and Fig. 13(b), Huang *et al*. investigated and analyzed the dependence of pulse parameters and temperature on the fatigue process of PLD-deposited Y: HfO_2 films. [189] The monotonous decrease of ε_r and P_r with electric field cycling was attributed to the phase transition from the ferroelectric *o*-phase to the paraelectric *m*-phase. The fatigue behavior was ascribed to the high-concentration on immobile domain walls, which originated from the trapped injected charge carriers at shallow defect centers from the passivation layer. The fatigue performance of the films after a heating and cooling process was also measured, as shown in Fig.13(c). The materials can maintain the same level of ferroelectricity after re-annealing of the sample due to the relaxed domains being pinned by oxygen vacancies. It was indicated that the degenerated ferroelectricity after the fatigue process can be recovered through an annealing treatment at 90 °C for 30 min.

Schenk *et al.* investigated the electric field cycling behavior of Sr: HfO_2 films under a range of applied frequencies and electric field cycles. [188] The split-up and fatigue phenomena can be explained by the movement of defects, where a higher Gibbs

energy barrier can lead to a higher coercive field. The defects are able to pin domain walls and inhibit the nucleation of domains at the interface regions near electrodes.[190] The existence of defects can accelerate the fatigue process, which is proposed to change the built-in electric field in the films. The fatigue performance is also closely related to other parameters including fabrication method, annealing condition, and elemental composition. Liu *et al*. comparatively investigated the ferroelectricity and endurance properties of Si: HfO_2 films, with the aid of Gibbs free energy calculations, as shown in Fig. 13(d). [191] The metastable *o*-phase can be stable under appropriate temperatures and moderate silicon doping levels. The fatigue behavior showed that a higher breakdown strength and fatigue resistance can be achieved in anti-ferroelectrics. The newly generated defects after continuous electric field cycles would lead to a decrease of the endurance and an increase of leakage current. In addition, the interaction between phonons and electrons during electric field cycling can lead to an increase of temperature at the domain region in films, which can lead to the thermochemical Hf-O bond breakage and promote the formation of a non-ferroelectric layer. [192] Fewer domain nucleation sites and a lower shared external field can trigger a decrease in P_r and lead to the onset of fatigue. More charges will be injected into films under applied external fields and the films will eventually breakdown with the buildup of defects achieving the limit.

Figure 13(e)-(f) show that the domain structures in La: HfO_2 films were relatively complicated, including 180° and 90° domain walls with head-to-head and tail-to-tail configurations. [193] When the samples were subjected to a fatigue condition, the domain

walls were pinned by aggregated charges and defects, leading to a decrease of P_r. Therefore, an oversaturated voltage should be applied to provide sufficient driving force and relax charges for the recovery of P-V loops. The domain pinning mechanisms were verified by studying the polarization switching behavior of La: HfO_2 films. The nucleation and growth of domains follow the nucleation-limited-switching (NLS) model for both fresh and fatigued La: HfO_2 films, which can be fitted with a inhomogeneous Lorentzian distribution and is consistent with PZT films. [194]

The above results demonstrated that oxygen vacancies and aggregated charges are dominant effects on the fatigue performance. Defect motion can be accelerated under higher temperatures due to a thermally activating process, which can lead to an increase in leakage current. The selection of appropriate electrodes can be an effective approach for the improvement of fatigue properties. [177,195] Avoiding the fatigue process is the eternal pursuit in semiconductor areas, which can provide a longer service life and improved practical applications.

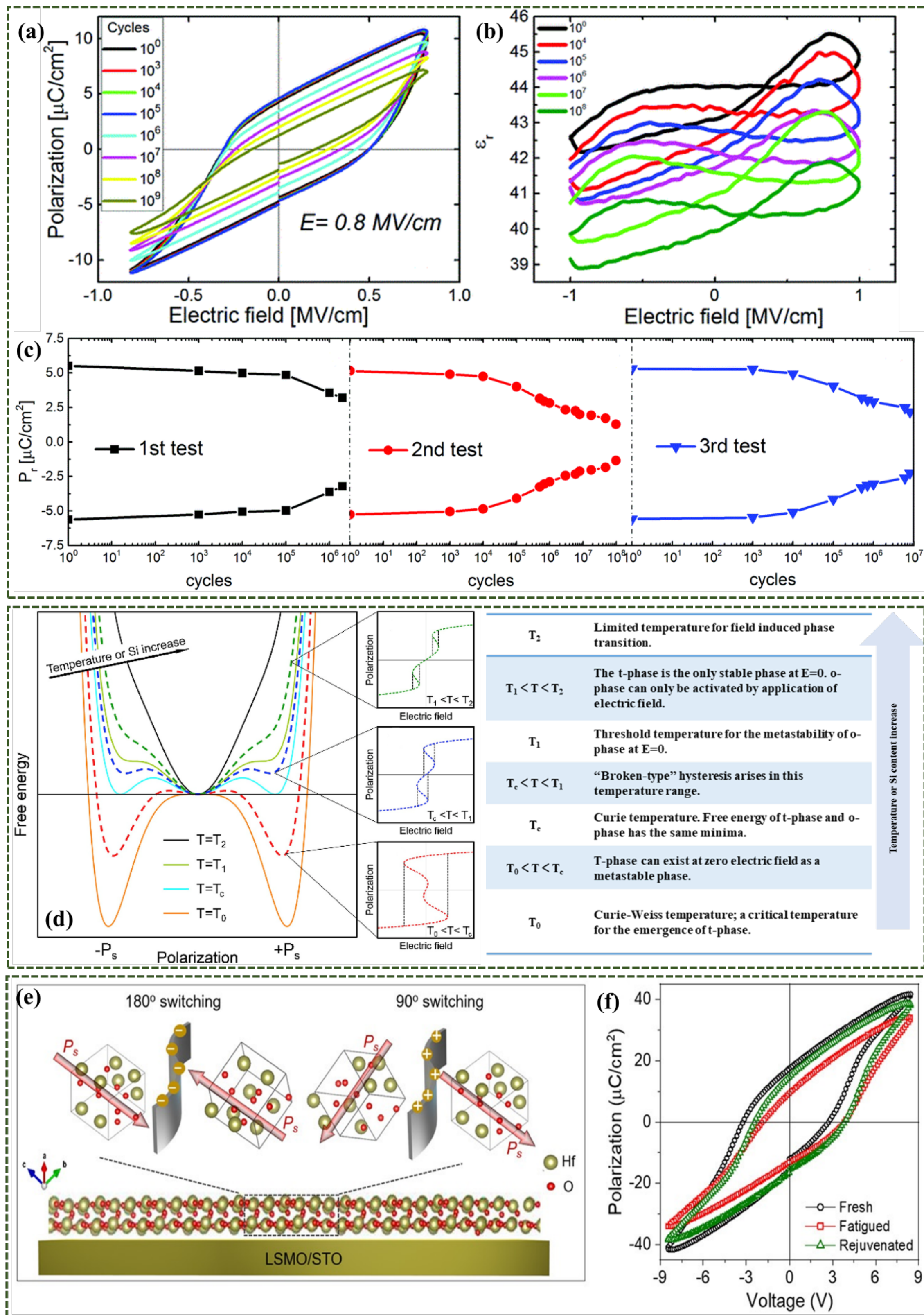

FIG. 13. (a) *P*-*E* and (b) *C*-*E* curves of Y: HfO_2 films under different field cycles. (c) First, second and third cycling test after heating and cooling process. [189] (d) Evolution of Gibbs free energy profiles and *P*-*E* loops of Si: HfO_2 films with increasing

temperature or Si content.[191] (e) Schematics for the possible 180° and 90° domain switching in the La: HfO_2 films, (f) *P–V* loops of the La: HfO_2 capacitors under fresh, fatigued, and rejuvenated conditions. [193] Reproduced with permission from (a-c) Huang et al., Phys. Chem. Chem. Phys. 19 (5), 3486 (2017).[189] Copyright 2016, Royal of Society Chemistry; (d) Liu et al., Acta Mater. 154, 190 (2018).[191] Copyright 2018, Elsevier Ltd; (e-f) Li et al., Phys. Status. Solid-R. 15 (4), 7 (2021).[193] Copyright 2021, John Wiley and Sons.

C. Additional technical issues

In addition to the wake-up effect and fatigue, there exist other important technical issues such as high temperature imprint and uniformity. Usually, the shift of the polarization-voltage hysteresis loops or nonsymmetric positive and negative coercive voltages can be shown in imprint phenomena with an increase of electric field cycles, which will lead to nonuniformity, an increase in operation voltage, the degradation of ferroelectric performance, and even write failure. The imprint voltage can be calculated by $V_{shift}=(V_{c+}+V_{c-})/2$, where V_{c+} and V_{c-} denote the positive and negative coercive voltages, respectively. As shown in Fig. 14(a)-(b), a clear time-dependent shift of polarization-voltage loops was observed by Takada *et al.*,[196] which indicated a typical imprint phenomenon, similar to reports on perovskite-structured films such as $BaTiO_3$ and Pb(Zr, Ti)O_3.[197,198] Firstly, the imprint was completely erased after 10^4 electric field cycles. Then, upward and downward polarization were set by applying pulses with a negative and positive amplitude for various durations. The final P-V loops were recorded at various holding times between the poling pulse and the current

measurements. The V_{c+} and V_{c-} are nearly equal to each other directly after the alternating pulse, which is attributed to the improvement of film uniformity during the wake-up process.[199] A significant shift of the coercive fields has been shown in the same direction as the polarization, which can be induced by the continuous accumulation of charges at the interfacial region during the holding time.

Takada *et al.* identified the contribution of redistributed charge, rather than dielectric relaxation, to the time-dependent imprint of various ferroelectric properties.[200] A weaker imprint behavior during time-dependent polarization retention has been reported in thicker films and PLD deposited films with lower defect densities, suggesting that the depolarization field is the driving force for charge redistribution. Meanwhile, the retention loss is not significant after a short time, and therefore relaxation is not the main cause. In order to verify the influence of mobile charges on the imprint behavior during retention tests, Chernikova *et al.* investigated the temperature-dependent dynamic imprint recovery of $Hf_{0.5}Zr_{0.5}O_2$-based capacitors.[201] The *I*-*V* and *P*-*V* loops in the initial state and after baking at P↑ and P↓ at 105 °C were shown in Fig. 14(c)-(d), respectively.[201] The initial imprint can be caused by the asymmetry between $Hf_{0.5}Zr_{0.5}O_2$/top TiN electrode and $Hf_{0.5}Zr_{0.5}O_2$/bottom TiN electrode interfacial region. A longer exposure to the atmosphere can decrease the work function and cause the oxidation of TiN bottom electrode, which can lead to a negative internal field. [202,203] A clear back-switching occurs after the removal of the electric field when using fast pulse measurements, however, nearly no back-switching can be observed in the sweep hysteresis measurements. Recently, Buragohain *et al.* proposed

the concept of a "fluid imprint", which presented that the charges can be continuously injected into and transported across the interfacial layer when the pulsed electric field was removed. [204] Domain recovery is accelerated during long sweep measurements, and thus no splitting current appears. Higashi *et al.* also investigated the voltage shift of the Al: HfO_2 ferroelectric capacitor. [205] The nucleation-limited-switching (NLS) model verified that the charge trapping and detrapping at the interfacial region are responsible for imprint and the recovery of voltage shift. Thus, more accumulated charges in one of the directions and the external applied electric field can lead to more imprint effects after being subjected to a bake.

In addition to the above electrical measurements, including time-dependent voltage shift and pulse switching techniques after bake, the domain structures are also visual evidence for the imprint effects during polarization reversal. Buragohain *et al.* studied the nanoscopic mechanisms using piezo-force microscopy (PFM) measurements combined with pulse measurements, as shown in Fig. 14(e)-(h).[206] The outward expansion of domains can be seen from Fig. 14(e), indicating the nucleation and growth process of domain walls. The lateral domain wall velocity increases with an increase of pulse width, as shown in Fig. 14(f), which is consistent with the change of switched charge. The unpinned domains can be rearranged into the same switching direction, and causes an imprint.[207] The Lorentzian distribution function in the NLS model fits the experimental data perfectly, in agreement with previous reports.[208] The defects or the pinned domains can become the nucleation centers and promote the switching behavior. Fengler *et al.* used an in-situ imprint measurement and two-step

waveform to analyze the root cause of the wake-up effect and imprint behavior.[167] Nearly no change in the dielectric constant indicated no pronounced phase transition in the wake-up process. The initial imprint behavior originated from the different orientations of grains due to processing conditions. [209,210] No splitting of the switching density can be shown after 10^6 cycles in the first order reversal curves (FORC), which is the result of domain reorientation, and local bias fields emerges and becomes stronger when baking at higher temperatures; this is again due to the pinned domains. Thus, oxygen vacancies at the defect sites are considered to be the root cause of imprint.

In order to increase the reliable operation and longer retention properties, it is necessary to optimize the interface quality and decrease the oxygen vacancies. It has been reported that Ge and $Si_{0.56}Ge_{0.44}$ semiconductors are recognized as good substrates for the growth of HZO, because there exists no interfacial layer and the reliability can be improved. [211-213] Zacharaki *et al.* also studied the influence of annealing processing of flash laser annealing (FLA) and rapid thermal annealing (RTA) on the imprint and wake-up effects.[214] The weak imprint and wake-up process were attributed to the clean HZO/Ge interface. In addition, a longer retention and lower leakage current could be achieved in FLA treated films, which originated from the insufficient diffusion of oxygen vacancies. Thus, the imprint and nonuniformity issues can be caused by the asymmetric interfaces and processing conditions. It is efficient to improve the retention performance through the formation of clean HZO/substrate interfacial layer and a decrease in the movement of charges. Further investigations are needed to explore the strategies to increase the uniformity of films and decrease imprint behavior.

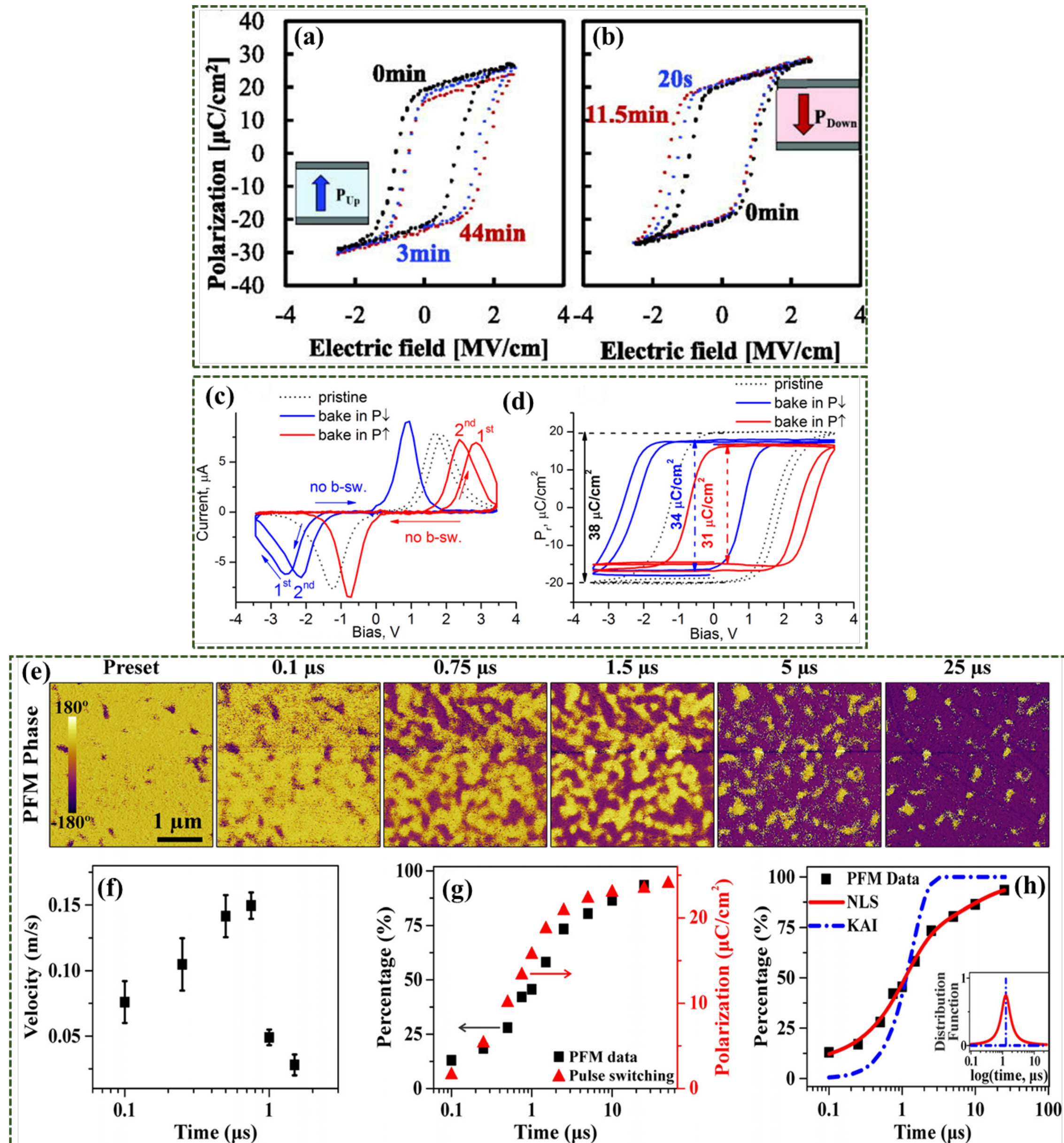

Fig. 14. *P-E* loops measured after maintaining the polarization in (a) upward and (b) downward directions.[196] Comparison of (c) *I-E* loops and (d) *P-E* loops in the pristine state and after bake at 105 °C in P↑ and P↓ directions.[201] (e) Domain configurations at different stages of polarization switching under a tip bias of 4.0 V with increasing duration, (f) time-dependent domain wall velocity obtained from (e), (g) comparison of switched area as a function of time between the PFM data and the pulse polarization,

(h) fitting results of PFM data using both KAI and NLS model.[206] Reproduced from (a-b) Takada *et al.* Appl. Phys. Lett. 119 (3) (2021),[196] (c-d) Chernikova *et al.* Appl. Phys. Lett. 119 (3) (2021),[201] (e-h) Buragohain *et al.* Appl. Phys. Lett.112 (22) (2018),[206] with permission of AIP publishing.

V. APPLICATIONS BASED ON FERROELECTRIC HFO_2-BASED FILMS

The excellent properties of HfO_2-based ferroelectric films enable them to gain widespread future practical applications, including non-volatile memories for the Internet of Things, bionic devices for human-computer interaction, and piezoelectric transducers. The range of application areas will be summarized in the following sections including ferroelectric random-access memories (FRAM), ferroelectric field-effect transistors (FeFET), ferroelectric tunnelling junctions (FTJ), bioelectronic synapse, and piezoelectric devices.

A. Non-volatile memories

With the rapid development of big data and cloud computing, the demand for non-volatile memories with large information storage capacity and fast computing speed faces challenging demands. Ferroelectric materials can be widely applied in non-volatile memories due to their different polarization states. Until now, ferroelectric memories have evolved from thick perovskite ferroelectric films to the more recent HfO_2 thin films, from single device to integrated electronics, from low speed to high operation power. HfO_2-based ferroelectrics are promising due to their excellent

ferroelectric behavior when formed in an ultrathin thickness, which can be coupled with their large breakdown strength, and large memory window. From the property parameters listed in Table III, it can be seen that HfO_2-based ferroelectric films have significant potential compared to traditional perovskite-structured materials to further advance non-volatile applications.

Table III. Comparison of coercive field (E_c) and the switched polarization ($2P_r$) for commercial SBT, PZT, PVDF-TRFE, and doped HfO_2. [35]

	SBT ($Sr_2Bi_2TaO_9$)	PZT	PVDF-TRFE	Doped-HfO_2
E_c (MV/cm)	0.05	0.1	0.5	0.8-2
$2P_r$ (μC/cm^2)	15-25	30-60	10	30-60

1. *Ferroelectric random-access memories (FRAMs)*

The operation of “1” and “0” can be accomplished in FRAMs by the polarization switching and non-switching access to the data storage and readout, [215] as shown in Fig. 15(a). The access time is relatively fast in FRAMs and power consumption is rather low. The capacitor density can be represented by the storage charge, as shown in Formula (6), which is proportional to the P_r and capacitor area.

$$Q = 2P_r A_{Cap} \quad (4)$$

The improvement in ferroelectric activity can largely promote the storage capacity of FRAM. In order to obtain high-density FRAM devices, the cell size should be scaled down as much as possible. However, the P_r was severely reduced in perovskite-based capacitors due to the thickness limitation and large leakage current below 130 nm, [216] as

shown in Fig. 15(b). Thus, 3D capacitors are pursued to solve the limitation. Park's groups compared the ferroelectricity of planer capacitor with stretch capacitors with different sizes,[216] as displayed in Fig. 15(c). The memory density of 256 Mbits was successfully achieved by decreasing the deep/radius (D/R) ratio of a PZT film from 0.25 μm to 0.13 μm. [216,217] The challenge of size limitation can be overcome in trench capacitors using HfO_2-based films due to its better ferroelectricity when formed in an ultrathin thickness, [81] as shown in Fig. 15(d). It is a breakthrough to successfully achieve the vertical integration of ferroelectric 1T/1C memories. The P_r value of 3D arrays (150 $\mu C/cm^2$) is much larger than the planar capacitors (~15 $\mu C/cm^2$), and the ferroelectric properties showed negligible degradation after 10^9 cycles, as shown in Fig. 15(e). The advantages of FE-HfO_2 including large P_r, small thickness and CMOS compatibility, which make it highly promising for the 1T-1C FeRAM. Fengler *et al.* systematically compared the properties of non-volatile FRAM using FE-HfO_2 with using PZT.[218] HZO and PZT could both exhibit good scalability and similar access time in the nanosecond range. However, ionic charge diffusion could occur at high frequencies, which led to a decrease of endurance in PZT. In HZO, the existence of oxygen vacancies in the interfacial region can be the main cause for the wake-up effect[182], and a detailed description of this phenomenon is discussed in the chapter 4.1. Lower-k of HZO and comparable ferroelectricity to the perovskites, could also be beneficial for the scaling down 3D FRAMs.

Mueller *et al.* investigated the properties of the 10 nm-thick Si: HfO_2 film, which showed a large dependence with processing conditions.[219] The endurance could only

achieve 10^6 cycles and was far lower than that of PZT-based FRAM capacitors. Despite the advantages of HfO_2-based FRAMs, there also exists challenges including a lower endurance (10^9 cycles) compared to conventional perovskites (10^{12} cycles) and large coercive field (1~2 MV/cm) that is almost near its dielectric breakdown strength (4~8 MV/cm).[220] While robust ferroelectricity can be obtained at high coercive fields, such high-voltage operation during retention can increase the risk of hard breakdown and lead to device failure. Meanwhile, the switching speed can be relatively low under the same external field. Thus, it is necessary to decrease the coercive field to control the operation voltage at a lower state. Yoo *et al.* reported on the frequency dependent polarization switching behavior of Si: HfO_2 with a variety of Si dopant concentrations and annealing temperatures, and proposed an avenue to decrease the E_c by controlling the grain size.[221] The coercive field (E_c) can increase with frequency due to the creep and flow motions according to the intrinsic domain-wall growth mechanisms and the E_c value can be reduced to 0.5 MV/cm through forming nanoscale grains in Si: HfO_2, and the final switching time can be much three times faster than those films with larger grain size and a higher E_c (1 MV/cm). Grenouillet *et al.* demonstrated the integration of HZO films in the Back-End-Of-Line using 130 nm CMOS technology, and the switching speed could be lower than 100 ns.[222] Okuno *et al.* recently reported on a 64 kbit 1T1C FeRAM array with integration of 1000 capacitors in parallel using HZO films with a high endurance and low-voltage operation.[223] Reliability at over 10^{11} cycles can be obtained at a low voltage of 2 V, which is beneficial for the practical use. The write and sense operations could maintain excellent uniformity with an external voltage

of 2.0 V, which can present a high speed of 16 ns. The ultra-high endurance at lower voltage makes FRAM promising candidates for future IoT applications. Huang et al. found that the ferroelectricity and endurance of Y: HfO_2 FRAM devices showed no difference after ^{60}Co γ ray radiation, which could be potentially of interest for nuclear and aerospace applications.[224]

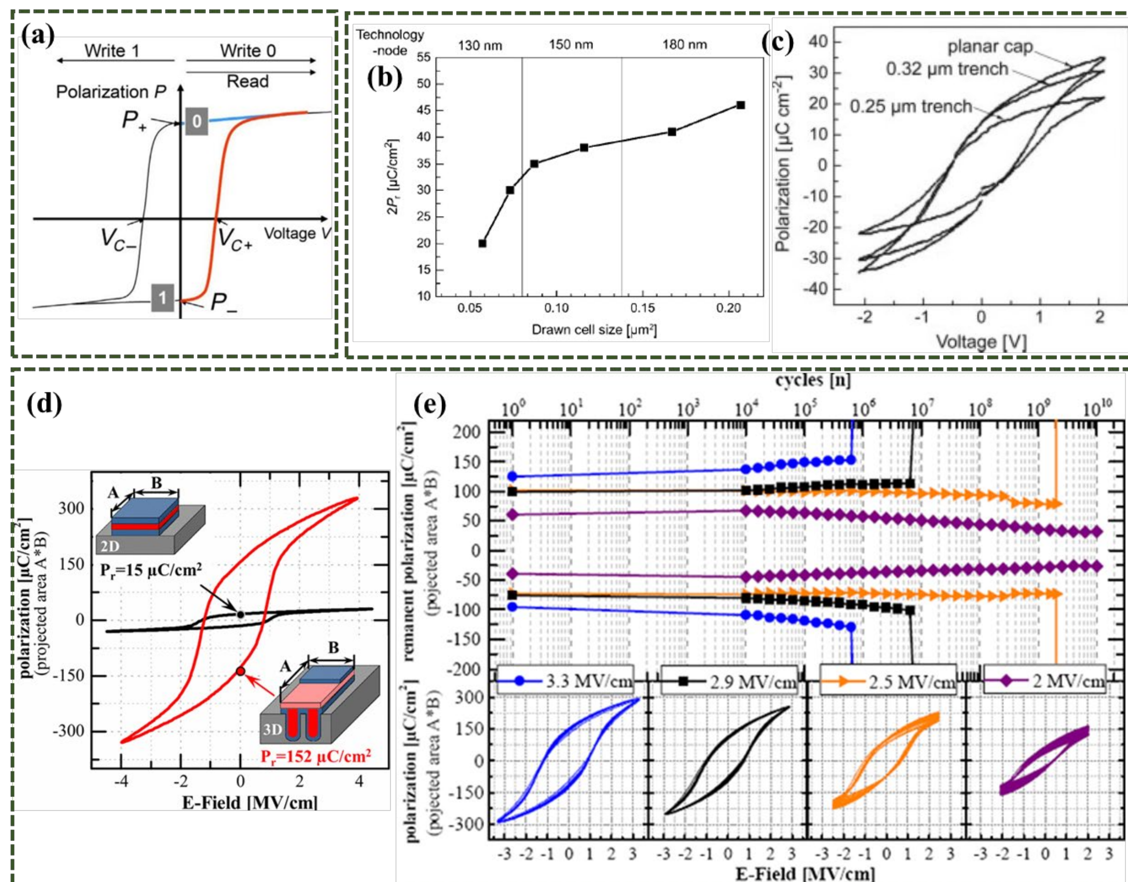

FIG. 15. (a) Readout mechanism of FeRAM.[215] (b) The relationship between Pr values and cell size for PZT and (c) *P-V* curves in PZT planar and trench capacitors.[216] (d) Comparison of *P-E* loops between a planar capacitor and 100k trench capacitor, (e) Schematic of 3D deep trench capacitor, and (f) Fatigue performance for Al:HfO_2-based 3D non-volatile memory.[81] Reproduced with permission from (a) Pešić et al., in Ferroelectricity in Doped Hafnium Oxide (2019), pp. 413.[215] Copyright 2019, Elsevier

Ltd; (b-c) Park et al., Ferroelectric Random Access Memory (2010), Nanotechnology. [216] Copyright 2010, John Wiley and Sons; (d-e) Polakowski et al., in 2014 IEEE 6th International Memory Workshop (2014).[81] Copyright 2014, IEEE.

2. *Ferroelectric field effect transistors (FeFETs)*

In an FeFET, the storage capacity can be represented by a memory window (MW), which is calculated by the formula (5):

$$\mathrm{MW} = V_{c+} - V_{c-} = 2E_c t_{FE} \qquad (5)$$

where E_c and t_{FE} are the coercive field and thickness of ferroelectric film, respectively. To obtain a large MW, the low E_c of perovskite ferroelectric films (SBT: 10-100kV/cm, PZT: 50 kV/cm [225,226]) should be compensated for by producing a large thickness, which could suffer from integrity issues, large electrostatic consumption, and poor scalability. A schematic diagram, TEM cross section, and transfer characteristics are shown in Fig. 16(a)-(c).[208] The polarization direction was determined by the gate voltage, which could also induce positive or negative charges at the HfO_2/SiON interface and generate a high or low V_T state. Müller *et al.* successfully fabricated a 28 nm gate-first High-K Metal Gate (HKMG) stack using Si:HfO_2 ferroelectric films, [227] which solved the existing issues due to the large E_c of HfO_2 (1-2 MV/cm). [228] The observed memory window was 0.9 V when the program/erase operation voltage was ±5V, with a fast operation speed of 20 ns, and the retention capability could be extrapolated to 10 years. Further technology scaling down to 22 nm using planar Fully Depleted Silicon-On-Insulator (FDSOI) was achieved by Carter and his co-workers.[229] The same group improved the HfO_2-based FeFET with an area of 0.025 μm^2 with an ultrafast operation in the 10 ns

range, which could fulfill the 12 nm technology node. [230] The history and forecast of physical gate length of FE-HfO_2 were also summarized according to the publication year of papers. A clear trend of FE-HfO_2 to replace perovskite ferroelectric films can be observed and the continuous decrease of film thickness is imperative. Since ferroelectricity was found to be stabilized even in 1 nm-thick doped HfO_2 film, [139] it is believed that the scaling (Moore's law [231]) is suitable for HfO_2-based FeFET performance.

The existence of an interfacial dielectric layer can lead to poor endurance of FeFETs, which can be an obstacle for their practical applications. Usually, a lower-k interfacial layer can be generated between the substrate/lower electrodes and the HfO_2 layer, which will act as a two-capacitor divider. Such interface compound can consume part of applied voltage and induce a voltage drop and a depolarization field. The increased charge trapping at the interface can be harmful to the reliability of FeFETs.[232] As a result, the endurance of devices can be largely limited. It is reported that an effective approach is to increase the endurance by decreasing the thickness or improving the dielectric constant of the interface oxide. Xiao *et al.* reported on an improved reliability of HZO FeFETs by inserting an seed layer of ZrO_2.[233] A stronger crystallization of the HZO films and the suppression of an interfacial trap could effectively enhance the memory window and the endurance of devices. As shown in Fig. 16(d)-(f), Kim *et al.* proposed a new approach of a spherical recess channel FeFET to improve endurance performance.[234] A middle metal layer was inserted between the ferroelectric layer and insulation layer, which could effectively increase the dielectric

constant of interfacial layer. The function is consistent with previous report using a higher-k material to replace the interfacial layer.[235,236] The MW and endurance were both enhanced with the increase of metal thickness. The decrease in electric field of the interfacial region could reduce the charge injection and trapping, which enhanced the reliability of devices. Tan et al. also reported an endurance exceeding 10^{10} cycles in HZO films by incorporating a high-k SiN_x layer (ε_r: ~ 7.8) between the Si substrate and the functional film. [237] The decreased charge traps can be induced by the reduced electric field in the nitride interfacial layer due to its higher permittivity compared to the SiO_2 interface, which counteracts the ferroelectric hysteresis and increases the endurance of devices.

Although planar HfO_2-based FeFETs or FeCaps have achieved interesting performance, the 3-D NAND devices are attracting interest due to their high density, low power and high speed. Florent et al. firstly demonstrated a vertical Al: HfO_2 device with endurance over 10 years at 85 °C for NAND applications.[238] Subsequently, the same group fabricated a HfO_2-based vertical macaroni-type 3D FeFET and the flash endurance could achieve 10^4 cycles and a MW of 2 V.[239] However, more trapped charges at higher operation voltages can be caused by interfacial defects which leads to retention issues and the non-uniformity of threshold voltages for these devices. In order to optimize the interfacial qualities, Kim *et al.* recently fabricated a potential ferroelectric NAND flash memory due to the synergistic effect of $HfZrO_x$ films and $InZnO_x$ channel layer with an endurance of over 10^8 cycles.[240] The introduction of an oxide semiconductor can avoid the formation of an SiO_x interfacial layer and avoid the

charge trapping in the ferroelectric layer, which is beneficial for stable endurance characteristics. In addition, each memory cell could show similar performance on the wafer scale in FeNAND and vertical FeTFTs, which is beneficial for high-density memories. The program and erase operation of 3D vertical channel FeFETs can be successfully executed to accelerate the vector-matrix multiplication, which is useful in memory computing.[241] Based on these advantages, 3D FeNANDs are potential structures in future ultra-high density memories and deep neural networks with high efficiency.

In addition to the fabrication of FeFETs on a rigid Si substrate, ferroelectric HfO_2 films can also be integrated with FeFETs on flexible substrates for the application of wearable devices. While it is possible to prepare HfO_2 films at high temperature on the rigid substrate, and then transfer them onto the organic substrate through remote epitaxy technology, [242] it adds complexity to the fabrication process and increases production costs. It was reported that a HZO film could be integrated into the vertical FETs (VFET) and ferroelectric properties were retained up to 1000 bending cycles at a bending radius less than 8 mm. [243] As shown in Fig. 16(g)-(i), band bending of the channel could be generated because of the different work function of ITO and C_{60}.[243] The accumulation of electric charges at the interfacial region caused by nonvolatile ferroelectric polarization could induce stronger downward band bending. Figure 16(j)–(k) show that the VFET could represent a strong direction selection as a Schottky diode.[243] The reverse current was increased after applying higher gate pulses, while the forward current nearly stayed at the same level. The retention of this device could stabilize and

be extrapolated to 10 years. The superior performance was ascribed to the high level of ferroelectricity of the HZO films. Recently, mica has been found as a promising substrate for the fabrication of the inorganic flexible FeFETs due to its flexibility and high temperature resistance.[244] The ferroelectricity of FE-HfO_2 on flexible mica substrates was also investigated, which showed no degradation even under a large bending radius.[245] However, studies ont flexible HfO_2-based FeFETs are limited to date, and further studies are required, especially with attention to the bending radius and bending cycles.

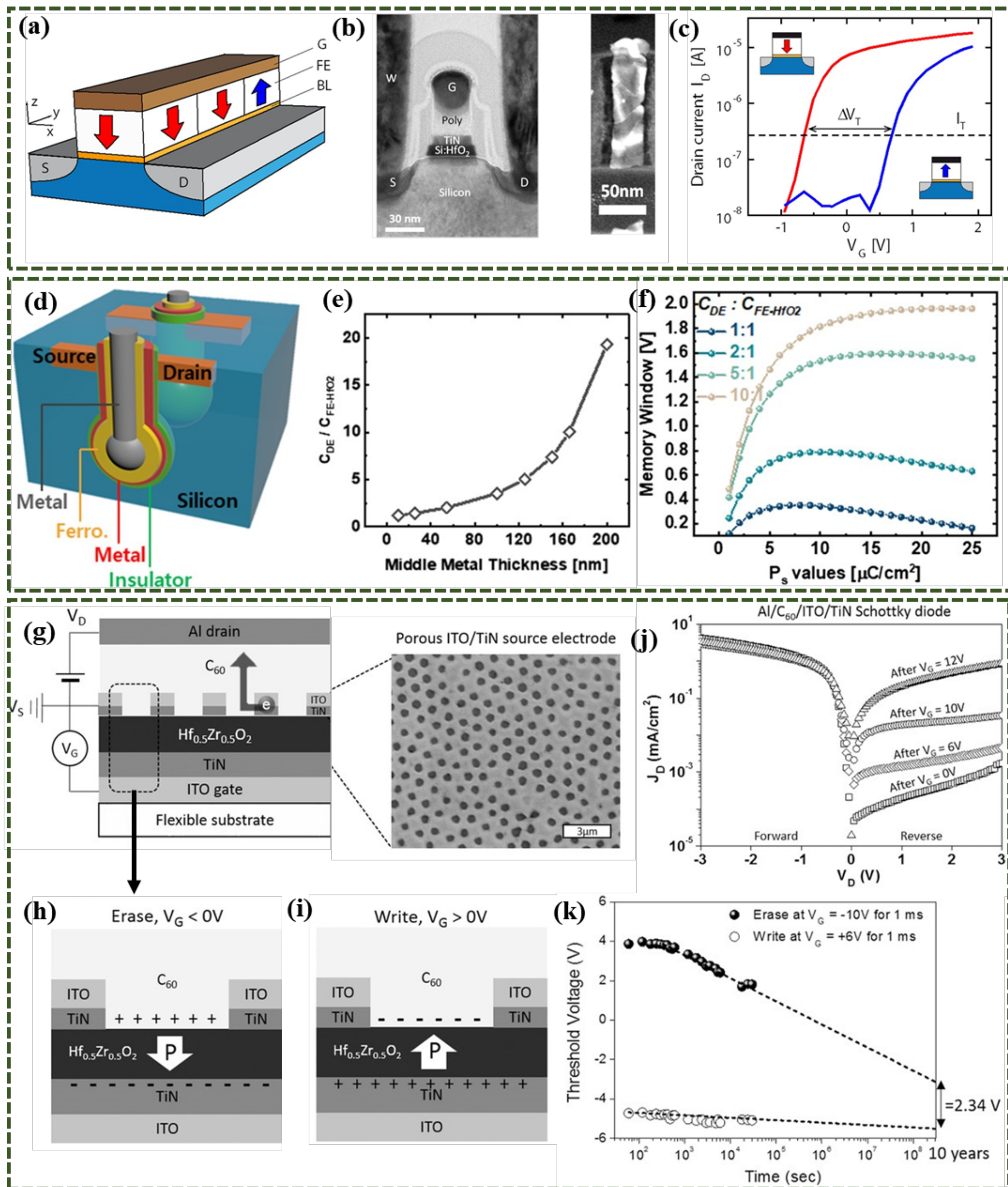

FIG. 16. (a) Structure of FeFET, (b) TEM image of cross section, (c) I_D–V_G transfer curves with different polarization directions.[208] (d) Schematic structure of MFMIS-FeFET, (e) dependence of middle metal layer on the $C_{DE}/C_{Fe\text{-}HfO2}$, (f) Memory Window (MW) variation with P_s values under different $C_{DE}/C_{Fe\text{-}HfO2}$.[234] (g) Device schematic of flexible VFET and SEM image of porous ITO/TiN source electrode, polarization direction at the interfacial region after (h) positive gate voltage and (i) negative gate

voltage, (j) J_D-V_D curves and (k) retention properties of this VFET.[243] Reproduced with permission from (a-c) Mulaosmanovic *et al.*, ACS Appl. Mater. Inter. 9 (4) (2017). [208] Copyright 2017, American Chemistry Society; (d-f) Kim *et al.*, Phys. Status. Solid-R. 15 (5) (2021). [234] Copyright 2021, John Wiley and Sons; (g-k) Yu *et al.*, Adv. Funct. Mater. 27 (21) (2017). [243] Copyright 2017, John Wiley and Sons.

3. *Ferroelectric tunneling junctions (FTJs)*

A ferroelectric tunneling junctions (FTJ) is another two-terminal nonvolatile memory, which can achieve non-destructive write and readout through the direction of ferroelectric polarization and tunneling current across the capacitors. Tian *et al.* firstly discovered the tunneling electro-resistance (TER) effect in HfO_2, and on/off ratio could reach 10000%, which comparable to ReRAM.[246] In 2016, a 2.5 nm-thick HZO was fabricated on a silicon substrate, which was highly suitable for FTJ applications. [247] As shown in Fig. 17(a)-(c), Ambriz-Vargas *et al.* fabricated a TiN/HZO/Pt FTJ with a TER of 15 at a low read voltage of 0.2 V.[248] The good linear fitting of theoretical and experimental I-V curves confirmed the contribution of the TER effect, rather than resistive switching to the resistance change. The electrostatic potential could be modulated by polarization reversal, as displayed in the potential barrier mechanism diagram in Fig. 17(a). The conduction band could become downward and upward according to the direction of polarization vector. The same group achieved a TER ratio over 20 in a symmetric Pt/HZO/Pt stack, which was related to the different interfacial conditions near top and bottom electrodes. [249] During polarization switching, the electric charges could move towards one of the interfaces, which would create an

insulating region and a different resistance state. Seo *et al.* calculated the effect of atomic species at the interfaces on the tunneling barrier in ferroelectric HfO_2-based FTJs using DFT simulations.[250] The barrier height can be adjusted by varying the interface configuration. Kabuyanagi *et al.* [251] optimized the retention and TER performance of HfO_2-based FTJ by adopting a template layer. The decrease of crystallization temperature can efficiently reduce the thickness of interface layer, which finally decreases the depolarization field and improves data retention.[252]

Park *et al*. reported on the two-step polarization switching in $Hf_{0.4}Zr_{0.6}O_2$ thin films through electric field cycling, where an intermediate nonpolar phase appeared as the transition phase.[253] The UP → nonpolar and nonpolar → DOWN steps from pulse switching measurement could be clearly observed, which originated from the redistribution of oxygen vacancies. The discovery of this stable mediate polarization state can broaden its practical application in hardware networks.[254-256] Lee *et al*. also reported on the stable sub-loop behavior in Si: HfO_2 films through conventional voltage measurements, combining Monte Carlo simulations and first principle calculations.[257] Different polarization states could be achieved by applying different voltage amplitudes. Due to the small thickness of HfO_2 and its low activation energy, the stability for immediate states and the small grain size for nucleation could ensure the multi-levered robust polarization states. A 3D vertical FTJ array was successfully fabricated by Chen's group, where the 3D schematic and the zoomed-in schematic of the single unit are shown in Fig. 17(d)-(f).[258] When the device was continuously stimulated by an applied voltage, the conductance of the HZO film became increasingly larger. Therefore,

the memory is formed and external data can be remembered and recognized. The fault could be distinguished for data readout could be largely decreased after multiple pseudo training pulses. The superior ferroelectricity and scalability make FE-HfO_2 attractive for the further non-volatile memories, and further physical mechanisms for improving the device performance and reliability is needed.

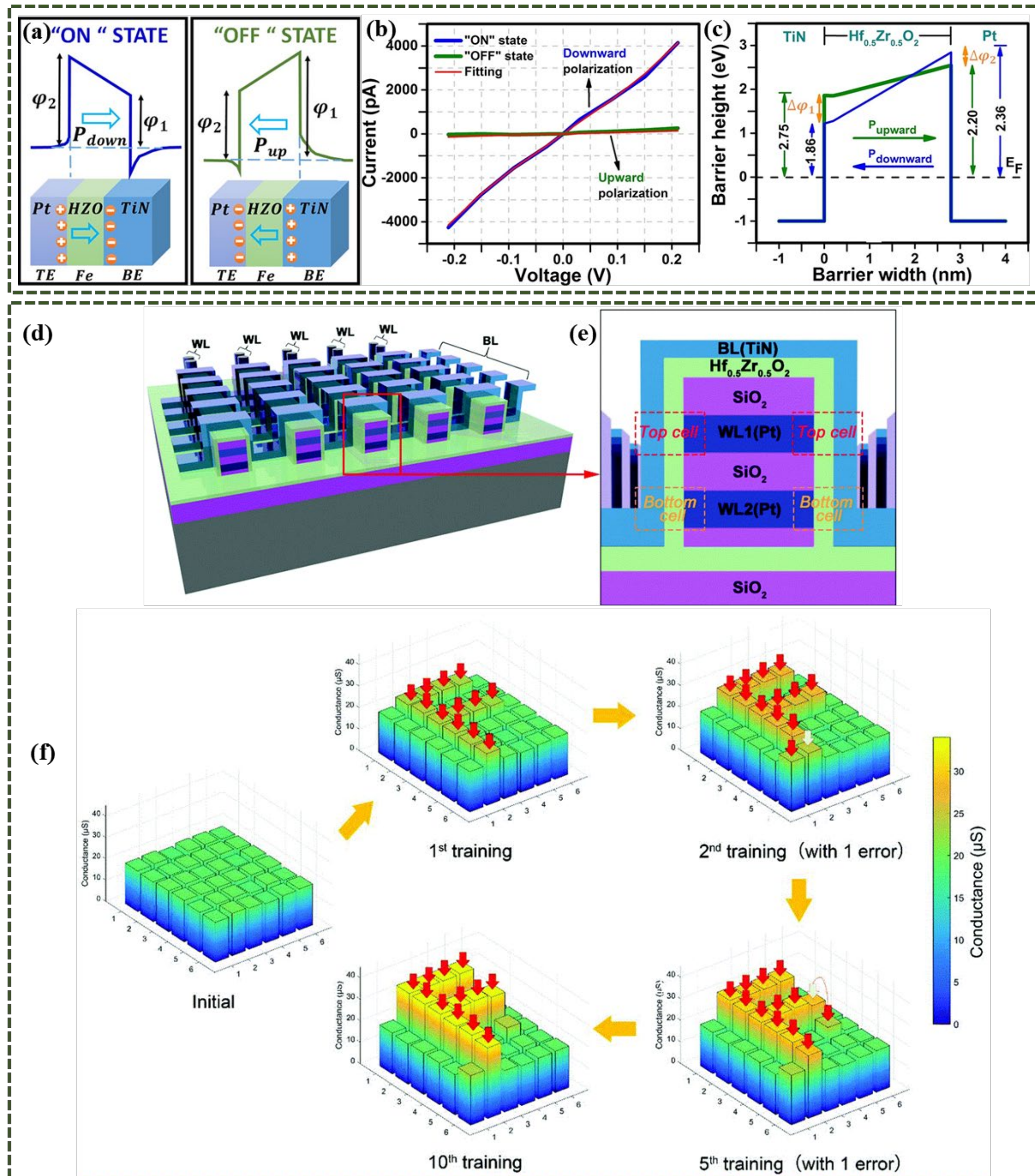

FIG. 17. (a) FTJ device under "ON" and "OFF" state, (b) I-V curves of TiN/HZO/Pt heterostructure and (c) electrostatic potential barrier height with polarization

directions.[248] Schematic structures of (d) 3D vertical HZO FTJ array and (e) single FTJ unit cell, (f) training application.[258] Reproduced with permission from (a-c) Ambriz-Vargas et al., ACS Appl. Mater. Inter. 9 (15), 13262 (2017). [248] Copyright 2017, American Chemistry Society. (d-f) Chen et al., Nanoscale 10 (33), 15826 (2018). [258] Copyright 2018, Royal of Society Chemistry.

B. Bioelectronic synapses for neuromorphic applications

Neuromorphic computing attracts significant interest for emulating the brain of a human and can fulfill the rapid development of big data and the Internet of Things, which can solve the complex computer algorithm through distributed parallel information processing. On account of its adjustable ferroelectricity, it is appropriate to design a brain-like nervous system which can respond to external stimulation, such as electric stimulation, illumination, mechanical stress, environmental sound, and external smells. The study of bioelectric synaptic devices using ferroelectric HfO_2 for neuromorphic applications is therefore necessary.

Numerous synapses connect the neurons together, and the impression and depression of synaptic transition can be achieved by the influx and extrusion of Ca^+,[259] as shown in Fig. 18(a) and Fig. 18(b). Kim *et al.* demonstrated a photonic synapse device, which was demonstrated using photonic semiconductors of indium gallium zinc oxide (IGZO) in combination with ferroelectric HZO films.[259] The conductance of the IGZO channel was able to increase with the optical stimulation and decayed over time, without light illumination. Upon applying a ferroelectric HZO film, the conductance could be easily adjusted through applying different voltage amplitudes due to the

different polarization states. Figure 18(c) displays the modulation of a synaptic weight through controlling the downward and upward polarization states of HZO. The accumulation and depletion of charge carriers on the IGZO/HZO interface can cause the recombination of photo-generated electrons, and lead to the different relaxation behaviors on the synapse. Jeon *et al.* reported on hysteresis modulation by passivating the charge traps at the HZO/MoS_2 interface for application in optic neural networks, [260] as shown in Fig. 18(d)-(f). A color recognition capability could be imitated due to the absorption of visible light by a MoS_2 channel, similar to a human vision system. The conductance could be modulated by the HZO ferroelectric films and the interface trap-dependent clockwise hysteresis could be transformed into a polarization-related hysteresis. The large accuracy (90.1%) of the artificial neural network (ANN), compared to that of ideal synaptic device (94.5%), indicated the high potential for pattern-recognition applications.

In addition to regulating the concentration of charge carriers through the polarization of ferroelectric HfO_2-based films, the ferroelectric FET can also be directly used as analog synapses for speech and image recognition. Jerry *et al.* realized the modulation of threshold voltage in a FeFET using the partial polarization switching of HZO films, which resulted in multiple conductance states.[261] The potentiation and depression can be successfully achieved with high accuracy (90%) after training. Kim *et al.* reported on ferroelectric thin-film transistors (FeTFT) as synaptic devices with a 91.1% recognition accuracy, as shown in Fig. 18(g)-(i).[262] Figure 18(g) shows a schematic structure of FeTFT with the combination of a IGZO oxide semiconductor

and a $HfZrO_x$ ferroelectric film. The multilevel data storage is represented by the different current conditions through applying different programming voltage pulses, as shown in Fig. 18(h). The corresponding conductive mechanisms are shown in Fig. 18(i). In the pristine state, the polarization points downward when a negative bias pulse is applied on $HfZrO_x$ film. The IGZO semiconductor is under a low conductance state because of the depletion of electrons from the interface between IGZO and $HfZrO_x$ film. With the application of positive voltages, the electrons can accumulate at the interface due to the polarization direction towards upward and the IGZO semiconductor will change to a high conductance state. The concentration of electrons can increase with the amplitude of applied voltage pulses, which can trigger the programming state. The direction and intensity of polarization can influence the quantities of electrons at the interface, which results in different data storage. Chou *et al.* improved the ferroelectric performance of $HfZrO_x$ film using a poly-GeSn channel and inducing a Ta_2O_5 dielectric layer, and obtained FeTFTs with high reliability over 10 years.[263] The defects at the interface can be largely decreased by NH_3 plasma treatment and the introduction of higher-*k* dielectric layer, which can promise the high quality of interface and promote the stronger endurance of films. Meanwhile, the spike-timing-dependent plasticity (STDP) rules are successfully imitated by such monolithic 3D IC.

Interestingly, Mulaosmanovic *et al.* constructed a neural network according to two important neuronal dynamics including integration and firing based on HfO_2-based FeFETs,[264] as shown in Fig. 18(j)-(n). The neural network consisted of a crossbar synaptic array fabricated by nanoscale Si: HfO_2, which can significantly reduce the

power and silicon area consumption. The OFF state was not be affected by limited sub-threshold pulses due to insufficient switching of nano-domains. However, the program transition could suddenly occur due to polarization reversal after the nucleation of numerous nano-domains. The electronic neurons could execute a firing action after receiving necessary pulses through ferroelectric HfO_2-based FeFETs.[265] Recently, Zeng *et al*. reported on the multi-level operation in FE-HfO_2 FeFET from the point of domain size in combination with the phase field simulation of domain switching.[266] The multi-level synapse could be produced by effectively controlling the multi-step domain switching. The STDP rules were also verified using such HfO_2-based memristors. [267-271]

In addition to the previously mentioned applications of ferroelectric HfO_2-based films, piezoelectric devices, resistive devices are also being developed. An artificial olfactory system has been achieved through designing Sr: ZnO-based gas sensors, HfO_x-based resistive memristors, and PVDF-based electro-mechanical actuators.[271] The integration and interaction of ferroelectric memristors with other gas sensors, stress sensors, and sound sensors can lead to the building of a multisensory, memory, and actuator neural network, which will clearly recognize and response to external stimulation. Schenk *et al*. firstly reported the piezoelectric performance of 5% La: HfO_2 films by CSD method within the thickness range of 45 nm ~ 1 μm.[107] An improved P_r of 9 $\mu C/cm^2$ can be achieved and the estimated d_{33} is 7.7 pm/V for the 1 μm-thick La: HfO_2 films after 460 cycles. Recently, the in-plane piezo-response was identified in Si-doped HfO_2 films and the d_{31} value of ~ 11.5 pm/V larger than AlN was obtained. The

piezoelectric properties of HfO_2 can pave a way toward actuation and sensing fields.

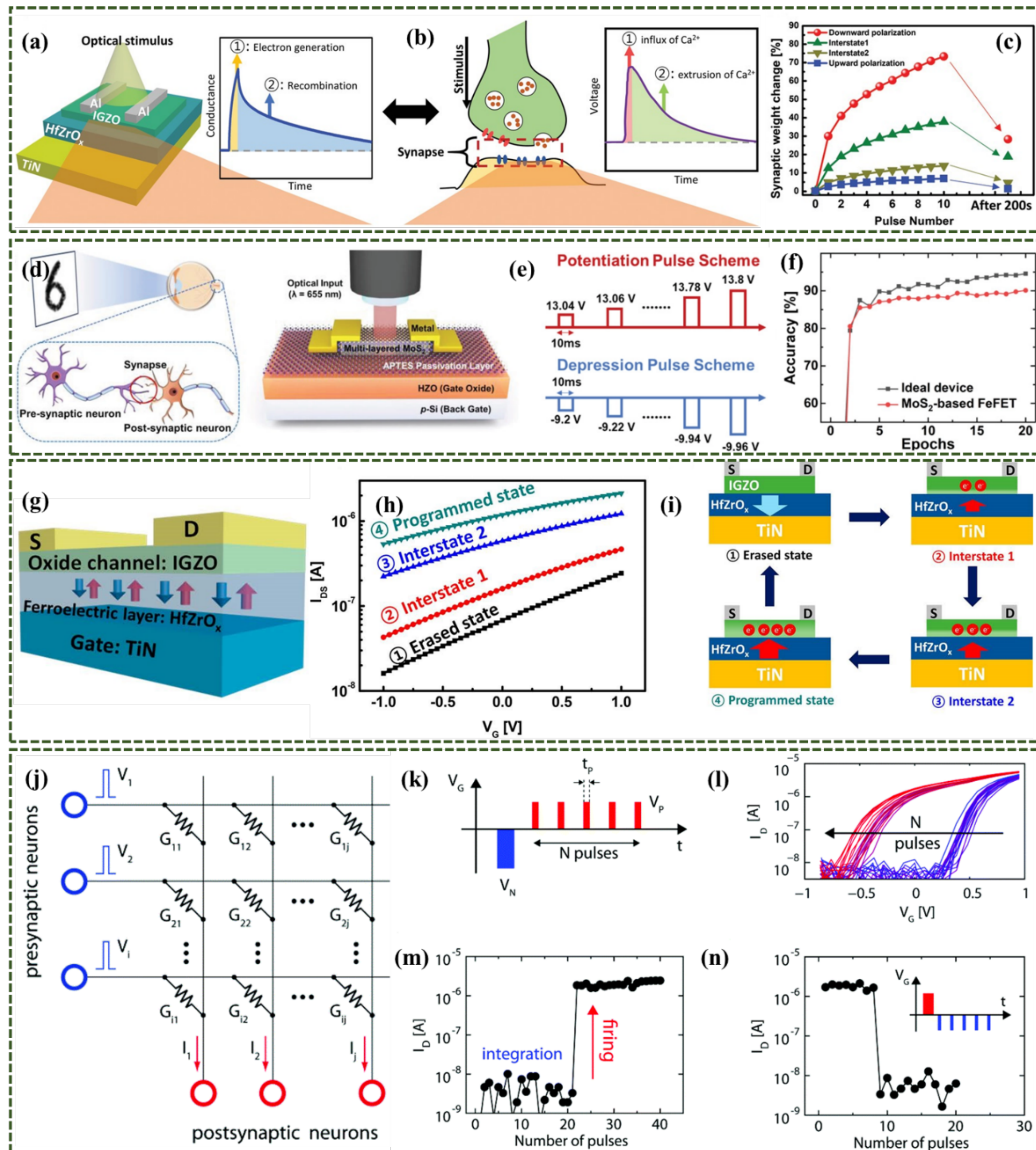

FIG. 18. (a) Schematic of photonic synapse device, (b) illustration of action response to stimulation, (c) synaptic weight changes with response to different ferroelectric states.[259] (d) Schematic of optic-neural synapse device based on MoS_2-based FeFET with a HZO ferroelectric layer, (e) applied pulses on the gate electrode for potentiation and depression, (f) comparison of simulated pattern with ideal devices as a function of epochs.[260] (g) Schematic of $HfZrO_x$ FeTFT, (h) multiple conductance states of FeTFT

and (i) illustrations of conductive mechanisms for data storage.[262] (j) Diagram of neural network consisting of synaptic arrays, (k) pulsing scheme using identical gate pulses, (l) I_D-V_G curves with the increase of pulse numbers, (m) from OFF to ON state, (n) from ON to OFF state with negative stimulation.[264] Reproduced with permission from (a-c) Kim et al., Adv. Mater. 32 (12), 1907826.1 (2020). [259] Copyright 2020, John Wiley and Sons; (d-f) Jeon et al., Small 16 (49) (2020).[260] Copyright 2020, John Wiley and Sons; (g-i) Kim et al., Nano Lett. 19(3), 2044 (2019).[262] Copy right 2019, American Chemistry Society. (j-n) Mulaosmanovic et al., Nanoscale 10 (46), 21755 (2018). [264] Copyright 2018, Royal of Society Chemistry.

VI. SUMMARY AND PERSPECTIVE

This paper comprehensively reviews current developments on HfO_2-based films due to its excellent ferroelectric properties at ultrathin thickness, CMOS compatibility and mature fabrication technique. The crystal structure and phase transition kinetics are complex due to their small variation in free energy and in order to explain the origin of ferroelectricity and induce a stronger polarization, detailed strategies are summarized and classified, including the use of doping elements, the development of a mechanical stress and surface energy effects. Stronger ferroelectricity represents better storage capacity, while the achieved experimental P_r value is far smaller than the theoretical value (54 μC/cm^2). The performance can be further improved through fabrication of single-crystal HfO_2-based films, and the use of epitaxial films with a preferred orientation. In addition, the bulk ferroelectricity in HfO_2 remains an unsolved mystery which need to be examined in detail.

For HfO_2-based thin films, the *wake-up effect*, *fatigue* and *imprint* issues are main challenges for practical application, which are yet to be fully solved. Oxygen vacancies at the interfacial region are thought to be the influencing factors, which lead to a decrease in the endurance of devices. As a result, it is feasible to control the concentration of oxygen vacancies through adopting oxide electrodes, controlling the process conditions with appropriate oxygen exposure, and optimizing the interface structure.

HfO_2-based ferroelectrics have widespread applications due to their non-volatile characteristics such as FRAM, FeFET, FTJ and neural networks, while there is a need to solve endurance issues. In addition, other interdisciplinary approaches can be developed exploiting the ferroelectricity of HfO_2-based devices including vision, touch and hearing, and further developments of 3D devices with high density are demanded to achieve imitation of a human brain with autonomous learning and memory.

ACKNOWLEDGEMENTS

Thanks to the financial support by the National Natural Science Foundation of China (No. U19A2087 and 52002404), the Construction of Innovative Provinces in Hunan Province of China (No. 2020GK2062), the State Key Laboratory of Powder Metallurgy, Central South University, Changsha, China. Xuefan Zhou (Postdoc) acknowledges the support from the China National Postdoctoral Program for Innovative Talents (Grant No. BX2021377).

DATA AVAILABILITY

Data sharing is not applicable to this article as no new data were created or analyzed in this study.

REFERENCES

[1] J. F. Scott and C. A. Paz de Araujo, Science **246** (4936), 1400 (1989).

[2] J. Valasek, Phys. Rev. **17** (4), 475 (1921).

[3] D. Vanderbilt, Mater. Res. Bull. (2002).

[4] B. Jaffe, R. S. Roth, and S. Marzullo, J. Appl. Phys. **25** (6), 809 (1954).

[5] Martin and M. Richard, Phys. Rev. B **5** (4), 1607 (1972).

[6] S. Aggarwal, A. M. Dhote, H. Li, S. Ankem, and R. Ramesh, Appl. Phys. Lett. **74** (2), 230 (1999).

[7] J. R. Slack and J. C. Burfoot, Thin Solid Films **6** (4), 233 (1970).

[8] H. P. McAdams, R. Acklin, T. Blake, X. H. Du, J. Eliason, J. Fong, W. F. Kraus, D. Liu, S. Madan, T. Moise, S. Natarajan, N. Qian, Y. C. Qiu, K. A. Remack, J. Rodriguez, J. Roscher, A. Seshadri, and S. R. Summerfelt, IEEE J. Solid-st. Circ. **39** (4), 667 (2004).

[9] W. J. Lee, C. H. Shin, C. R. Cho, J. S. Lyu, B. W. Kim, B. G. Yu, and K. I. Cho, Jpn. J. Appl. Phys. **38** (4A), 2039 (1999).

[10] T. S. Böscke, J. Müller, D. Bräuhaus, U. Schröder, and U. Böttger, Appl. Phys. Lett. **99** (10), 102903 (2011).

[11] S. Oh, H. Hwang, and I. K. Yoo, APL Mater. **7** (9), 091109 (2019).

[12] M. Takahashi and S. Sakai, Jpn. J. Appl. Phys. **44** (24-27), L800 (2005).

[13] N. Setter, D. Damjanovic, L. Eng, G. Fox, S. Gevorgian, S. Hong, A. Kingon, H. Kohlstedt, N. Y. Park, and G. B. Stephenson, J. Appl. Phys. **100** (5), p.051606.1 (2006).

[14] S. H. Choi, H. Y. Ko, J. E. Heo, Y. H. Son, B. J. Bae, D. C. Yoo, D. H. Im, Y. J. Jung, K. R. Byun, J. H. Hahm, S. H. Shin, B. U. Yoon, C. K. Hong, H. K. Cho, and J. T. Moon, Integr. Ferroelectr. **84**, 147 (2006).

[15] M. H. Park, Y. H. Lee, H. J. Kim, Y. J. Kim, T. Moon, K. D. Kim, J. Muller, A. Kersch, U. Schroeder, T. Mikolajick, and C. S. Hwang, Adv. Mater. **27** (11), 1811 (2015).

[16] J. Müller, P. Polakowski, S. Mueller, and T. Mikolajick, ECS J. Solid State SC. **4** (5), N30 (2015).

[17] J. Robertson and B. Falabretti, J. Appl. Phys. **100** (1), 5243 (2006).

[18] D. Fischer and A. Kersch, Appl. Phys. Lett. **92** (1), 5243 (2008).

[19] R. J., Eur. Phys. J-Appl, Phys. **28** (3), 265 (2004).

[20] S. J. Kim, J. Mohan, H. S. Kim, S. M. Hwang, N. Kim, Y. C. Jung, A. Sahota, K. Kim, H.-Y. Yu, P.-R. Cha, C. D. Young, R. Choi, J. Ahn, and J. Kim, Materials **13** (13) (2020).

[21] H. P. Min, H. J. Kim, J. K. Yu, T. Moon, and C. S. Hwang, Appl. Phys. Lett. **104** (7), 072901 (2014).

[22] P. Polakowski and J. Müller, Appl. Phys. Lett. **106** (23) (2015).

[23] S. Starschich, D. Griesche, T. Schneller, R. Waser, and U. Böttger, Appl. Phys. Lett. **104** (20) (2014).

[24] T. Shimizu, K. Katayama, T. Kiguchi, A. Akama, T. J. Konno, and H. Funakubo, Appl. Phys. Lett. **107** (3) (2015).

[25] T. Shimizu, K. Katayama, T. Kiguchi, A. Akama, T. J. Konno, O. Sakata, and H. Funakubo, Sci. Rep. **6**, 32931 (2016).

[26] U. Schroeder, E. Yurchuk, J. Mueller, D. Martin, T. Schenk, P. Polakowski, C. Adelmann, M. I. Popovici, S. V. Kalinin, and T. Mikolajick, Jpn. J. Appl. Phys. **53** (8S1), 08LE02.1 (2014).

[27] J. Muller, T. S. Boscke, U. Schroder, S. Mueller, D. Brauhaus, U. Bottger, L. Frey, and T. Mikolajick, Nano Lett. **12** (8), 4318 (2012).

[28] S. Mueller, J. Mueller, A. Singh, S. Riedel, J. Sundqvist, U. Schroeder, and T. Mikolajick, Adv. Funct. Mater. **22** (11), 2412 (2012).

[29] M. H. Park, H. J. Kim, Y. J. Kim, T. Moon, K. D. Kim, and C. S. Hwang, Nano Energy **12**, 131 (2015).

[30] M. H. Park, H. J. Kim, Y. J. Kim, T. Moon, K. D. Kim, and C. S. Hwang, Adv. Energy Mater. **4** (16) (2014).

[31] T. Mimura, T. Shimizu, and H. Funakubo, Appl. Phys. Lett. **115** (3) (2019).

[32] S. Kirbach, M. Lederer, S. Esslinger, C. Mart, M. Czernohorsky, W. Weinreich, and T. Wallmersperger, Appl. Phys. Lett. **118** (1) (2021).

[33] X. H. Xu, F. T. Huang, Y. Qi, S. Singh, K. M. Rabe, D. Obeysekera, J. Yang, M. W. Chu, and S. W. Cheong, Nat. Mater. **20** (6), 826 (2021).

[34] M. H. Park, Y. H. Lee, T. Mikolajick, U. Schroeder, and C. S. Hwang, MRS Commun. **8** (03), 795 (2018).

[35] T. Mikolajick, S. Slesazeck, M. H. Park, and U. Schroeder, MRS Bull. **43** (5), 340 (2018).

[36] J. Y. Park, K. Yang, D. H. Lee, S. H. Kim, Y. Lee, P. R. S. Reddy, J. L. Jones, and M. H. Park, J. Appl. Phys. **128** (24) (2020).

[37] M. Pešić, C. Künneth, M. Hoffmann, H. Mulaosmanovic, S. Müller, E. T. Breyer, U. Schroeder, A. Kersch, T. Mikolajick, and S. Slesazeck, J. Comput. Electron. **16** (4), 1236 (2017).

[38] M. H. Park and C. S. Hwang, Rep. Prog. Phys. **82** (12), 124502 (2019).

[39] M. H. Park, D. H. Lee, K. Yang, J. Y. Park, G. T. Yu, H. W. Park, M. Materano, T. Mittmann, P. D. Lomenzo, T. Mikolajick, U. Schroeder, and C. S. Hwang, J. Mater. Chem. C **8** (31), 10526 (2020).

[40] D. H. Lee, Y. Lee, K. Yang, J. Y. Park, S. H. Kim, P. R. S. Reddy, M. Materano, H. Mulaosmanovic, T. Mikolajick, J. L. Jones, U. Schroeder, and M. H. Park, Appl. Phys. Rev, **8** (2) (2021).

[41] C. E. Curtis, L. M. Doney, and J. R. Johnson, J. Am. Ceram. Soc. **37** (10), 458 (2006).

[42] W. Newkirk, Acta Crystallogr. **18**, 983 (1965).

[43] O. Ohtaka, H. Fukui, T. Kunisada, T. Fujisawa, K. Funakoshi, W. Utsumi, T. Irifune, K. Kuroda, and T. Kikegawa, J. Am. Ceram. Soc. **84** (6), 1369 (2001).

[44] E. H. Kisi, C. J. Howard, and R. J. Hill, J. Am. Ceram. Soc. **72** (1989).

[45] C. J. Howard, E. H. Kisi, R. B. Roberts, and R. J. Hill, J. Am. Ceram. Soc. **73** (10), 2828 (1990).

[46] Y. Wei, P. Nukala, M. Salverda, S. Matzen, H. J. Zhao, J. Momand, A. S. Everhardt, G. Agnus, G. R. Blake, P. Lecoeur, B. J. Kooi, J. Iniguez, B. Dkhil, and B. Noheda, Nat. Mater. **17** (12), 1095 (2018).

[47] Y. Zhang, Q. Yang, L. Tao, E. Y. Tsymbal, and V. Alexandrov, Phys. Rev. Appl. **14**, 014068 (2020).

[48] P. Nukala, J. Antoja-Lleonart, Y. Wei, L. Yedra, and B. Noheda, ACS Appl. Electron. Mater. **1** (1), 2585 (2019).

[49] E. H. Kisi and C. J. Howard, Key Eng. Mater. **153-154**, 1 (1998).

[50] E. H. Kisi, J. Am. Ceram. Soc **81** (3), 741 (1998).

[51] J. Müller, U. Schröder, T. S. Böscke, I. Müller, U. Böttger, L. Wilde, J. Sundqvist, M. Lemberger, P. Kücher, T. Mikolajick, and L. Frey, J. Appl. Phys. **110** (11) (2011).

[52] T. D. Huan, V. Sharma, G. A. Rossetti, Jr., and R. Ramprasad, Phys. Rev. B **90** (6) (2014).

[53] S. E. Reyes-Lillo, K. F. Garrity, and K. M. Rabe, Phys. Rev. B **90** (14), 5 (2014).
[54] R. Materlik, C. Kuenneth, and A. Kersch, J. Appl. Phys. **117** (13), 134109 (2015).
[55] J. Adam and R. M. D., Acta Crystallogr. **12** (11), 951 (2010).
[56] X. Sang, E. D. Grimley, T. Schenk, U. Schroeder, and J. M. Lebeau, Appl. Phys. Lett. **106** (16), 114113 (2015).
[57] M. H. Park, Y. H. Lee, H. J. Kim, T. Schenk, W. Lee, K. D. Kim, F. P. G. Fengler, T. Mikolajick, U. Schroeder, and C. S. Hwang, Nanoscale **9** (28), 9973 (2017).
[58] R. Batra, T. D. Huan, J. L. Jones, G. Rossetti, and R. Ramprasad, J. Phys. Chem. C **121** (8), 4139 (2017).
[59] M. H. Park, Y. H. Lee, T. Mikolajick, U. Schroeder, and C. S. Hwang, Adv. Electron. Mater. **5** (3) (2019).
[60] K. D. Kim, M. H. Park, H. J. Kim, Y. J. Kim, T. Moon, Y. H. Lee, S. D. Hyun, T. Gwon, and C. S. Hwang, J. Mater. Chem. C **4** (28), 6864 (2016).
[61] M. H. Park, Y. H. Lee, H. J. Kim, Y. J. Kim, T. Moon, K. D. Kim, S. D. Hyun, T. Mikolajick, U. Schroeder, and C. S. Hwang, Nanoscale **10** (2), 716 (2018).
[62] Y. H. Lee, S. D. Hyun, H. J. Kim, J. S. Kim, C. Yoo, T. Moon, K. D. Kim, H. W. Park, Y. B. Lee, B. S. Kim, J. Roh, M. H. Park, and C. S. Hwang, Adv. Electron. Mater. **5** (2) (2019).
[63] J. Wu, F. Mo, T. Saraya, T. Hiramoto, and M. Kobayashi, Appl. Phys. Lett. **117** (25) (2020).
[64] Y. Tashiro, T. Shimizu, T. Mimura, and H. Funakubo, ACS Appl. Electron. Mater. (2021).
[65] M. H. Park, C. C. Chung, T. Schenk, C. Richter, K. Opsomer, C. Detavernier, C. Adelmann, J. L. Jones, T. Mikolajick, and U. Schroeder, Adv. Electron. Mater. **4** (7), 1800091 (2018).
[66] T. Shimizu, Y. Tashiro, T. Mimura, T. Kiguchi, T. Shiraishi, T. J. Konnno, O. Sakata, and H. Funakubo, Phys. Status. Solid-R. **15** (5) (2021).
[67] S. Clima, D. J. Wouters, C. Adelmann, T. Schenk, U. Schroeder, M. Jurczak, and G. Pourtois, Appl. Phys. Lett. **104** (9) (2014).
[68] M. H. Park, Y. H. Lee, H. J. Kim, Y. J. Kim, T. Moon, K. Do Kim, S. D. Hyun, and C. S. Hwang, ACS Appl. Mater. Inter. **10** (49), 42666 (2018).
[69] D. Das, V. Gaddam, and S. Jeon, IEEE Electr. Dev. L. **41** (1), 34 (2020).
[70] Q. Luo, H. Ma, H. Su, K.-H. Xue, R. Cao, Z. Gao, J. Yu, T. Gong, X. Xu, J. Yin, P. Yuan, L. Tai, D. Dong, S. Long, Q. Liu, X.-S. Miao, H. Lv, and M. Liu, IEEE Electr. Dev. L. **40** (4), 570 (2019).
[71] G. Karbasian, A. Tan, A. Yadav, E. M. H. Sorensen, C. R. Serrao, A. I. Khan, K. Chatterjee, S. Kim, C. Hu, and S. Salahuddin, in *2017 International Symposium on Vlsi Technology, Systems and Application* (2017).
[72] J. C. Slater, J. Chem. Phys. **41** (10), 3199.
[73] E. Yurchuk, J. Mueller, R. Hoffmann, J. Paul, D. Martin, R. Boschke, T. Schloesser, S. Mueller, S. Slesazeck, R. van Bentum, M. Trentzsch, U. Schroeder, and T. Mikolajick, in *2012 4th IEEE International Memory Workshop* (2012).
[74] P. D. Lomenzo, S. Jachalke, H. Stoecker, E. Mehner, C. Richter, T. Mikolajick, and U. Schroeder, Nano Energy **74**, 10 (2020).
[75] D. Martin, J. Mueller, T. Schenk, T. M. Arruda, A. Kumar, E. Strelcov, E. Yurchuk, S. Mueller, D. Pohl, U. Schroeder, S. V. Kalinin, and T. Mikolajick, Adv. Mater. **26** (48), 8198 (2014).
[76] E. Yurchuk, J. Müller, S. Knebel, J. Sundqvist, A. P. Graham, T. Melde, U. Schröder, and T. Mikolajick, Thin Solid Films **533**, 88 (2013).
[77] R. Materlik, C. Künneth, M. Falkowski, T. Mikolajick, and A. Kersch, J. Appl. Phys. **123** (16) (2018).

[78] M. G. Kozodaev, A. G. Chernikova, R. R. Khakimov, M. H. Park, A. M. Markeev, and C. S. Hwang, Appl. Phys. Lett. **113** (12) (2018).

[79] M. Hoffmann, U. Schroeder, C. Künneth, A. Kersch, S. Starschich, U. Böttger, and T. Mikolajick, Nano Energy **18**, 154 (2015).

[80] C. Mart, K. Kuehnel, T. Kaempfe, S. Zybell, and W. Weinreich, Appl. Phys. Lett. **114** (10) (2019).

[81] P. Polakowski, S. Riedel, W. Weinreich, M. Rudolf, J. Sundqvist, K. Seidel, and J. Mueller, in *2014 IEEE 6th International Memory Workshop* (2014).

[82] C. K. Lee, E. Cho, H. S. Lee, C. S. Hwang, and S. Han, Phys. Rev. B **78** (1), 5 (2008).

[83] S. Starschich and U. Bottger, J. Appl. Phys. **123** (4), 6 (2018).

[84] M. H. Park, T. Schenk, C. M. Fancher, E. D. Grimley, C. Zhou, C. Richter, J. M. LeBeau, J. L. Jones, T. Mikolajick, and U. Schroeder, J. Mater. Chem. C **5** (19), 4677 (2017).

[85] J. D. Luo, Y. T. Yeh, Y. Y. Lai, C. F. Wu, H. T. Chung, Y. S. Li, K. C. Chuang, W. S. Li, P. G. Chen, M. H. Lee, and H. C. Cheng, Vacuum **176** (2020).

[86] H. P. Min, J. K. Han, J. K. Yu, W. Lee, H. K. Kim, and C. S. Hwang, Appl. Phys. Lett. **102** (11) (2013).

[87] D. Y. Cho, H. S. Jung, I. H. Yu, J. H. Yoon, H. K. Kim, S. Y. Lee, S. H. Jeon, S. Han, J. H. Kim, T. J. Park, B. G. Park, and C. S. Hwang, Chem. Mater. **24** (18), 3534 (2012).

[88] C. Kuenneth, R. Materlik, M. Falkowski, and A. Kersch, ACS Appl. Nano Mater. **1** (1), 254 (2018).

[89] A. K. K., H. Miki, K. Torii, and Y. Fujisaki, Appl. Phys. Lett. (1996).

[90] M. H. Park, H. J. Kim, Y. J. Kim, T. Moon, K. D. Kim, Y. H. Lee, S. D. Hyun, and C. S. Hwang, J. Mater. Chem. C **3** (24), 6291 (2015).

[91] S. Oh, J. Song, I. K. Yoo, and H. Hwang, IEEE Electr. Dev. L. **40** (7), 1092 (2019).

[92] Y. Zhou, Y. K. Zhang, Q. Yang, J. Jiang, P. Fan, M. Liao, and Y. C. Zhou, Comp. Mater. Sci. **167**, 143 (2019).

[93] S. Clima, S. Mcmitchell, K. Florent, L. Nyns, and G. Pourtois, presented at the 2018 IEEE International Electron Devices Meeting (IEDM), San Francisco, CA, USA, 2018.

[94] L. Xu, T. Nishimura, S. Shibayama, T. Yajima, S. Migita, and A. Toriumi, Appl. Phys. Express **9** (9) (2016).

[95] T. Schenk, S. Mueller, U. Schroeder, R. Materlik, A. Kersch, M. Popovici, C. Adelmann, S. Van Elshocht, and T. Mikolajick, in *2013 Proceedings of the European Solid-State Device Research Conference* (IEEE, New York, 2013), pp. 260.

[96] L. Tang, C. Chen, A. Q. Wei, K. Li, D. Zhang, and K. C. Zhou, Ceram. Int. **45** (3), 3140 (2019).

[97] Y. Yao, D. Zhou, S. Li, J. Wang, N. Sun, F. Liu, and X. Zhao, J. Appl. Phys. **126** (15) (2019).

[98] S. Mueller, C. Adelmann, A. Singh, S. Van Elshocht, U. Schroeder, and T. Mikolajick, ECS J. Solid State SC. **1** (6), N123 (2012).

[99] U. Schroeder, S. Mueller, J. Mueller, E. Yurchuk, D. Martin, C. Adelmann, T. Schloesser, R. van Bentum, and T. Mikolajick, ECS J. Solid State SC. **2** (4), N69 (2013).

[100] T. C. U. Tromm, J. Zhang, J. Schubert, M. Luysberg, W. Zander, Q. Han, P. Meuffels, D. Meertens, S. Glass, P. Bernardy, and S. Mantl, Appl. Phys. Lett. **111** (14) (2017).

[101] P. D. Lomenzo, Q. Takmeel, C. Zhou, C. C. Chung, S. Moghaddam, J. L. Jones, and T. Nishida, Appl. Phys. Lett. **107** (24) (2015).

[102] A. G. Chernikova, D. S. Kuzmichev, D. V. Negrov, M. G. Kozodaev, S. N. Polyakov, and A. M. Markeev, Appl. Phys. Lett. **108** (24), 102903 (2016).

[103] H. Liu, S. Zheng, Q. Chen, B. Zeng, J. Jiang, Q. Peng, M. Liao, and Y. Zhou, J Mater. Sci-Mater. El. **30** (6), 5771 (2019).

[104] T. Shiraishi, S. Choi, T. Kiguchi, T. Shimizu, H. Funakubo, and T. J. Konno, Appl. Phys. Lett. **114** (23) (2019).

[105] S. Starschich and U. Boettger, J. Mater. Chem. C **5** (2), 333 (2017).

[106] H. Chen, Y. Chen, L. Tang, H. Luo, K. Zhou, X. Yuan, and D. Zhang, J. Mater. Chem. C **8** (8), 2820 (2020).

[107] T. Schenk, N. Godard, A. Mahjoub, S. Girod, A. Matavz, V. Bobnar, E. Defay, and S. Glinsek, Phys. Status. Solid-R. **14** (3) (2020).

[108] T. Olsen, U. Schröder, S. Müller, A. Krause, D. Martin, A. Singh, J. Müller, M. Geidel, and T. Mikolajick, Appl. Phys. Lett. **101** (8) (2012).

[109] Q. Luo, H. Ma, H. Su, K. H. Xue, and M. Liu, IEEE Electr. Dev. L. **40** (99), 1 (2019).

[110] T. Mittmann, M. Materano, P. D. Lomenzo, M. H. Park, I. Stolichnov, M. Cavalieri, C. Z. Zhou, C. C. Chung, J. L. Jones, T. Szyjka, M. Muller, A. Kersch, T. Mikolajick, and U. Schroeder, Adv. Mater. Interfaces **6** (11), 9 (2019).

[111] T. Shiraishi, S. Choi, T. Kiguchi, T. Shimizu, H. Uchida, H. Funakubo, and T. J. Konno, Jpn. J. Appl. Phys. **57** (11S), 11UF02.1 (2018).

[112] S. Estandia, N. Dix, M. F. Chisholm, I. Fina, and F. Sanchez, Cryst. Growth Des. **20** (6), 3801 (2020).

[113] T. Li, J. Dong, N. Zhang, Z. Wen, Z. Sun, Y. Hai, K. Wang, H. Liu, N. Tamura, S. Mi, S. Cheng, C. Ma, Y. He, L. Li, S. Ke, H. Huang, and Y. Cao, Acta Mater. **207** (2021).

[114] J. Wang, H. P. Li, and R. Stevens, J. Mater. Sci. **27** (20), 5397 (1992).

[115] P. D. Lomenzo, P. Zhao, Q. Takmeel, S. Moghaddam, T. Nishida, M. Nelson, C. M. Fancher, E. D. Grimley, X. Sang, J. M. LeBeau, and J. L. Jones, J Vac. Sci. Technol. B **32** (3), 03d123 (2014).

[116] S. J. Kim, D. Narayan, J. G. Lee, J. Mohan, J. S. Lee, J. Lee, H. S. Kim, Y. C. Byun, A. T. Lucero, C. D. Young, S. R. Summerfelt, T. San, L. Colombo, and J. Kim, Appl. Phys. Lett. **111** (24) (2017).

[117] U. Schroeder, C. Richter, M. H. Park, T. Schenk, M. Pesic, M. Hoffmann, F. P. G. Fengler, D. Pohl, B. Rellinghaus, C. Zhou, C. C. Chung, J. L. Jones, and T. Mikolajick, Inorg. Chem. **57** (5), 2752 (2018).

[118] P. D. Lomenzo, Q. Takmeel, C. Zhou, C. M. Fancher, E. Lambers, N. G. Rudawski, J. L. Jones, S. Moghaddam, and T. Nishida, J. Appl. Phys. **117** (13) (2015).

[119] G. Karbasian, R. dos Reis, A. K. Yadav, A. J. Tan, C. M. Hu, and S. Salahuddin, Appl. Phys. Lett. **111** (2), 4 (2017).

[120] Y. Lee, Y. Goh, J. Hwang, D. Das, and S. Jeon, IEEE T. Electron. Dev. **68** (2), 523 (2021).

[121] R. R. Cao, Y. Wang, S. J. Zhao, Y. Yang, X. L. Zhao, W. Wang, X. M. Zhang, H. B. Lv, Q. Liu, and M. Liu, IEEE Electr. Dev. L. **39** (8), 1207 (2018).

[122] T. Nishimura, L. Xu, S. Shibayama, T. Yajima, S. Migita, and A. Toriumi, Jpn. J. Appl. Phys. **55** (8S2), 08pb01 (2016).

[123] M. H. Park, H. J. Kim, Y. J. Kim, W. Lee, T. Moon, K. D. Kim, and C. S. Hwang, Appl. Phys. Lett. **105** (7), 072902 (2014).

[124] A. G. Chernikova, M. G. Kozodaev, R. R. Khakimov, S. N. Polyakov, and A. M. Markeev, Appl. Phys. Lett. **117** (19), 6 (2020).

[125] Y. Zhang, Z. Fan, D. Wang, J. L. Wang, Z. M. Zou, Y. S. Li, Q. Li, R. Q. Tao, D. Y. Chen, M. Zeng, X. S. Gao, J. Y. Dai, G. F. Zhou, X. B. Lu, and J. M. Liu, ACS Appl. Mater. Inter. **12** (36), 40510 (2020).

[126] Y. Goh, S. H. Cho, S. H. K. Park, and S. Jeon, Nanoscale **12** (16), 9024 (2020).

[127] Z. M. Zhang, S. L. Hsu, V. A. Stoica, H. Paik, E. Parsonnet, A. Qualls, J. J. Wang, L. Xie, M. Kumari, S. Das, Z. N. Leng, M. McBriarty, R. Proksch, A. Gruverman, D. G. Schlom, L. Q. Chen, S. Salahuddin, L. W. Martin, and R. Ramesh, Adv. Mater. **33** (10) (2021).

[128] T. Shiraishi, K. Katayama, T. Yokouchi, T. Shimizu, T. Oikawa, O. Sakata, H. Uchida, Y. Imai, T. Kiguchi, T. J. Konno, and H. Funakubo, Appl. Phys. Lett. **108** (26), 262904 (2016).

[129] T. Li, N. Zhang, Z. Sun, C. Xie, M. Ye, S. Mazumdar, L. Shu, Y. Wang, D. Wang, L. Chen, S. Ke, and H. Huang, J. Mater. Chem. C **6** (34), 9224 (2018).

[130] K. Katayama, T. Shimizu, O. Sakata, T. Shiraishi, S. Nakamura, T. Kiguchi, A. Akama, T. J. Konno, H. Uchida, and H. Funakubo, Appl. Phys. Lett. **109** (11), 112901 (2016).

[131] T. Shimizu, K. Katayama, and H. J. F. Funakubo, Ferroelectrics **512** (1), 105 (2017).

[132] T. Mimura, T. Shimizu, T. Kiguchi, A. Akama, T. J. Konno, Y. Katsuya, O. Sakata, and H. Funakubo, Jpn. J. Appl. Phys. **58** (SB) (2019).

[133] T. Song, R. Bachelet, G. Saint-Girons, R. Solanas, I. Fina, and F. Sanchez, ACS Appl. Electron. Mater. **2** (10), 3221 (2020).

[134] Y. Qi, S. Singh, C. Lau, F.-T. Huang, X. Xu, F. J. Walker, C. H. Ahn, S.-W. Cheong, and K. M. Rabe, Phys. Rev. Lett. **125** (25) (2020).

[135] T. Li, M. Ye, Z. Sun, N. Zhang, W. Zhang, S. Inguva, C. Xie, L. Chen, Y. Wang, S. Ke, and H. Huang, ACS Appl. Mater. Inter. **11** (4), 4139 (2019).

[136] H. Zhou, L. J. Wu, H. Q. Wang, J. C. Zheng, L. H. Zhang, K. Kisslinger, Y. P. Li, Z. Q. Wang, H. Cheng, S. M. Ke, Y. Li, J. Y. Kang, and Y. M. Zhu, Nat. Commun. **8** (2017).

[137] J. Lyu, I. Fina, R. Solanas, J. Fontcuberta, and F. Sanchez, Appl. Phys. Lett. **113** (8) (2018).

[138] J. Lyu, I. Fina, R. Bachelet, G. Saint-Girons, S. Estandía, J. Gázquez, J. Fontcuberta, and F. Sánchez, Appl. Phys. Lett. **114** (22) (2019).

[139] S. S. Cheema, D. Kwon, N. Shanker, R. Dos Reis, S. L. Hsu, J. Xiao, H. Zhang, R. Wagner, A. Datar, M. R. McCarter, C. R. Serrao, A. K. Yadav, G. Karbasian, C. H. Hsu, A. J. Tan, L. C. Wang, V. Thakare, X. Zhang, A. Mehta, E. Karapetrova, R. V. Chopdekar, P. Shafer, E. Arenholz, C. Hu, R. Proksch, R. Ramesh, J. Ciston, and S. Salahuddin, Nature **580** (7804), 478 (2020).

[140] S. Estandia, N. Dix, J. Gazquez, I. Fina, J. Lyu, M. F. Chisholm, J. Fontcuberta, and F. Sanchez, ACS Appl. Electron. Mater. **1** (8), 1449 (2019).

[141] J. Lyu, I. Fina, R. Solanas, J. Fontcuberta, and F. Sánchez, ACS Appl. Electron. Mater. **1** (2), 220 (2019).

[142] J. Lyu, I. Fina, J. Fontcuberta, and F. Sanchez, ACS Appl. Mater. Inter. **11** (6), 6224 (2019).

[143] Y. Yan, D. Zhou, C. Guo, J. Xu, X. Yang, H. Liang, F. Zhou, S. Chu, and X. Liu, J. Sol-gel Sci. Techn. **77** (2), 430 (2015).

[144] M. Hyuk Park, H. Joon Kim, Y. Jin Kim, W. Lee, T. Moon, and C. Seong Hwang, Appl. Phys. Lett. **102** (24), 242905 (2013).

[145] M. Shandalov and P. C. McIntyre, J. Appl. Phys. **106** (8), 5 (2009).

[146] M. W. Pitcher, S. V. Ushakov, A. Navrotsky, B. F. Woodfield, G. S. Li, J. Boerio-Goates, and B. M. Tissue, J. Am. Ceram. Soc. **88** (1), 160 (2005).

[147] J. J. Liao, B. J. Zeng, Q. Sun, Q. Chen, M. Liao, C. G. Qiu, Z. Y. Zhang, and Y. C. Zhou, IEEE Electr. Dev. L. **40** (11), 1868 (2019).

[148] S. Migita, H. Ota, S. Asanuma, Y. Morita, and A. Toriumi, Appl. Phys. Express **14** (5) (2021).

[149] Y. Chen, L. Wang, L. Liu, L. Tang, X. Yuan, H. Chen, K. Zhou, and D. Zhang, J. Mater. Sci. **56** (10), 6064 (2021).

[150] H. W. Shin and J. Y. Son, Appl. Phys. Lett. **117** (20), 202902 (2020).
[151] Q. Chen, Y. K. Zhang, W. Y. Liu, J. Jiang, Q. Yang, and L. M. Jiang, Int. J. Mech. Sci. **212** (212), 106828 (2021).
[152] H. J. Kim, M. H. Park, Y. J. Kim, Y. H. Lee, W. Jeon, T. Gwon, T. Moon, K. D. Kim, and C. S. Hwang, Appl. Phys. Lett. **105** (19), 192903 (2014).
[153] S. Nakayama, H. Funakubo, and H. Uchida, Jpn. J. Appl. Phys. **57** (11S), 11UF06 (5pp) (2018).
[154] X. Wang, D. Zhou, S. Li, X. Liu, P. Zhao, N. Sun, F. Ali, and J. Wang, Ceram. Int. **44** (12), 13867 (2018).
[155] S. L. Weeks, A. Pal, V. K. Narasimhan, K. A. Littau, and T. Chiang, ACS Appl. Mater. Inter. **9** (15), 13440 (2017).
[156] M. H. Park, H. J. Kim, G. Lee, J. Park, Y. H. Lee, Y. J. Kim, T. Moon, K. D. Kim, S. D. Hyun, H. W. Park, H. J. Chang, J. H. Choi, and C. S. Hwang, Appl. Phys. Rev, **6** (4) (2019).
[157] A. Kashir, M. Ghiasabadi Farahani, and H. Hwang, Nanoscale **13** (32), 13631 (2021).
[158] Y. W. Lu, J. Shieh, and F. Y. Tsai, Acta Mater. **115**, 68 (2016).
[159] M. E. McBriarty, V. K. Narasimhan, S. L. Weeks, A. Pal, H. Fang, T. A. Petach, A. Mehta, R. C. Davis, S. V. Barabash, and K. A. Littau, Phys. Status Solid B (2019).
[160] M. Si, X. Lyu, and P. D. Ye, ACS Appl. Electron. Mater. **1** (5), 745 (2019).
[161] J. Wang, D. Wang, Q. Li, A. Zhang, D. Gao, M. Guo, J. Feng, Z. Fan, D. Chen, M. Qin, M. Zeng, X. Gao, G. Zhou, X. Lu, and J. M. Liu, IEEE Electr. Dev. L. **40** (12), 1937 (2019).
[162] H. Chen, L. Tang, L. Liu, Y. Chen, H. Luo, X. Yuan, and D. Zhang, Appl. Surf. Sci. **542**, 148737 (2021).
[163] T. Onaya, T. Nabatame, N. Sawamoto, A. Ohi, N. Ikeda, T. Chikyow, and A. Ogura, Appl. Phys. Express **10** (8) (2017).
[164] T. Schenk, M. Hoffmann, J. Ocker, M. Pesic, T. Mikolajick, and U. Schroeder, ACS Appl. Mater. Inter. **7** (36), 20224 (2015).
[165] K. Florent, S. Lavizzari, L. Di Piazza, M. Popovici, J. Duan, G. Groeseneken, and J. Van Houdt, IEEE T. Electron. Dev. **64** (10), 4091 (2017).
[166] M. Pesic, U. Schroeder, S. Slesazeck, and T. Mikolajick, IEEE T. Device. Mat. Re. **18** (2), 154 (2018).
[167] F. P. G. Fengler, M. Hoffmann, S. Slesazeck, T. Mikolajick, and U. Schroeder, J. Appl. Phys. **123** (20) (2018).
[168] D. Y. Zhou, J. Xu, Q. Li, Y. Guan, F. Cao, X. L. Dong, J. Muller, T. Schenk, and U. Schroder, Appl. Phys. Lett. **103** (19), 4 (2013).
[169] S. Starschich, S. Menzel, and U. Boettger, J. Appl. Phys. **121** (15) (2017).
[170] H. J. Kim, M. H. Park, Y. J. Kim, Y. H. Lee, T. Moon, K. D. Kim, S. D. Hyun, and C. S. Hwang, Nanoscale **8** (3), 1383 (2016).
[171] E. D. Grimley, T. Schenk, X. Sang, M. Pešić, U. Schroeder, T. Mikolajick, and J. M. LeBeau, Adv. Electron. Mater. **2** (9) (2016).
[172] F. Mehmood, T. Mikolajick, and U. Schroeder, Phys. Status Solidi A **217** (22) (2020).
[173] T. Y. Lee, K. Lee, H. H. Lim, M. S. Song, S. M. Yang, H. K. Yoo, D. I. Suh, Z. Zhu, A. Yoon, M. R. MacDonald, X. Lei, H. Y. Jeong, D. Lee, K. Park, J. Park, and S. C. Chae, ACS Appl. Mater. Inter. **11** (3), 3142 (2019).
[174] Y. Ishibashi and Y. Takagi, J. Phys. Soc. Jpn. **31** (2), 506 (2007).
[175] M. Pešić, F. P. G. Fengler, L. Larcher, A. Padovani, T. Schenk, E. D. Grimley, X. Sang, J. M. LeBeau, S. Slesazeck, U. Schroeder, and T. Mikolajick, Adv. Funct. Mater. **26** (25), 4601 (2016).

[176] F. P. G. Fengler, R. Nigon, P. Muralt, E. D. Grimley, X. Sang, V. Sessi, R. Hentschel, J. M. LeBeau, T. Mikolajick, and U. Schroeder, Adv. Electron. Mater. **4** (3) (2018).

[177] M. Hoffmann, U. Schroeder, T. Schenk, T. Shimizu, H. Funakubo, O. Sakata, D. Pohl, M. Drescher, C. Adelmann, R. Materlik, A. Kersch, and T. Mikolajick, J. Appl. Phys. **118** (7) (2015).

[178] M. H. Park, H. J. Kim, Y. J. Kim, Y. H. Lee, T. Moon, K. D. Kim, S. D. Hyun, F. Fengler, U. Schroeder, and C. S. Hwang, ACS Appl. Mater. Inter. **8** (24), 15466 (2016).

[179] A. Chouprik, S. Zakharchenko, M. Spiridonov, S. Zarubin, A. Chernikova, R. Kirtaev, P. Buragohain, A. Gruverman, A. Zenkevich, and D. Negrov, ACS Appl. Mater. Inter. **10** (10), 8818 (2018).

[180] T. Shimizu, T. Yokouchi, T. Oikawa, T. Shiraishi, T. Kiguchi, A. Akama, T. J. Konno, A. Gruverman, and H. Funakubo, Appl. Phys. Lett. **106** (11) (2015).

[181] A. G. Chernikova, M. G. Kozodaev, D. V. Negrov, E. V. Korostylev, M. H. Park, U. Schroeder, C. S. Hwang, and A. M. Markeev, ACS Appl. Mater. Inter. **10** (3), 2701 (2018).

[182] F. P. G. Fengler, M. Pešić, S. Starschich, T. Schneller, C. Künneth, U. Böttger, H. Mulaosmanovic, T. Schenk, M. H. Park, and R. Nigon, Adv. Electron. Mater. **3** (4), 1600505 (2017).

[183] Y. A. Genenko, J. Glaum, M. J. Hoffmann, and K. Albe, Mater. Sci. Eng. B **192**, 52 (2015).

[184] A. Kashir, S. Oh, and H. Hwang, Adv. Eng. Mater. **23** (1) (2020).

[185] T. Mittmann, M. Materano, S. C. Chang, I. Karpov, T. Mikolajick, and U. Schroeder, in *2020 IEEE International Electron Devices Meeting (IEDM)* (2020), pp. 18.4.1.

[186] A. Kashir, H. Kim, S. Oh, and H. Hwang, ACS Appl. Electron. Mater. **3** (2), 629 (2021).

[187] H. B. Kim, M. Jung, Y. Oh, S. W. Lee, D. Suh, and J. H. Ahn, Nanoscale **13** (18), 8524 (2021).

[188] T. Schenk, U. Schroeder, M. Pesic, M. Popovici, Y. V. Pershin, and T. Mikolajick, ACS Appl. Mater. Inter. **6** (22), 19744 (2014).

[189] F. Huang, X. Chen, X. Liang, J. Qin, Y. Zhang, T. Huang, Z. Wang, B. Peng, P. Zhou, H. Lu, L. Zhang, L. Deng, M. Liu, Q. Liu, H. Tian, and L. Bi, Phys. Chem. Chem. Phys. **19** (5), 3486 (2017).

[190] A. K. Tagantsev, I. Stolichnov, E. L. Colla, and N. Setter, J. Appl. Phys. (2001).

[191] X. Liu, D. Zhou, Y. Guan, S. Li, F. Cao, and X. Dong, Acta Mater. **154**, 190 (2018).

[192] D. Y. Zhou, U. Schroeder, G. Jegert, M. Kerber, S. Uppal, R. Agaiby, M. Reinicke, J. Heitmann, and L. Oberbeck, J. Appl. Phys. **106** (4), 4 (2009).

[193] X. F. Li, C. Li, Z. Y. Xu, Y. S. Li, Y. H. Yang, H. H. Hu, Z. Z. Jiang, J. Y. Wang, J. X. Ren, C. Y. Zheng, C. J. Lu, and Z. Wen, Phys. Status. Solid-R. **15** (4), 7 (2021).

[194] J. Y. Jo, H. S. Han, J. G. Yoon, T. K. Song, S. H. Kim, and T. W. Noh, Phys. Rev. Lett. **99** (26), 4 (2007).

[195] T. S. Boscke, S. Teichert, D. Brauhaus, J. Muller, U. Schroder, U. Bottger, and T. Mikolajick, Appl. Phys. Lett. **99** (11), 3 (2011).

[196] K. Takada, M. Murase, S. Migita, Y. Morita, H. Ota, N. Fujimura, and T. Yoshimura, Appl. Phys. Lett. **119** (3) (2021).

[197] W. L. Warren, D. Dimos, G. E. Pike, B. A. Tuttle, M. V. Raymond, R. Ramesh, and J. T. Evans, Appl. Phys. Lett. **67** (6), 866 (1995).

[198] M. Grossmann, O. Lohse, D. Bolten, U. Boettger, T. Schneller, and R. Waser, J. Appl. Phys. **92** (5), 2680 (2002).

[199] M. C. Chun, S. Park, S. Park, G.-y. Park, M. J. Kim, Y. Cho, and B. S. Kang, J. Alloys Compd. **823** (2020).

[200] K. Takada, S. Takarae, K. Shimamoto, N. Fujimura, and T. Yoshimura, Adv. Electron. Mater. **7** (8) (2021).

[201] A. G. Chernikova and A. M. Markeev, Appl. Phys. Lett. **119** (3) (2021).
[202] B. Y. Kim, B. S. Kim, S. D. Hyun, H. H. Kim, Y. B. Lee, H. W. Park, M. H. Park, and C. S. Hwang, Appl. Phys. Lett. **117** (2) (2020).
[203] W. Hamouda, C. Lubin, S. Ueda, Y. Yamashita, and N. Barrett, Appl. Phys. Lett. **116** (25), 252903 (2020).
[204] P. Buragohain, A. Erickson, P. Kariuki, T. Mittmann, C. Richter, P. D. Lomenzo, H. Lu, T. Schenk, T. Mikolajick, U. Schroeder, and A. Gruverman, ACS Appl. Mater. Inter. **11** (38), 35115 (2019).
[205] Y. Higashi, B. Kaczer, A. S. Verhulst, B. J. O'Sullivan, N. Ronchi, S. R. C. McMitchell, K. Banerjee, L. D. Piazza, M. Suzuki, D. Linten, and J. Van Houdt, IEEE T. Electron. Dev. **67** (11), 4911 (2020).
[206] P. Buragohain, C. Richter, T. Schenk, H. Lu, T. Mikolajick, U. Schroeder, and A. Gruverman, Appl. Phys. Lett. **112** (22) (2018).
[207] Y. Zhou, H. K. Chan, C. H. Lam, and F. G. Shin, J. Appl. Phys. **98** (2), 5406 (2005).
[208] H. Mulaosmanovic, J. Ocker, S. Mueller, U. Schroeder, and S. Slesazeck, ACS Appl. Mater. Inter. **9** (4) (2017).
[209] K. Z. Rushchanskii, S. Bluegel, and M. Lezaic, Phys. Rev. Lett. **127** (8) (2021).
[210] T. Mittmann, F. P. G. Fengler, C. Richter, M. H. Park, T. Mikolajick, and U. Schroeder, Microelectron. Eng. (2017).
[211] P. D. Lomenzo, Q. Takmeel, C. M. Fancher, C. Zhou, N. G. Rudawski, S. Moghaddam, J. L. Jones, and T. Nishida, IEEE Electr. Dev. L. **36** (8), 766 (2015).
[212] C. Zacharaki, P. Tsipas, S. Chaitoglou, S. Fragkos, and A. Dimoulas, Appl. Phys. Lett. **114** (11), 112901 (2019).
[213] K. Y. Chen, Y. H. Huang, R. W. Kao, Y. X. Lin, K. Y. Hsieh, and Y. H. Wu, IEEE T. Electron. Dev. **66** (8), 3636 (2019).
[214] C. Zacharaki, P. Tsipas, S. Chaitoglou, L. Bégon-Lours, M. Halter, and A. Dimoulas, Appl. Phys. Lett. **117** (21) (2020).
[215] M. Pešić, U. Schroeder, and T. Mikolajick, in *Ferroelectricity in Doped Hafnium Oxide: Materials, Properties and Devices* (2019), pp. 413.
[216] S. O. Park, B. J. Bae, D. C. Yoo, and U.-I. Chung, Nanotechnology (2010).
[217] J. M. Koo, B. S. Seo, S. Kim, S. Shin, J. H. Lee, H. Baik, J. H. Lee, J. H. Lee, B. J. Bae, J. E. Lim, D. C. Yoo, S. O. Park, H. S. Kim, H. Han, S. Baik, J. Y. Choi, Y. J. Park, and Y. Park, in *IEEE International Electron Devices Meeting 2005, Technical Digest* (2005), pp. 351.
[218] F. Fengler, M. Pesic, S. Starschich, T. Schneller, U. Bottger, T. Schenk, M. H. Park, T. Mikolajick, and U. Schroeder, presented at the Solid-state Device Research Conference, 2016.
[219] S. Mueller, S. R. Summerfelt, J. Muller, U. Schroeder, and T. Mikolajick, IEEE Electr. Dev. L. **33** (9), 1300 (2012).
[220] Z. Fan, J. Chen, and J. Wang, J. Adv. Dielec. **06** (02), 1630003 (2016).
[221] H. K. Yoo, J. S. Kim, Z. Zhu, Y. S. Choi, A. Yoon, M. R. MacDonald, X. Lei, T. Y. Lee, D. Lee, S. C. Chae, J. Park, D. Hernker, J. G. Langan, Y. Nishi, S. J. Hong, and Ieee, presented at the 63rd IEEE Annual International Electron Devices Meeting (IEDM), San Francisco, CA, 2017.
[222] L. Grenouillet, T. Francois, J. Coignus, N. Vaxelaire, and E. Nowak, presented at the 2020 IEEE Silicon Nanoelectronics Workshop (SNW), 2020.
[223] J. Okuno, T. Kunihiro, K. Konishi, H. Maemura, Y. Shuto, F. Sugaya, M. Materano, T. Ali, M. Lederer, K. Kuehnel, K. Seidel, U. Schroeder, T. Mikolajick, M. Tsukamoto, and T. Umebayashi, in *2021 IEEE International Memory Workshop (IMW)* (2021), pp. 1.

[224] F. Huang, Y. Wang, X. Liang, J. Qin, Y. Zhang, X. Yuan, Z. Wang, B. Peng, L. Deng, Q. Liu, L. Bi, and M. Liu, IEEE Electr. Dev. L. **38** (3), 330 (2017).

[225] T. Oikawa, H. Morioka, A. Nagai, H. Funakubo, and K. Saito, Appl. Phys. Lett. **85** (10), 1754 (2004).

[226] J. Celinska, V. Joshi, S. Narayan, L. McMillan, and C. Paz de Araujo, Appl. Phys. Lett. **82** (22), 3937 (2003).

[227] J. Müller, E. Yurchuk, T. Schlösser, J. Paul, R. Hoffmann, S. Müller, D. Martin, S. Slesazeck, P. Polakowski, J. Sundqvist, M. Czernohorsky, K. Seidel, P. Kücher, R. Boschke, M. Trentzsch, K. Gebauer, U. Schröder, and T. Mikolajick, presented at the 2012 Symposium on VLSI Technology (VLSIT), 2012.

[228] T. S. Böscke, J. Müller, D. Bräuhaus, U. Schröder, and U. Böttger, IEDM Tech. Dig., 547 (2011).

[229] R. Carter, J. Mazurier, L. Pirro, J. U. Sachse, and B. Rice, presented at the IEEE International Electron Devices Meeting, 2017.

[230] S. Dünkel, M. Trentzsch, R. Richter, P. Moll, C. Fuchs, O. Gehring, M. Majer, S. Wittek, B. Müller, T. Melde, H. Mulaosmanovic, S. Slesazeck, S. Müller, J. Ocker, M. Noack, D. A. Löhr, P. Polakowski, J. Müller, T. Mikolajick, J. Höntschel, B. Rice, J. Pellerin, and S. Beyer, presented at the 2017 IEEE International Electron Devices Meeting (IEDM), 2017.

[231] J. Junquera and P. Ghosez, Nature **422** (6931), 506 (2003).

[232] E. Yurchuk, J. Mueller, S. Mueller, J. Paul, M. Pesic, R. van Bentum, U. Schroeder, and T. Mikolajick, IEEE T. Electron. Dev. **63** (9), 3501 (2016).

[233] W. Xiao, C. Liu, Y. Peng, S. Zheng, Q. Feng, C. Zhang, J. Zhang, Y. Hao, M. Liao, and Y. Zhou, Nanoscale Res. Lett. **14** (2019).

[234] T. Kim, J. Hwang, G. Kim, M. Jung, and S. Jeon, Phys. Status. Solid-R. **15** (5) (2021).

[235] T. Ali, P. Polakowski, S. Riedel, T. Buettner, T. Kaempfe, M. Rudolph, B. Paetzold, K. Seidel, D. Loehr, R. Hoffmann, M. Czernohorsky, K. Kuehnel, P. Steinke, J. Calvo, K. Zimmermann, and J. Mueller, IEEE T. Electron. Dev. **65** (9), 3769 (2018).

[236] K. Yan, M. Takahashi, and S. Sakai, Appl. Phys. A-mater. **108** (4), 835 (2012).

[237] A. J. Tan, Y. H. Liao, L. C. Wang, N. Shanker, J. H. Bae, C. Hu, and S. Salahuddin, IEEE Electr. Dev. L. **42** (7), 994 (2021).

[238] K. Florent, S. Lavizzari, L. Di Piazza, M. Popovici, E. Vecchio, G. Potoms, G. Groeseneken, J. Van Houdt, and Ieee, presented at the 37th Symposium on VLSI Technology, Kyoto, JAPAN, 2017.

[239] K. Florent, M. Pesic, A. Subirats, K. Banerjee, S. Lavizzari, A. Arreghini, L. Di Piazza, G. Potoms, F. Sebaai, S. R. C. McMitchell, M. Popovici, G. Groeseneken, J. Van Houdt, and Ieee, presented at the 64th IEEE Annual International Electron Devices Meeting (IEDM), San Francisco, CA, 2018.

[240] M. K. Kim, I. J. Kim, and J. S. Lee, Sci. Adv. **7** (3), eabe1341 (2021).

[241] P. Wang, W. Shim, Z. Wang, J. Hur, S. Datta, A. I. Khan, and S. Yu, IEEE T. Electron. Dev. **67** (3), 962 (2020).

[242] H. S. Kum, H. Lee, S. Kim, S. Lindemann, W. Kong, K. Qiao, P. Chen, J. Irwin, J. H. Lee, S. Xie, S. Subramanian, J. Shim, S.-H. Bae, C. Choi, L. Ranno, S. Seo, S. Lee, J. Bauer, H. Li, K. Lee, J. A. Robinson, C. A. Ross, D. G. Schlom, M. S. Rzchowski, C.-B. Eom, and J. Kim, Nature **578** (7793), 75 (2020).

[243] H. Yu, C.-C. Chung, N. Shewmon, S. Ho, J. H. Carpenter, R. Larrabee, T. Sun, J. L. Jones, H. Ade, B. T. O'Connor, and F. So, Adv. Funct. Mater. **27** (21) (2017).

[244] J. Jiang, Y. Bitla, C. W. Huang, T. H. Do, H. J. Liu, Y. H. Hsieh, C. H. Ma, C. Y. Jang, Y. H. Lai, P. W. Chiu, W. W. Wu, Y. C. Chen, Y. C. Zhou, and Y. H. Chu, Sci. Adv. **3** (6), 8 (2017).

[245] W. W. Xiao, C. Liu, Y. Peng, S. Z. Zheng, Q. Feng, C. F. Zhang, J. C. Zhang, Y. Hao, M. Liao, and Y. C. Zhou, ACS Appl. Electron. Mater. **1** (6), 919 (2019).
[246] X. Tian, S. Shibayama, T. Nishimura, T. Yajima, and A. Toriumi, presented at the 2016 International Conference on Solid State Devices and Materials, 2016.
[247] A. Chernikova, M. Kozodaev, A. Markeev, D. Negrov, M. Spiridonov, S. Zarubin, O. Bak, P. Buragohain, H. Lu, E. Suvorova, A. Gruverman, and A. Zenkevich, ACS Appl. Mater. Inter. **8** (11), 7232 (2016).
[248] F. Ambriz-Vargas, G. Kolhatkar, M. Broyer, A. Hadj-Youssef, R. Nouar, A. Sarkissian, R. Thomas, C. Gomez-Yanez, M. A. Gauthier, and A. Ruediger, ACS Appl. Mater. Inter. **9** (15), 13262 (2017).
[249] F. Ambriz-Vargas, G. Kolhatkar, R. Thomas, R. Nouar, and A. Ruediger, Appl. Phys. Lett. **110** (9), 093106 (2017).
[250] J. Seo and M. Shin, presented at the 2020 International Conference on Simulation of Semiconductor Processes and Devices (SISPAD), 2020.
[251] S. Kabuyanagi, S. Fujii, K. Usuda, M. Yamaguchi, and M. Saitoh, presented at the 2018 International Conference on Solid State Devices and Materials, 2018.
[252] S. Fujii, M. Yamaguchi, S. Kabuyanagi, K. Ota, and M. Saitoh, presented at the 2020 IEEE Symposium on VLSI Technology, 2020.
[253] M. H. Park, H. J. Kim, Y. H. Lee, Y. J. Kim, T. Moon, K. D. Kim, S. D. Hyun, and C. S. Hwang, Nanoscale **8** (29), 13898 (2016).
[254] S. Roy, G. Niu, Q. Wang, Y. K. Wang, Y. J. Zhang, H. P. Wu, S. J. Zhai, P. Shi, S. N. Song, Z. T. Song, Z. G. Ye, C. Wenger, T. Schroeder, Y. H. Xie, X. J. Meng, W. B. Luo, and W. Ren, ACS Appl. Mater. Inter. **12** (9), 10648 (2020).
[255] V. Milo, C. Zambelli, P. Olivo, E. Perez, M. K. Mahadevaiah, O. G. Ossorio, C. Wenger, and D. Ielmini, APL Mater. **7** (8), 10 (2019).
[256] D. K. Lee, M. H. Kim, T. H. Kim, S. Bang, Y. J. Choi, S. Kim, S. Cho, and B. G. Park, Solid-State Electron. **154**, 31 (2019).
[257] K. Lee, H. J. Lee, T. Y. Lee, H. H. Lim, M. S. Song, H. K. Yoo, D. I. Suh, J. G. Lee, Z. Zhu, A. Yoon, M. R. MacDonald, X. Lei, K. Park, J. Park, J. H. Lee, and S. C. Chae, ACS Appl. Mater. Inter. **11** (42), 38929 (2019).
[258] L. Chen, T. Y. Wang, Y. W. Dai, M. Y. Cha, H. Zhu, Q. Q. Sun, S. J. Ding, P. Zhou, L. Chua, and D. W. Zhang, Nanoscale **10** (33), 15826 (2018).
[259] M. K. Kim and J. S. Lee, Adv. Mater. **32** (12), 1907826.1 (2020).
[260] H. Jeon, S. G. Kim, J. Park, S. H. Kim, E. Park, J. Kim, and H. Y. Yu, Small **16** (49) (2020).
[261] M. Jerry, P. Y. Chen, J. Zhang, P. Sharma, K. Ni, S. Yu, and S. Datta, presented at the 63rd IEEE Annual International Electron Devices Meeting (IEDM), San Francisco, CA, 2017.
[262] M. K. Kim and J. S. Lee, Nano Lett. **19** (3), 2044 (2019).
[263] C. P. Chou, Y. X. Lin, Y. K. Huang, C. Y. Chan, and Y. H. Wu, ACS Appl. Mater. Inter. **12** (1), 1014 (2020).
[264] H. Mulaosmanovic, E. Chicca, M. Bertele, T. Mikolajick, and S. Slesazeck, Nanoscale **10** (46), 21755 (2018).
[265] B. Suresh, M. Bertele, E. T. Breyer, P. Klein, H. Mulaosmanovic, T. Mikolajick, S. Slesazeck, and E. Chicca, *Simulation of integrate-and-fire neuron circuits using HfO2-based ferroelectric field effect transistors*. (2019), pp.229.
[266] B. Zeng, C. Liu, S. Dai, P. Zhou, and Y. Zhou, Adv. Funct. Mater., 2011077 (2021).

[267] H. Ryu, H. Wu, F. Rao, and W. Zhu, Sci. Rep. **9** (2019).

[268] V. Mikheev, A. Chouprik, Y. Lebedinskii, S. Zarubin, Y. Matveyev, E. Kondratyuk, M. G. Kozodaev, A. M. Markeev, A. Zenkevich, and D. Negrov, ACS Appl. Mater. Inter. **11** (35), 32108 (2019).

[269] V. Mikheev, A. Chouprik, Y. Lebedinskii, S. Zarubin, A. M. Markeev, A. V. Zenkevich, and D. Negrov, Nanotechnology **31** (21) (2020).

[270] Q. L. Zheng, Z. W. Wang, N. B. Gong, Z. Z. Yu, C. Chen, Y. M. Cai, Q. Q. Huang, H. Jiang, Q. F. Xia, and R. Huang, IEEE Electr. Dev. L. **40** (8), 1309 (2019).

[271] S.-J. Yoon, S.-E. Moon, and S.-M. Yoon, Nanoscale **12** (25), 13421 (2020).